Subcooled Two-Phase Flow Heat Transfer in Multiscale Systems

Zur Erlangung des akademischen Grades
Doktor der Ingenieurwissenschaften
der Fakultät für Maschinenbau
Karlsruher Institut für Technologie (KIT)

genehmigte
Dissertation
von

Dipl.-Ing. Martin Sonntag

Tag der mündlichen Prüfung: 21. Juni 2017

Hauptreferent: Prof. Dr.-Ing. Xu Cheng

Korreferent: Prof. Dr.-Ing. Thomas Schulenberg

I declare that I have developed and written the enclosed thesis completely by myself, and have not used sources or means without declaration in the text.

Karlsruhe, 3.4.2017

. . . .
(Martin Sonntag)

Acknowledgements

Abstract

Residual heat removal in case of a severe accident in a nuclear power plant without the need for external power sources is proposed for many new nuclear power plants. These *passive safety systems* rely mainly on natural circulation or radiation to remove decay heat.

The concept of In Vessel Retention (IVR) foresees the flooding of a cavity below the reactor pressure vessel (RPV) with cooling water in case of a severe accident. The cooling water is stored in a large storage tank located above the RPV. The decay heat is supposed to be removed by a two-phase natural circulation flow through a cooling path along the outside of the RPV wall and the storage tank. The evaporated portion of the cooling water is separated by a steam vent and condensed at structural material inside the containment or at the containment walls. It is then fed back to the storage tank.

In case of reactors with an electrical power of over 1 GW, the coolability of the RPV is not clear yet. The limiting factor is the critical heat flux (CHF) imposed on the RPV wall. The highest thermal loads on the RPV wall come from a thin metallic layer on top of a ceramic pool of molten core material, due to the higher thermal conductivity in the metallic layer.

This leads to the following challenges in the simulation of a passive IVR system that will be addressed in this study:

- *Two-phase flow heat transfer from RPV wall to cooling water.* To simulate the wall heat transfer and evaporation rates, a new boiling model has been proposed in this study. The model is build on top of a well known one dimensional correlation and extends this to a three dimensional Eulerian two-fluid CFD approach. The model is validated against a series of experiments for low and high heat fluxes.

- *Heat flux distribution on the outside of the RPV wall.* Crust formation inside the ceramic pool and partial melting of the RPV wall have a great influence on the wall heat flux distribution on the outside of the RPV wall. Also the interaction between the metallic layer and the RPV wall/ ceramic pool have to be considered.

- *Integral system behavior of the cooling system.* To study the integral system behavior, like mass flow rate response to different boundary conditions, the complete cooling loop has to be simulated. In order to achieve this a legacy one-dimensional STH code has been coupled with the CFD library, where a boiling model was implemented.

The main achievements of this study include the proof of applicability of a robust boiling model to predict void fraction distributions under subcooled nucleate boiling flow conditions. It has further been shown that the coupling of a legacy STH code with a CFD library is feasible, also for two-phase flows. With a simple model for solidification and melting, the core melt behavior previously predicted by lumped parameter codes has been recalculated with a CFD approach. Finally, the application of the developed two-phase CFD-STH code to a prototypical/academic IVR system has shown that under passive conditions the inlet subcooling plays a significant role on the flow stability.

Kurzfassung

Das Abführen von Nachzerfallswärme ohne Verwendung externer Energiequellen wird für Reaktoren der kommenden Generation vorgeschlagen. Diese *passiven Sicherheitssysteme* basieren meist auf Naturkonvektion oder Wärmrstrahlung zur Abfuhr der Nachzerfallswärme.

Das so genannte In Vessel Retention (IVR) Konzept sieht das Fluten der Reaktorgrube mit Kühlwasser im Falle eines Schwerunfalls vor. Das Kühlwasser wird in einem Tank vorgehalten, der auf einem höheren Niveau als der Reaktordruckbehälter (RDB) angebracht ist. Die Nachzerfallswärme soll über eine Zweiphasenströmung um die äußere Wand des RDB und durch den Vorratstank abgeführt werden. Der Anteil des Kühlwassers, der verdampft wurde, wird vom Rest der Strömung getrennt. Er kondensiert folgend an Bauteilen im Inneren des Containments oder dessen Wänden. Das Kondensat wird gesammelt und dem Vorratstank wieder zugeführt.

Für Reaktoren mit einer elektrischen Leistung von über 1 GW ist fraglich, ob der RDB dadurch ausreichend gekühlt werden kann. Der limitierende Faktor ist hierbei die kritische Wärmestromdichte an der RDB Außenwand. Die größte Wärmestromdichte wird von einer dünnen metallischen Schicht mit sehr hoher Wärmeleitfähigkeit oberhalb der geschmolzenen Oxidschicht erwartet.

Dies führt auf folgende Herausforderungen bei der Simulation eines passiven IVR Systems, die in dieser Studie bearbeitet werden:

- *Zweiphasenströmung mit Wärmeübergang von der RDB Außenwand zum Kühlwasser.* Um den Zweiphasenwärmeübergang und die Evaporationsraten zu simulieren, wurde ein neues Modell vorgeschlagen. Das Modell basiert auf einer anerkannten eindimensionalen Korrelation und erweitert diese für die Implementierung in einen dreidimensionalen Zweiphasen-CFD Kontext. Das Modell und dessen Implementierung wurden durch Nachrechnen von Experimenten aus der Literatur validiert.

- *Wärmestromdichten-Verteilung an der äußeren RDB Wand.* Krustenbildung im inneren des Oxid-Pools und das partielle Schmelzen der RDB Wand haben großen Einfluss auf die Wärmestromdichte-Verteilung an der RDB Außenwand. Des Weiteren spielen die Interaktion zwischen der metallischen Schicht, der RDB-Wand und des Oxid-Pools eine wichtige Rolle.

- *Integrales Verhalten des gesamten Kühlsystems.* Um das integrale Systemverhalten des Kühlsystems, wie das Verhalten des Massenstroms bei unterschiedlichen Randbedingungen zu untersuchen, muss das gesamte System simuliert werden. Um dies durchführen zu können wurde ein System Thermo Hydraulic Code (STH) mit einem dreidimensionalen CFD Code gekoppelt.

Die wichtigsten Beiträge dieser Arbeit beinhalten die Entwicklung und Anwendung eines robusten Modells zur Vorhersage des Wärmeübergangs für unterkühltes Blasensieden. Des weiteren wurde gezeigt, dass die Kopplung eines eindimensionalen STH-Programs

mit einem dreidimensionalen CFD-Code für Zweiphasenströmungen möglich ist. Mit einem einfachen Modell für Schmelz- und Verferstigungsvorgägne konnte das hydrodynamische Verhalten eines Schmelzpools nachgerechnet und mit existierenden eindimensionalen Berechnungen verglichen werden. Schließlich zeigte die Anwendung der entwickelten Simulations Tools auf ein prototypisches passives IVR System, dass die Einlassunterkühlung des Kühlwassers einen wesentlichen Einfluss auf die Strömungsstabilität unter Naturumlauf hat.

Contents

Nomenclature

Latin Symbols

Symbol	Dimensions	Description
A	m^2	Flow area
A_d	$-$	Drag related coefficient in mixture $k - \epsilon$ model
A_i	m^2	Interfacial area
C_D	$-$	Drag coefficient
C_{vm}	$-$	Virtual mass coefficient
C_L	$-$	Lift coefficient
C_l	$-$	Shear lift coefficient
C_{TD}	$-$	Turbulent dispersion coefficient
C_p	$-$	Model coefficient in mixture $k - \epsilon$ model
C_t	$-$	Turbulent response coefficient
C_u	$-$	Model constant in solidification model
C_{wl}	$-$	Wall Force coefficient
C^ϕ	$-$	Two-phase friction multiplier
D	m	Dimension
E	$-$	Empirical constant in definition of T^+
Eo	$-$	Eötvös Number
F		Blending function
F_{byc}	N	Buoyancy Force
F_{conv}		Convective enhancement factor
F_d	N	Drag Force
F_{du}	N	Bubble growth Force
F_{fl}	N	Shear lift Force
F_V	$\frac{m^3}{s}$	Volume face flux
G	$\frac{kg}{s}$	Mass flow rate
G_A	$\frac{kg}{m^2 s}$	Mass flux
G_s	$-$	Fluid velocity gradient (dimensionless)
J	$\frac{m}{s}$	Superficial velocity
I	$-$	Intensity
L	$\frac{J}{kg}$	Latent heat of solidification
Ja	$-$	Jakob number
$K_{b(1-2)}$	$-$	Model constants for bubble breakup
$K_{c(1-3)}$	$-$	Model constants for bubble coalescence
M	$\frac{N}{m^3}$	Interfacial Momentum
N	$\frac{1}{m^2}$	Nucleation site density
P	$-$	Sublayer Resistance Function
P_k	$\frac{kg}{ms^3}$	Production of turbulent kinetic energy

Latin Symbols Cont.

Symbol	Dimensions	Description
Pr	$-$	Prandtl Number
Q	W	Residual heat
Re	$-$	Reynolds Number
Re_{nb}	$-$	Bubble Reynolds Number
S	$\frac{kg}{sm^3}$	Interfacial mass exchange
S_{flow}	$-$	Boiling suppression factor due to flow
S_{total}	$-$	Total boiling suppression factor
S_s	m^2	Face area of a computational cell
S_{sub}	$-$	Boiling suppression factor due to subcooling
$T_{BK,CO,I}$	s	Bubble coalescence and breakup interaction time
$T_{BK,CO,TF}$	s	Bubble coalescence and breakup free traveling time
WE	$-$	Weber number

Latin Symbols Cont.

Symbol	Dimensions	Description
a_i	$\frac{1}{m}$	Interfacial area concentration
b	$-$	Empirical constant
c_p	$\frac{J}{kgK}$	Specific heat capacity
d_b	m	Bubble diameter
d_h	m	Hydraulic diameter
g	$\frac{m}{s^2}$	Gravitational constant
f_M	$-$	Mass fraction
f_N	$-$	Mole fraction
f_v	$-$	Volume fraction
f_{BK}	$\frac{1}{s}$	Bubble break up frequency
f_{CO}	$\frac{1}{s}$	Bubble coalescence frequency
h	$\frac{J}{kg}$	Specific enthalpy
h_0	m	Initial film thickness
h_{cr}	m	Critical film thickness
h_{mac}	$\frac{W}{m^2K}$	Macroscopic heat transfer coefficient
h_{mic}	$\frac{W}{m^2K}$	Microscopic heat transfer coefficient
htc	$\frac{W}{m^2K}$	Heat transfer coefficient
i	$\frac{J}{kg}$	Latent heat of vaporization
k	$\frac{m^2}{s^2}$	Turbulent kinetic energy
l	m	Length
n	$-$	Normal wall vector
n	$\frac{1}{m^3}$	Number of bubbles per volume
p	Pa	Pressure
q	$\frac{W}{m^2}$	Heat flux
r_b	m	Bubble radius
r_{rough}	m	Absolute wall roughness
t	s	Time
u	$\frac{m}{s}$	Velocity
u_c	$\frac{m}{s}$	Velocity magnitude at $y^+ = y_{therm}$
x, y, z	-	Direction of Cartesian coordinate system

Greek Symbols

Symbol	Dimensions	Description
Δ	$-$	Difference
Ω	m^3	Volume
α	$-$	Void fraction
α_1	$-$	Model constant in $k-\omega$ model
α_2	$-$	Model constant in $k-\omega$ model
β	$\frac{1}{K}$	Linear thermal expansion coefficient
β_{solid}	$-$	Solid fraction
β_1	$-$	Model constant in $k-\omega$ model
β_2	$-$	Model constant in $k-\omega$ model
β^*	$-$	Model constant in $k-\omega$ model
β_t	$-$	Model coefficient in mixture $k-\epsilon$ model
γ	$\frac{Pr}{Pr_t}$	Prandtl number ratio
ϵ	$\frac{m^2}{s^3}$	Dissipation of turbulent energy
ϕ	$-$	Field variable
ϕ^{BK}	$\frac{1}{m^3}$	Interfacial area source due to break up
ϕ^{CO}	$\frac{1}{m^3}$	Interfacial area source due to coalescence
ϕ^{NUC}	$\frac{1}{m^3}$	Interfacial area source due to nucleation
κ	$\frac{m^2}{s}$	Thermal diffusivity
λ	$\frac{W}{mK}$	Thermal conductivity
λ_f	$-$	Wall friction coefficient
μ	$\frac{Pa}{s}$	Dynamic viscosity
ω	$\frac{1}{s}$	Turbulent eddy frequency
ρ	$\frac{kg}{m^4}$	Density
σ	$\frac{W}{m^2K^4}$	Stefan-Boltzmann constant
σ_t	-	Turbulent Schmidt number
σ_{k1}	-	Model constant in $k-\omega$ model
σ_{k2}	-	Model constant in $k-\omega$ model
$\sigma_{\omega1}$	-	Model constant in $k-\omega$ model
$\sigma_{\omega2}$	-	Model constant in $k-\omega$ model
θ	deg	Angular position of hemisphere
τ	$\frac{N}{m^2}$	shear stress
τ_c	s	Characteristic time

Subscripts

Symbol	Dimensions	Description
E	–	At cell center of cell east
P	–	At cell center
0	–	At reference conditions
c	–	Continuous phase
cr	–	Critical
d	–	Dispersed phase
dep	–	At departure
eff	–	Effective
e	–	Face center value east
eq	–	At equilibrium
$evap$	–	Evaporation
fc	–	Forced convection
inf	–	Infinity
l	–	Liquid
$lift$	–	At lift off
log	–	In logarithmic layer
N	–	Mole
M	–	Mass
m	–	Mixture
pc	–	Phase change
$quench$	–	Quenching
r	–	relative
rad	–	Radiation
ref	–	Reference value
sup	–	Superheat
SS	–	Stainless Steel
t	–	Turbulent
v	–	Volume
vis	–	In viscous sub-layer
$wall$	–	At the wall

Superscripts

Symbol	Dimensions	Description
n	–	At time step n
0	–	At old time step
$'$	–	Fluctuation
$+$	–	Dimensionless
$^{-}$	–	Mean
$\cdot$	–	First temporal derivative
$\cdot\cdot$	–	Second temporal derivative
$\sim$	–	Limited

Abbreviations

Abbreviation	long form
ATHLET	Analysis of THermal-hydraulics of LEaks and Transients
CEA	Alternative Energies and Atomic Energy Commission
CFD	Computational Fluid Dynamics
CHF	Critical Heat Flux
FVM	Finite Volume Method
GNU	GNU is Not Unix
GRS	Gesellschaft für Anlagen- und Reaktorsicherheit gGmbH
I/O	Input - Output
IAC	Interfacial area concentration
IATE	Interfacial area concentration transport equation
IVR	In vessel retention
KHNP	Korea Hydro and Nuclear Power Co., Ltd.
ONB	Onset of nucleate boiling
PWR	Pressurized water reactor
RANS	Reynolds averaged Navier Stokes equations
RELAP	Reactor Excursion and Leak Analysis Program
RDB	Reaktordruckbehälter
RPV	Reactor pressure vessel
TFO	Thermo Fluid Object
SNB	Subcooled nucleate boiling
SNPTC	State Nuclear Power Technology Company
STH	System thermal hydraulic
VTK	Visualization Tool Kit

1. Introduction

Transport of heat from one place to another is a key feature in many engineering systems. The more efficient this transport process can be established, the smaller, cheaper and more elegant the design of the system can be accomplished. A very efficient mode of heat transfer is nucleate flow boiling. Here heat is transferred from a solid wall to a moving liquid. If the wall temperature exceeds a certain value, small vapor nuclei are formed in the liquid. This phenomena is called onset of nucleate boiling (ONB). These nuclei grow until they reach a size called bubble departure diameter and then leave their origin of nucleation (nucleation site). After traveling along the wall in flow direction for a while and still growing in size, the bubbles detach from the wall at their lift-off diameter to either condensate or travel along with the main flow depending on the subcooling of the liquid.

Unfortunately, there is a limit to the upper heat flux that can be applied at the wall. This limit can be observed in experiments with a sudden increase of the wall temperature which leads to a decrease in the efficiency of the heat transfer. This upper limit is called Critical Heat Flux (CHF). The increase of the wall temperature can lead to deformation of materials or the loss of structural integrity. An overview of available experimental data on CHF has been compiled by Cheng and Müller (2003).

If one wants to utilize nucleate flow boiling in an engineering system for the removal of heat, he has to know this limit. Finding a formula to describe critical heat flux has been subject of many studies in the last decades (Weisman and Pei (1983) , Groeneveld et al. (1986) or a detailed overview given by Sadasivan et al. (1995)). As the correlations or lookup tables available today are tailored to specific geometries or use cases, finding a more universal method to identify critical heat flux, is still of great interest today.

1.1 In Vessel Retention

One application that requires the transport of very high thermal loads is *In Vessel Retention* (IVR). IVR is a concept proposed by Theofanous et al. (1997) and first licensed in the Westinghouse pressurized water cooled reactor (PWR) AP600. Table 1.1 gives an overview of commercial nuclear reactors equipped with an IVR system. The main idea is to flood a cavity under the reactor pressure vessel (RPV) with water in the case of an accident scenario with core melt progression. This setup is schematically illustrated in figure 1.1. The water is supposed to cool the outer surface of the RPV wall and ensure its
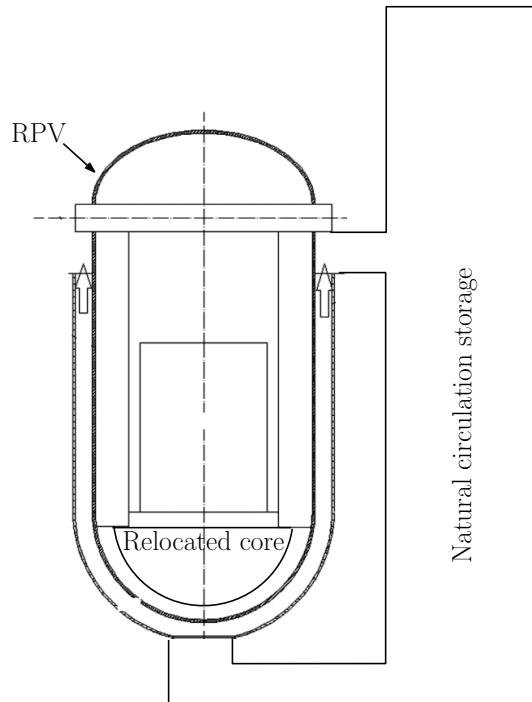
Figure 1.1: Basic concept of the In Vessel Retention (IVR) system. Graphic from Yue et al. (2015) (modified).

Table 1.1: Reactor systems planned or already built with IVR system.

Name	Manufacturer	Power (el.)
VVER-440	Westinghouse and Russia	488 $MWel$
AP 600 (Rempe et al., 1997)	Westinghouse	600 $MWel$
AP 1000 (Cheng, 2013)	Westinghouse	1000 $MWel$
SWR 1000 (Cheng, 2013)	Areva	1000 $MWel$
CAP 1400 (Zheng et al., 2016)	SNPTC	1400 $MWel$
APR 1400 (Lee et al., 2009)	KHNP	1400 $MWel$

integrity. Inside the RPV, a pool of molten uranium oxide has been formed with a lighter metallic layer on top. If successfully applied, no radioactive material would be released through the RPV wall, even in case of a complete core melt. The driving force to supply cooling water to the cavity would be natural circulation or through an auxiliary pump. In case of natural circulation, this emergency system would be a *passive* safety system. Passive safety systems do not rely on electrical power, which excludes the use of pumps and makes them still effective even in a case of a complete station blackout.

1.2 Objective

Theofanous et al. (1997) state that the upper limit of heat flux that will ensure the integrity of the reactor pressure vessel will be right below the critical heat flux (CHF). To identify this CHF value for this particular case, it is impossible to do experiments in a 1:1 scale (geometric, material, power and time). For this reason, all the experiments available are scaled in one way or another (see Park et al. (2013) for example). This leaves us with simulation as the only method to describe and understand the different phenomena and their interaction with each other happening at different scales in such a complex system.

Recent publications like Macek and Vyskocil (2008) or Lifante et al. (2013) use the near wall void fraction in two-fluid simulations as a way to asses values for CHF. Bestion (2014)
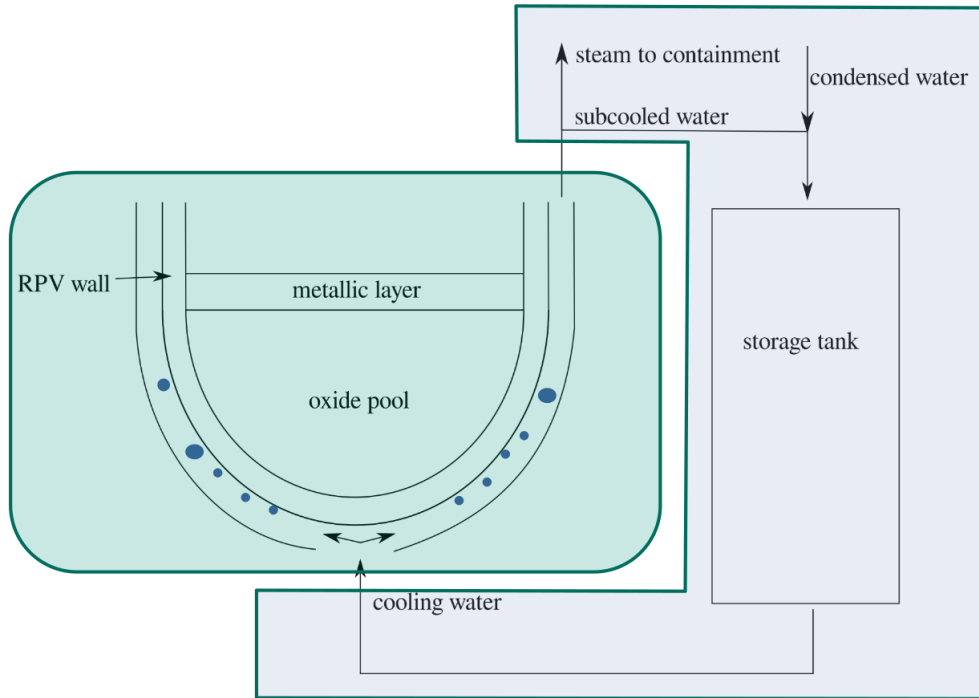
Figure 1.2: Scheme of the division strategy for the IVR system. The green part is simulated by CFD and the light gray part by a system thermo-hydraulic approach.

suggests that the Euler-Euler Method (see. 2.1.2) could be the right compromise between precision and computational effort for the simulation of an external reactor vessel cooling scenario.

As it is not feasible to simulate the whole cooling flow path with a three dimensional Euler-Euler method, a coupled approach between 3D-CFD and a system thermo-hydraulic (STH) code will be used. This leads to three main topics that will be discussed in this study.

- The first being the modeling of subcooled two-phase flow wall heat transfer with a 3D-CFD method.

- The second will be the coupling between the CFD-code and the STH-code.

- And the last part will be an application to a typical IVR system after a rigorous validation of the developed and implemented models and methods.

This strategy of dividing the IVR cooling system into a CFD part and a system thermo-hydraulics part is depicted in figure 1.2. Here, the green area shows the part of the complete system that will be simulated by CFD and the light gray area shows the part simulated by a system themo-hydraulics approach.

1.3 Previous Studies

Wall Heat Flux Modeling in Two-Phase Flows

An extensive overview of the history of advances in the modeling of wall heat transfer in two-phase flows is given by Steiner (2006). He divides the modeling approaches into two categories. The first being general empirical correlations and the second being mechanistic models. In case of empirical correlations, the wall heat transfer is described by dimensionless groups and functions of them or simply by a power function of the wall superheat (see eq. 1.1 for an example of a wall superheat power function type). The wall superheat ΔT_{sup}

is defined as the difference between the wall temperature and the saturation temperature of the fluid. Mechanistic models try to describe the underlying phenomena in more detail by taking the underlying physical processes into account.

Steiner (2006) presents the correlation by McAdams et al. (1949) as an archetype for the group of empirical correlations:

$$q_{wall} = 4.77 * \Delta T_{sup}^{3.86}. \tag{1.1}$$

Although, originally proposed for the boiling of subcooled fluids, the amount of subcooling is not considered in these type of correlations. Mechanistic models for subcooled flow boiling, try to isolate as many physical processes as possible and model them separately. This leads to the decomposition of heat fluxes in the following way:

$$q_{wall} = q_{fc} + q_{evap} + q_{quench}. \tag{1.2}$$

With q_{fc} being the heat flux due to single-phase forced convection, q_{evap} the heat flux used for the evaporation of wall adjacent bubbles and q_{quench} is the heat flux used for quenching the bubble area right after the departure of a bubble from its nucleation site. This model, originally proposed by Kurul and Podowski (1991) can be considered as industry standard and is often referred to in the literature as RPI model following its origin in the Rensselaer Polytechnic Institute. This model is implemented in the major commercial and open source CFD codes like Ansys CFX, Starccm+ and OpenFOAM. These separate heat fluxes are modeled with various sub-models for which in return often only empirical formulations are available. These sub-models often contain reference values that are commonly tuned to fit the desired experimental data. One example could be the modeling of the nucleation site density N. In CFX, the model by Lemmert and Chawla (1977) is applied:

$$N = N_{ref} * (\frac{\Delta T_{sup}}{\Delta T_{refN}})^{1.805}. \tag{1.3}$$

Krepper and Rzehak (2011) demonstrates this by varying the reference parameter N_{ref} for the sub-model of nucleation site density in the range of $8e5m^{-2}$ and $3e8m^{-2}$ to match the experimentally measured wall temperature. It is clear that such parameters, which are subject to user input, should be avoided in any numerical code as much as possible. This was one of the reasons for the approach to wall heat flux modeling as presented in this study in chapter 3.

Coupling of System Thermo-Hydraulic (STH) Codes and CFD

The motivation for coupling of a STH-code and CFD comes from the fact, that certain phenomena like thermal stratification, flows through complex geometries occurring in current and future reactor systems, cannot be adequately described by a reduction of the problem to one dimension, while the available computational power is still not sufficient to model a whole reactor system with a 3-dimensional CFD approach. A further need for the simulation of certain parts of a reactor system with CFD instead of a STH code is the pure loss of information in the reduction from 3D to 1D. One example is the radial void fraction distribution even in a simple geometry like a channel or a pipe, which is impossible to obtain in a STH approach, but gives valuable information about the heat transfer process.

Bandini et al. (2015) gives a very recent overview of the activities undertaken in the field of coupling STH codes an CFD codes. The categories needed to classify these coupled code

systems are, according to him, the choice of geometrical domain on which each code acts and the choice of frequency, at which the two codes exchange information. The geometrical coupling can either be done by domain decomposition or by domain overlapping, while the exchange frequency is either one exchange per complete transient simulation or data exchange after every solution time step of each individual code.

In case of domain decomposition, each code acts on different predefined subsets of the complete simulation domain. The codes exchange information at the interfaces between these subsets. In domain overlapping approaches, the complete simulation domain is simulated by the STH code, while a subset of it is calculated by CFD. The results from CFD are used as correction factors for the STH calculation. The frequency of the information exchanges describes the depth of integration of the coupled system. In case of data exchange after complete transients, several repeated runs are necessary to reach a converged state. But the effort needed is less invasive in the two codes. If data exchange at every simulation time-step is desired, a deeper integration of the codes is achieved, but at the cost of more information exchange operations needed. Various STH and CFD codes have been coupled based on the previously described classification and used to recalculated experiments like TALL (Ma et al., 2006) and the Phenix End of life test (Tenchine et al., 2013). A conclusion, which methodology performs better in certain situations, was unfortunately not drawn.

Coolability of IVR systems

The foundation of most work related to the simulation of coolability of IVR systems is the work by Theofanous et al. (1994). He conducted experiments (ULPU-2000) that provide data for the CHF values for a hemisphere submerged in water. From this data, a CHF correlation with its only dependence being the angular position of the hemisphere θ was derived (Theofanous et al., 1997):

$$q_{CHF}(\theta) = 490 + 30.2 * \theta - 8.88 * 10^{-1} * \theta^2 + 1.35 * 10^{-3} * \theta^3 - 6.65 * 10^{-5} * \theta^4. \quad (1.4)$$

This correlation forms the basis of many simulation codes for IVR coolability like in the work of Esmaili and Khatib (2004) or Cao et al. (2015).

Another set of large scale experiments were conducted by CEA and reported by Rouge (1997). Key findings are that the CHF mainly depends on the local mass flow rates. The mass flow rate will be induced by natural circulation in case of a passive IVR system. This indicates the interconnectivity between integral system behavior (natural circulation flow) and CHF limits. Unfortunately, only forced convection experimental results were reported by the authors. Instead of a natural circulation flow, various mass fluxes ranging from $5 - 1800 \frac{kg}{s*m^2}$ were used as boundary conditions for their experimental setup. Another interesting point reported by Rouge (1997), is the large discrepancy between their measured CHF values and data tables by Groeneveld. CHF values taken from the tables overestimate the experimental CHF values by a factor of 2 for low steam qualities and underestimate the CHF by about 20% for high steam qualities.

Esmaili and Khatib (2004) developed a computer code based on one- and two-dimensional models to asses the thermal response of the AP1000 RPV-wall. Two different melt pool configurations were considered. In the first configuration, a two-layer melt pool with a heavy ceramic $UO_2 - ZrO_2 - M_xO_x$ layer beneath a lighter $Fe - Zr$ layer was assumed. In the second configuration, a third heavy metallic layer consisting of $Zr - U - Fe$ under the ceramic layer is assumed forming a three layer configuration. Because of the large uncertainty in the boundary conditions regarding the melt configuration and the resulting

residual heat, the authors used a probabilistic framework to asses the cases with the highest likelihood to occur. The boundary conditions for the case with the highest probability will be used as the boundary conditions in chapter 6 of this study and will be explained there in detail.

Similar one-dimensional analysis of the IVR coolability have been performed by Zhang et al. (2010). The authors developed their own one-dimensional code (IVRASA) and compared their results with the work by Esmaili and Khatib (2004). The results can be considered as similar.

Two-phase natural circulation flow stability in the gap between the RPV-wall and the insulation wall are studied by Guozhi et al. (2013) and Jin et al. (2013) using the RELAP5 system code. Guozhi et al. (2013) studied the effect of the water subcooling on the natural circulation stability and the resulting mass flow rate. The authors varied the subcooling of the water from 45 K to 70 K. A lower subcooling leads to a higher mass flow rate. An increase of subcooling of 5 K leads to a decrease of flow rate of 2%. A critical subcooling is observed. Below a subcooling of 45 K, flow instabilities are reported by the authors for 18.05 MW residual heat and 2 bar surrounding pressure. Jin et al. (2013) studied two-phase natural circulation instabilities for higher thermal loads (40 MW). Here again, a critical subcooling was found, but at a much lower level of 19 K. The authors also found the flow to stabilize again at a very low subcooling of 1 K.

The most recent experimental investigations on the coolability of IVR systems have been conducted by Park et al. (2013). A two-dimensional slice of a half-hemisphere was used as the test section. The heated part of the test section is divided into 4 regions with variable heat fluxes to account for the non-uniformity of the heat flux distribution in the lower head. Water at a subcooling of 2 K or 10 K is injected by a pump at mass fluxes between 50 and 400 $\frac{kg}{m^2 s}$. The heat flux in the last heating region is gradually raised until an excursion in the wall temperature is measured. This heat flux is then reported as the critical heat flux (CHF).

Cao et al. (2015) developed a computer code (Accident Simulation on Pressure vessel-2 Dimensional, ASAP-2D) for the two-dimensional heat flux through the RPV-wall. In this code, a heat flux distribution from a severe accident code like ATHLET-CD has to be supplied at the inner side of the RPV-wall. As a part of the RPV-wall is likely to melt, heat transfer correlations for natural convection are applied if the local temperature exceeds the liquidus temperature of the RPV-wall material. A key finding in this study is that the maximum output heat flux is decreased by 23% when two-dimensional effects are considered. For this reason, the authors recommend to consider 2-D effects when IVR coolability is studied.

Jamet et al. (2015) performed numerical simulations by recalculating experimental data by Dinh et al. (2003) with the Neptune CFD code. These experiments, called ULPU-2400 are the continuation of the work by Theofanous et al. (1994) described above. Neptune is a numerical code that employs a two-fluid Euler-Euler approach. The wall heat flux is modeled with equation 1.2. Global parameters like differential pressure and flow rate were predicted within a range of 10% deviation from the experimental data with the Neptune code. The authors express the need to compare local values like void fraction, bubble diameters and turbulent quantities to complete a validation of the code. Unfortunately, none of these quantities are available at the moment from experimental data.

1.4 Outline

Chapter 2 will cover the theoretical background and present the governing equations used in the following chapters. After a brief introduction to the Navies-Stokes equations for

single-phase flows and two-phase flows, the turbulence models employed in this study will be explained. Special care is taken in explaining the closure models used in the two-phase simulations. As the simulation of the liquid and solid phase transition requires modeling approaches as well, these models will also be presented in chapter 2.

In chapter 3, a novel modeling approach to two-phase flow wall heat transfer at subcooled flow boiling conditions will be presented. The constituting equations of work done in previous studies by other authors will be explained, as they are the basis for the new modeling approach.

The coupling of the system thermal-hydraulic code (STH) ATHLET and the CFD library OpenFOAM will be presented in chapter 4. Here, a brief overview of the coupling methodology will be given. The main focus in chapter 4 is given on the implementation, as this is the defining factor for computational speed and the novelty of the approach. The correctness of the implementation will be shown by calculating simple test cases with the coupled codes, and will be compared with the results with ATHLET standalone calculations.

Chapter 5 will cover the validation of the melting and solidification models used, and the wall heat transfer model developed and implemented in this study.

In chapter 6, the previously explained models for wall heat transfer, liquid to gas and gas to liquid phase change, melting and solidification, as well as the coupled STH and CFD code will be utilized to calculate a prototypical/academic IVR system in the scale of a commercially available PWR. The results will be compared with simulations by Esmaili and Khatib (2004).

The key findings of this study will be summarized and a conclusion is drawn in chapter 7. Still remaining problems will be addressed and suggestions given to further improve upon the topics discussed in the study.

2. Theoretical Background

This chapter covers the theoretical background of heat and mass transfer at first in single-phase flows and then secondly for two-phase flows. Basic modeling assumptions that will be used later on are also explained. In the last part of this chapter, the solution method for the previously described models will be presented.

2.1 Governing Equations

The governing equations of fluid mechanics are based on the principle of conservation of mass, momentum and energy in a particular control volume. They can be found in the common literature of fluid mechanics like in Oertel Jr et al. (2011) or Ferziger and Peric (2012). As different conservation equations are necessary for the assumption of a single phase fluid being present in the computational domain and for the assumption of two-phase flows, the single-phase version will be presented first and the two-phase version will be presented afterwards.

2.1.1 Single-Phase

Conservation of mass is described by the continuity equation

$$\frac{\partial \rho}{\partial t} + \frac{\partial \rho u_i}{\partial x_i} = 0. \tag{2.1}$$

With ρ being the density of the fluid and the velocity vector $u = (u_1, u_2, u_3)^T$ written with the Einstein summation convention.

Conservation of momentum in a particular control volume is described by

$$\frac{\partial \rho u_i}{\partial t} + \frac{\partial \rho u_j u_i}{\partial x_j} = \frac{\partial \tau_{ij}}{\partial x_j} - \frac{\partial p}{\partial x_i} + \rho g_i. \tag{2.2}$$

Acceleration caused by gravity is described by g_i (in direction of x_i) and the pressure by p. τ describes the viscous stress tensor for a Newtonian fluid

$$\tau_{ij} = \mu \left(\frac{\partial u_i}{\partial x_j} + \frac{\partial u_j}{\partial x_i}\right) - \frac{2}{3}\mu\left(\frac{\partial u_i}{\partial x_i}\right)\delta_{ij}. \tag{2.3}$$

The Kronecker delta δ_{ij} is used to address only the diagonal elements of τ and μ is a material property of the fluid that describes its dynamic viscosity.

Conservation of energy in terms of enthalpy h can be written as

$$\frac{\partial \rho h}{\partial t} + \frac{\partial \rho u_i h}{\partial x_i} = \kappa \frac{\partial^2 \rho h}{\partial x_i \partial x_i}. \tag{2.4}$$

κ is the thermal diffusivity of a fluid and defined as the ratio the thermal conductivity λ and the product of density ρ and specific heat capacity c_p

$$\kappa = \frac{\lambda}{\rho c_p}. \tag{2.5}$$

We will neglect any changes in density caused by pressure in the following and use the Boussinesq-Approximation to consider changes in the density caused by temperature gradients solely. Key point of the Boussinesq-Approximation is to neglect the change of density in all terms but the buoyancy term ρg_i in the conservation equation of momentum (equation 2.2). The density is now treated as a function of temperature $\rho(T)$. This density function can be approximated by a linear relationship between the change of temperature and the thermal expansion coefficient β

$$\rho(T) = \rho_0 \cdot (1 - \beta \cdot (T - T_0)). \tag{2.6}$$

Furthermore, we will use from now on the Reynolds averaged form of these equations, also denoted as the Reynolds Averaged Navier-Stokes Equations (RANS). Using the Reynolds averaged form of the Navier-Stokes equations allows the simulation of turbulent flows in reasonable time on computers available today. This is necessary as all cases of interest in this thesis deal with a turbulent flow pattern. Turbulence is characterized by a large variety of scales (in space and time) occurring in an irregular, chaotic and 3-dimensional flow structure. The field variable of interest can be split up into a mean value and its fluctuation counterpart. This method of treating turbulent flows is called Reynolds Decomposition

$$\phi = \bar{\phi} + \phi'. \tag{2.7}$$

These assumptions leads to a simplified set of equations.

For the continuity equation we get

$$\frac{\partial \bar{u}_i}{\partial x_i} = 0. \tag{2.8}$$

For the conservation of momentum

$$\frac{\partial \bar{u}_i}{\partial t} + \frac{\partial \bar{u}_j \bar{u}_i}{\partial x_j} = -\frac{\partial(\frac{\bar{p}}{\rho_0})}{\partial x_i} + \frac{1}{\rho_0} \frac{\partial(\tau_{ij} + \tau_{t,ij})}{\partial x_j} + \frac{\bar{\rho}}{\rho_0} g_i. \tag{2.9}$$

And for the conservation of energy

$$\frac{\partial \bar{h}}{\partial t} + \frac{\partial \bar{h} \bar{u}_j}{\partial x_j} = \frac{\partial(\kappa_{eff} \frac{\partial \bar{h}}{\partial x_k})}{\partial x_k}. \tag{2.10}$$

As a product of the averaging process, two new unknown terms appeared, the turbulent stress tensor $\tau_{t,ij}$ and the effective thermal diffusivity κ_{eff}. The effective thermal diffusivity is the sum of the molecular diffusivity κ and the turbulent diffusivity κ_t

$$\kappa_{eff} = \kappa + \kappa_t. \tag{2.11}$$

$\tau_{t,ij}$ and κ_t are unknown and have to be modeled. Modeling of them will be shown in chapter 2.2 (see eq. 2.19 for $\tau_{t,ij}$ and eq. 2.34 for κ_t). As from here on only averaged quantities will be used, the upper bar symbol will be omitted.

2.1.2 Two-Phase

For the simulation of the two-phase flows, a two-fluid approach (sometimes also referred to as the Euler-Euler Method) as presented by Ishii and Hibiki (2011) will be used. Here the two phases are treated as separate continua that can inter-penetrate each other. The conservation equations are averaged and written for each phase separately, but weighted by their phase fraction α

$$\alpha_c = \frac{V_c}{V_c + V_d}, \ \alpha_d = \frac{V_d}{V_c + V_d}. \tag{2.12}$$

α denotes the probability of the existence of a particular phase at one specific local point and time in the computational domain, V is volume that the particular phase occupies (see Rusche (2003) for a comprehensive overview of resent work related to the development of the two-fluid method). The indices c and d describe if either the continuous or the dispersed phase is refereed to. The averaging procedure introduces a loss of information at the interface between the two phases in the momentum equation. It is therefore necessary to model these interactions called *interfacial momentum transfer terms M* (see 2.3.1).

The two-fluid method is applicable to a wide range of flow regimes. Ishii and Hibiki (2011) classify two-phase flows either by combinations of present phases or by their interface structures. In regards of present phases, we get gas-solid, gas-liquid and liquid-solid mixtures (mixtures with plasma excluded). When classified by interface structure, we get separated flow, mixed flow and dispersed flow.

The continuity equation for the continuous phase including phase change can be written as

$$\frac{\partial \alpha_c}{\partial t} + \nabla \cdot (\alpha_c u_c) = \frac{S_{cd} - S_{dc}}{\rho_c}. \tag{2.13}$$

The phase fraction for the dispersed phase is simply computed as $1 - \alpha_c$. The source terms S_{cd} and S_{dc} describe the change of mass per unit time from one phase to the other. This would be in our case the processes of evaporation at a heated wall or the condensation in the bulk fluid.

Conservation of momentum for the continuous phase would be

$$\frac{\partial \alpha_c \rho_c u_c}{\partial t} + \nabla \cdot (\alpha_c \rho_c u_c u_c) = -\alpha_c \nabla p + \nabla \cdot [\alpha_c (\tau_c + \tau_{t,c})] + M_c + \alpha_c \rho_c g + S_{cd} u_d - S_{dc} u_c. \tag{2.14}$$

The momentum equation of the dispersed phase is exactly the same with the indices c and d exchanged. The conservation equations of momentum have to be solved for both phases. Here the pressure p is assumed to be the same for both phases in each computational cell. M_c stands for the sum of interfacial momentum exchange between the phases. M_c is a modeling term employed to capture the interaction between the two phases and consists of

many sub-models for momentum exchange due to interfacial drag, wall lubrication, virtual mass, turbulent dispersion and lift. A detailed explanation of these models will be given in chapter 2.3.1.

Conservation of enthalpy is written as

$$\frac{\partial \alpha_c \rho_c h_c}{\partial t} + \nabla \cdot (\alpha_c \rho_c u_c h_c) = \alpha_c \frac{Dp}{Dt} - \nabla \cdot [\alpha_c(q_c + q_{c,t})] + S_{cd} h_b - S_{dc} h_c + q_{wall}. \quad (2.15)$$

With the enthalpy of phase c, h_c, molecular heat flux q_c, the turbulent heat flux $q_{c,t}$ and a heat source q_{wall}. Fourier's law of heat conduction relates the molecular heat flux to the thermal conductivity λ_c and the temperature gradient $\frac{\partial T_c}{\partial x}$

$$q_c = -\lambda_c \cdot \frac{\partial T_c}{\partial x}. \quad (2.16)$$

In an analogous way, the turbulent heat flux $q_{c,t}$ is defined as

$$q_c, t = -\lambda_{c,t} \cdot \frac{\partial T_c}{\partial x} \quad (2.17)$$

with the help of the turbulent thermal conductivity $\lambda_{c,t}$. The turbulent thermal conductivity can be related to the turbulent thermal diffusivity in a similar way as the molecular thermal conductivity

$$\lambda_{c,t} = \kappa_{c,t} \rho_c c_{p_c}. \quad (2.18)$$

2.2 Turbulence Modeling

As a result of the Reynolds averaging of the Navier-Stokes equations, two terms, the turbulent stress tensor

$$\tau_{t,ij} = -\rho \overline{u_i' u_j'} \quad (2.19)$$

and the turbulent thermal diffusivity κ_t appeared. As they are unknown, they need to be modeled.

Single-Phase Turbulence

A common way to model the term $\overline{u_i' u_j'}$ is to use an analogy to Newtons approach for the molecular shear stress and relate the turbulent stress tensor to the mean velocity gradients

$$\overline{u_i' u_j'} = \frac{2}{3} k \delta_{ij} - \nu_t \left(\frac{\partial u_i}{\partial x_j} + \frac{\partial u_j}{\partial x_j} \right). \quad (2.20)$$

This approach is known in the literature as the Boussinesq approach. Newly introduced have been here the turbulent kinetic energy

$$k = \frac{1}{2} \overline{u_i u_j} \quad (2.21)$$

and the turbulent viscosity ν_t. A variety of modeling concepts for ν_t exist in the literature. Simple models employ algebraic relations, while more complex models solve transport equations for different field variables related to turbulent quantities. One such modeling

approach relates the turbulent viscosity ν_t to the turbulent kinematic energy k and its dissipation rate ϵ in the following way

$$\nu_t = C_\mu \frac{k^2}{\epsilon}. \tag{2.22}$$

ϵ is defined by

$$\epsilon = \nu \overline{\frac{\partial u_i \partial u_i}{\partial x_j \partial x_j}}. \tag{2.23}$$

In the standard $k - \epsilon$ model by Launder and Spalding (1974), two transport equations are solved, one for k

$$\frac{Dk}{Dt} = \frac{1}{\rho} \frac{\partial(\frac{\mu_t}{\sigma_k} \frac{\partial k}{\partial x_j})}{\partial x_j} + \frac{\mu_t}{\rho} \left(\frac{\partial u_i}{\partial x_j} + \frac{\partial u_j}{\partial x_i} \right) \frac{\partial u_i}{\partial x_j} - \epsilon \tag{2.24}$$

and one for ϵ

$$\frac{D\epsilon}{Dt} = \frac{1}{\rho} \frac{(\frac{\mu_t}{\sigma_\epsilon} \frac{\partial \epsilon}{\partial x_j})}{\partial x_j} + \frac{C_1 \mu_t}{\rho} \frac{\epsilon}{k} \left(\frac{\partial u_i}{\partial x_j} + \frac{\partial u_j}{\partial x_i} \right) \frac{\partial u_i}{\partial x_k} - C_2 \frac{\epsilon^2}{k}. \tag{2.25}$$

With the Lagrangian derivative

$$\frac{D}{Dt} = \frac{\partial}{\partial t} + u_i \frac{\partial}{\partial x_i}. \tag{2.26}$$

Values of the model constants appearing in eq. 2.23 and 2.25 are summarized in table 2.1.

Table 2.1: Values of the modeling constants in the standard $k - \epsilon$ model as in Launder and Spalding (1974).

C_μ	C_1	C_2	σ_k	σ_ϵ
0.09	1.44	1.92	1.0	1.3

The $k-\epsilon$ model is the basis for the turbulence model used for the two-phase flow simulations in this study and also part of the model described below. For the single-phase simulations presented in the following chapters, the $k - \omega$ SST turbulence model by Menter et al. (2003) will be used. This model can be seen as a continuation of the $k - \omega$ model first presented by Wilcox (1988). It uses a zonal approach. The $k-\omega$ model is used in the near wall region and the $k - \epsilon$ is used in the remaining parts of the flow domain. The zonal separation is accomplished by the use of blending functions (see F_1 in eq. 2.29 and F_2 in eq. 2.30). In the $k - \omega$ model, the transport equation for ϵ is replaced by a transport equation the turbulent frequency ω (see eq. 2.29). ω is defined as

$$\omega = \frac{k}{\epsilon}. \tag{2.27}$$

The $k - \omega$ formulation results in a higher accuracy in the near wall region. Eq 2.29 shows unfortunately large sensitivities in the regions apart from the boundary layer of the flow.

This was the main reason for Menter et al. (2003) to combine the two models into one. The final transport equations for k (eq. 2.28) and ω (eq. 2.29) read

$$\frac{\partial \rho k}{\partial t} + \frac{\partial \rho u_i k}{x_i} = \tilde{P}_k - \beta^* \rho k \omega + \frac{\partial [(\mu + \sigma_{k1}\mu_t)\frac{\partial k}{\partial x_i}]}{\partial x_i}, \qquad (2.28)$$

$$\frac{\partial \rho \omega}{\partial t} + \frac{\partial \rho u_i \omega}{x_i} = \frac{\alpha \tilde{P}_k}{\nu_t} - \beta_1 \rho \omega^2 + \frac{\partial [(\mu + \sigma_{\omega 1}\mu_t)\frac{\partial \omega}{\partial x_i}]}{\partial x_i} + 2(1 - F_1)\rho \sigma_{w2} \frac{1}{\omega} \frac{\partial k}{\partial x_i} \frac{\partial \omega}{\partial x_i}. \quad (2.29)$$

The turbulent viscosity is defined here by

$$\nu_t = \frac{\alpha_1 k}{max(\alpha_1 \omega, S_s F_2)}. \qquad (2.30)$$

$\tilde{P}_k$ is the limited production of turbulent kinetic energy, the invariant measure of strain is denoted by S_s, and $F1$ and $F2$ are blending functions. Values of the remaining modeling constants can be found in table 2.2.

Table 2.2: Values of the modeling constants in the $k - \omega$ model as in Menter et al. (2003).

β^*	α_1	β_1	σ_{k1}	$\sigma_{\omega 1}$	α_2	β_2	σ_{k2}	$\sigma_{\omega 2}$
0.09	5/9	3/40	0.85	0.5	0.44	0.0828	1.0	0.856

Another advantage of the $k - \omega$ formulation is the fact that an analytic solution for ω is known in the viscous sub-layer (see eq. 2.31) and in the log layer (see eq. 2.32).

$$\omega_{vis} = \frac{6\nu}{0.75 y^2} \qquad (2.31)$$

$$\omega_{log} = \frac{\sqrt{k}}{C_\mu^{0.25} \kappa y} \qquad (2.32)$$

y is the distance to the wall and κ the von Karman constant with a default value of 0.41. The value of ω in the near wall cell is finally obtained by blending eq. 2.31 and 2.32

$$\omega_{wall} = \sqrt{\omega_{vis}^2 + \omega_{log}^2}. \qquad (2.33)$$

ν_t and k are now defined and can be used in eq. 2.19 to model the turbulent stress tensor $\tau_{t,ij}$.

The remaining unknown is the turbulent thermal diffusivity κ_t. κ_t is modeled with the help of the so called Reynolds Analogy between the transfer of momentum and thermal energy. This assumption holds true for fluids with a Prandtl number Pr in the region of 1. The most simple model for the turbulent thermal diffusivity κ_t is now to define a turbulent Prandtl number Pr_t as

$$Pr_t = \frac{\nu_t}{\kappa_t} \qquad (2.34)$$

and set it to a constant value of 1. As the turbulent kinematic viscosity ν_t is known from the turbulence model described above, it is trivial to computer the turbulent thermal diffusivity from eq. 2.34.

Two-Phase Turbulence

The turbulence model used in this study for the Eulerian two-phase simulations is one of the currently implemented models in OpenFOAM and denoted as *mixture $k - \epsilon$ turbulence model*. It is based on the work of Behzadi et al. (2004). Previous models only provided a transport equation for the turbulent kinetic energy of the continuous phase (k_c), while the turbulent kinetic energy of the dispersed phase (k_d) was computed directly from k_c. In the cases we are looking at in this thesis, the volume fraction of the dispersed phase will be very high. In these cases, the assumption of one phase dominating the turbulent characteristics of the other phase does not hold true anymore. If the phase fraction of the dispersed phase is in the order of 1, it becomes the continuous phase and its turbulence properties determine the turbulence of the other (now dispersed) phase. Apart from these limiting cases, the two phases fluctuate as one unity, which was the reason for Behzadi et al. (2004) to derive transport equations for k and ϵ for a mixture of the two phases.

The mixture properties are defined as a mixture turbulent kinetic energy

$$k_m = (\alpha_c \frac{\rho_c}{\rho_m} + \alpha_d \frac{\rho_d}{\rho_m} C_t^2) k_c \tag{2.35}$$

and a mixture dissipation rate

$$\epsilon_m = (\alpha_c \frac{\rho_c}{\rho_m} + \alpha_d \frac{\rho_d}{\rho_m} C_t^2) \epsilon_c. \tag{2.36}$$

The mixture density ρ_m is defined by

$$\rho_m = \alpha_c \rho_c + \alpha_d \rho_d. \tag{2.37}$$

In eq. 2.37, the density of the dispersed phase (ρ_d) is calculated as an effective density (see Lahey (2005)) with the help of the coefficient of the virtual mass C_{vm} (see 2.63)

$$\rho_{eff,d} = \rho_d + C_{vm} \rho_c \tag{2.38}$$

which is different from the formulation by Behzadi et al. (2004). C_t is the turbulence response coefficient and relates the velocity fluctuations of the dispersed phase to those of the continuous phase

$$Ct = \frac{u'_d}{u'_c}. \tag{2.39}$$

Behzadi et al. (2004) suggest to model C_t as a function of the dispersed phase fraction in the following way

$$C_t(\alpha_d) = 1 + (C_{t0} - 1) e^{-f(\alpha_d)}, \tag{2.40}$$

$$C_{t0} = \frac{3 + \beta_t}{1 + \beta_t + 2\frac{\rho_d}{\rho_c}}, \tag{2.41}$$

and the coefficient β_t as:

$$\beta_t = \frac{2 A_d l_e^2}{\rho_c \nu_c Re_t}. \tag{2.42}$$

Ct_0 is the base response coefficient, which is used in the case of zero phase fraction. l_e is the eddy length scale

$$l_e = C_\mu(\frac{k_c^{1.5}}{\epsilon_c}) \tag{2.43}$$

A_d is a coefficient related to drag and Re_t the turbulence Reynolds number. A_d is defined as

$$A_d = \frac{3\alpha_d\rho_c C_D|u_r|}{4d_b} \tag{2.44}$$

and with the relative velocity u_r, and Re_t as

$$Re_t = \frac{\sqrt{\frac{2k_c}{3}}l_e}{\nu_c}. \tag{2.45}$$

In the transport equations for k_m and ϵ_m, the following relationship is used

$$k_d = C_t^2 k_c, \epsilon_d = C_t^2 \epsilon_c. \tag{2.46}$$

The transport equations for k_m (eq. 2.47) and ϵ_m (eq. 2.48) are very similar to the ones previously described for single-phase flows for k and ϵ.

$$\frac{\partial \rho_m k_m}{\partial t} + \nabla \cdot (\rho_m u_m k_m) = \nabla \cdot \frac{\mu_m^t}{\sigma_m}\nabla k_m + P_k^m - \rho_m\epsilon_m + S_k^m \tag{2.47}$$

$$\frac{\partial \rho_m \epsilon_m}{\partial t} + \nabla \cdot (\rho_m u_m \epsilon_m) = \nabla \cdot \frac{\mu_m^t}{\sigma_m}\nabla \epsilon_m + \frac{\epsilon_m}{k_m}(C_{\epsilon 1}P_k^m - C_{\epsilon 2}\rho_m\epsilon_m) + C_{\epsilon 3}\frac{\epsilon_m}{k_m}S_k^m \tag{2.48}$$

Newly introduced have been here the mixture velocity u_m

$$u_m = \frac{\alpha_c\rho_c u_c + \alpha_d\rho_d u_d C_t^2}{\alpha_c\rho_c + \alpha_d\rho_d C_t^2}, \tag{2.49}$$

the mixture turbulent viscosity μ_m^t

$$\mu_m^t = \frac{(\alpha_c\mu_c^t + \alpha_d\mu_d^t C_t^2)\rho_m}{\alpha_c\rho_c + \alpha_d rho_d C_t^2}, \tag{2.50}$$

The mixture production of turbulent kinetic energy P_k^m

$$P_k^m = \alpha_c P_k^c + \alpha_d P_k^d, \tag{2.51}$$

and finally the source term S_k^m.

Apart from the shear induced turbulence, it is common to add another source of turbulent kinetic energy induced by the presence of the bubbles in the fluid. Here the model by Lahey (2005) is implemented as opposed to the model suggested in Behzadi et al. (2004). This reason for this in unfortunately unknown. The model by Lahey (2005) relates the

bubble induced turbulence $S_{k,bubble}$ to the drag force coefficient C_D, the relative velocity of the two phases u_r and the bubble diameter d_b in the following way

$$S_{k,bubble} = Cp(1 + C_D^{\frac{4}{3}})\alpha_d \frac{|u_r|^3}{d_b} \tag{2.52}$$

Cp is a modeling constant which is calibrated to a value of 0.25 for the flow around a sphere.

2.3 Closure Modeling for two-phase flows

With the presentation of the conservation equation of momentum in an Eulerian two-fluid framework (eq. 2.14), the interfacial momentum exchange term M was introduced. This term as well as the interfacial area A_i between the two phases need additional modeling.

2.3.1 Interfacial Momentum Transfer

M is defined as the sum of different sub-models to retain the information of small scales lost during the averaging process of the conservation equations. Each of these forces is caused by a different physical process. The exact expression for M is still a matter of discussion in the literature, as well as the often empirical correlations that describe the particular forces. Recent approaches try to consolidate the vast number of modeling options (see Rzehak and Krepper (2015)) available in the literature. The authors consider drag-, lift-, wall-, turbulent dispersion- and virtual mass forces. This way M can be written for both phases as

$$M = M^{drag} + M^{lift} + M^{wall} + M^{turbulentDispersion} + M^{virtualMass}. \tag{2.53}$$

Drag Force

The drag force acting on a bubble is caused by the resistance of the surrounding fluid, when the bubble moves with a relative velocity through the liquid. An expression for the momentum source caused by drag is given as

$$M_c^{drag} = -M_d^{drag} = \frac{3}{4d_b}C_D\rho_c\alpha_d|u_r|u_r \tag{2.54}$$

A very basic model for the drag force coefficient was derived by Schiller and Naumann (1933) with

$$C_D = min(\frac{24}{Re}(1 + 0.15Re^{0.687}), 0.44), \tag{2.55}$$

Ishii and Zuber (1979) suggest a model for C_D which considers different possible shapes of a bubble, depending on the Reynolds- and the Eötvös Number (Eo)

$$C_D = max(C_{D,sphere}, min(C_{D,ellipse}, C_{D,cap})), \tag{2.56}$$

with

$$C_{D,sphere} = \frac{24}{Re}(1 + 0.1Re^{\frac{3}{4}}), \ C_{D,ellipse} = \frac{2}{3}\sqrt{Eo}, C_{D,cap} = \frac{8}{3}. \tag{2.57}$$

Lift Force

When a vapor bubble moves through velocity gradients of the continuous phase, a so-called lift force acts on it. This lift force is given as

$$M_c^{lift} = -M_d^{lift} = C_L \rho_c \alpha_d u_r \times rot(u_c). \tag{2.58}$$

An expression for the lift coefficient C_L for high void fractions is provided by Behzadi et al. (2004)

$$C_L = 6.51 \cdot 10^{-4} \alpha_d^{-1.2} \tag{2.59}$$

with a maximum value of 0.25.

Wall Force

The wall force (or wall lubrication force) acts on a bubble only in the vicinity of a wall. Antal et al. (1991) suspect that the drainage rate between the bubble and the wall is slower than on the opposite site of the bubble. This asymmetry causes a force acting on the bubble and pushing it away from the wall. Unfortunately no analytical expression exists for this phenomena at present. Antal et al. (1991) present a form of the wall force which was deduced from a two dimensional solution of the flow between a cylinder and a wall

$$M_c^{wall} = -M_d^{wall} = -C_{wl} \alpha_d \rho_c |u_r - (u_r n)n|^2 n, \tag{2.60}$$

with the normal vector n pointing away from the wall. The wall force coefficient C_{wl} is modeled as

$$C_{wl} = max(0, \frac{C_{w1}}{d_b} + \frac{C_{w2}}{y_w}). \tag{2.61}$$

y_w is the shortest distance to the next wall. The model coefficients C_{w1} and C_{w2} are given in table 2.3.

Table 2.3: Model constants of the wall lubrication model by Antal et al. (1991)

C_{w1}	C_{w2}
-0.01	0.05

Turbulent Dispersion Force

The turbulent dispersion force is a result from the turbulence of the continuous phase transporting particles or bubbles of the dispersed phase from regions of high dispersed phase concentrations to lower ones (see the proportionality of the net force with the gradients of the phase fractions in eq. 2.62). The Favre averaged drag model by Burns et al. (2004) uses Favre averaging of the drag force to compute the turbulent dispersion force. The model finally reads

$$M_c^{turbulentDispersion} = -M_d^{turbulentDispersion} = C_{TD} C_D \frac{\nu_t}{\sigma_t} (\frac{\nabla \alpha_d}{\alpha_d} - \frac{\nabla \alpha_c}{\alpha_c}). \tag{2.62}$$

C_{TD} is a model constant with the value of 1 and σ_t is the turbulent Schmidt number with a value of 0.9.

Virtual Mass Force

The origin of the virtual mass force (eq. 2.63) comes from that fact that if a dispersed particle is accelerated in a continuous phase, a small part of the continuous phase has to be accelerated as well. For this reason, the virtual mass force is neglected by many authors (see Yamoah and Martínez (2015) or Frank et al. (2008)) in steady-state simulations. In case of this study, bubbles will be generated by nucleation in a subcooled continuous liquid phase surrounding them. They will be accelerated by buoyancy forces as well as by a source term in the momentum equation due to phase change.

$$M_c^{virtualMass} = -M_d^{virtualMass} = C_{vm}\rho_c\alpha_d(\frac{D_d u_d}{Dt} - \frac{D_c u_c}{Dt}). \tag{2.63}$$

Rzehak and Krepper (2015) confirmed the findings of previous studies that a constant value of the virtual mass coefficient C_{vm} of 0.5 can be assumed.

2.3.2 Interfacial Area Concentration

The relation between the interfacial area A_i separating the two phases and the size of the volume V defines the interfacial area concentration a_i. If we assume a constant bubble diameter d_b and a total of n bubbles consuming the volume $V_{bubbles}$ in the volume V, we get the relation

$$a_i = \frac{A_i}{V} = \frac{n\pi d_b^2}{n\pi\frac{d_b^3}{6}}\frac{V_{bubbles}}{V} = \frac{6\alpha}{d_b}. \tag{2.64}$$

Yao and Morel (2004) derived a transport equation for the interfacial area concentration. The authors did not only consider mechanical effects on the evolution of the interfacial area concentration, but also the creation and destruction of area density by nucleation and condensation. By combining the continuity equation with phase change (eq. 2.13) and the transport equation for a_i derived by previous authors (see Wu et al. (1997)), their transport equation reads

$$\frac{\partial a_i}{\partial t} + \nabla \cdot (a_i u_i) = \frac{2}{3}\frac{a_i}{\alpha\rho_v}(S_{phase} - \alpha\frac{d\rho_v}{dt}) + \frac{36\pi}{3}(\frac{\alpha}{a_i})^2(\phi^{CO} + \phi^{BK}) + \pi d_w^2\phi^{NUC}. \tag{2.65}$$

S_{phase} is the net phase change by nucleation and condensation. All variables in 2.65 are available from the governing equations of the Eulerian two-fluid model (see eq. 2.13 and eq. 2.2) except from the source term caused by bubble coalescence ϕ^{CO}, bubble breakup ϕ^{BK} and nucleation ϕ^{NUC}.

The modeling of both mechanical source terms ϕ^{CO} and ϕ^{BK} follows the same principle. A breakup (or coalescence) frequency $f_{BK,CO}$ and an efficiency $\eta_{BK,CO}$ for the process is defined as

$$\phi^{CO} = f_{CO}n\eta_{CO}, \ \phi^{BK} = f_{BK}n\eta_{BK} \tag{2.66}$$

with the number of bubbles in a unit volume n. The frequency can be split up into an interaction and free traveling part

$$f_{BK,CO} = \frac{1}{T_{BK,CO}}, \ T_{BK,CO} = T_{BK,CO,I} + T_{BK,CO,TF}. \tag{2.67}$$

The coalescence frequency is modeled under the assumption that binary bubble collisions are more likely to happen than collisions of three or more bubbles. If the further assumption of a single bubble size per unit volume is employed the frequency of bubble collisions can be written as

$$f_{CO} = \frac{\pi}{4} n^2 d_b^{\frac{7}{3}} \epsilon^{\frac{1}{3}}. \tag{2.68}$$

This leads to the free traveling time

$$T_{CO,FT} = \frac{n}{2f_{CO}} = \frac{1}{3} \frac{d_b^{\frac{2}{3}}}{\alpha \epsilon^{\frac{1}{3}}}. \tag{2.69}$$

The modeling of the coalescence interaction time $T_{CO,I}$ is based on the film thinning model. The assumption here is that two bubbles will coalesce if their contact time is larger than the film drainage time. With an empirical expression for the film drainage time and an initial film thickness h_o of 10^{-4} m and a critical film thickness h_{cr} of 10^{-8} m, the following expression for the interaction time due to bubble bubble collision is obtained

$$T_{CO,I} = 0.814 \sqrt{\frac{\rho_l d_b^3}{\sigma}}. \tag{2.70}$$

The efficiency is estimated to have an exponential form of

$$\eta_{CO} = exp(-\frac{T_{CO,I}}{\tau_c}). \tag{2.71}$$

τ_c is the characteristic time of eddies which have the same size as the bubbles.

The final source for collision induced bubble coalescence reads

$$\phi^{CO} = -K_{c1} \frac{\epsilon^{\frac{1}{3}} \alpha^2}{d_b^{\frac{11}{3}}} \frac{1}{g(\alpha) + K_{c2}\alpha\sqrt{\frac{We}{We_{cr}}}} \cdot exp(-K_{c3}\sqrt{\frac{We}{We_{cr}}}). \tag{2.72}$$

$g(\alpha)$ (see eq. 2.73) is a limiting function. In cases of the void fraction reaching a critical value α_{max} the maximum packing of bubbles in a unit volume is reached and the bubbles start to touch each other reducing their free traveling time to 0 s.

$$g(\alpha) = \frac{\alpha_{max}^{\frac{1}{3}} - \alpha^{\frac{1}{3}}}{\alpha_{max}^{\frac{1}{3}}}, \quad \alpha_{max} = \frac{\pi}{6} \tag{2.73}$$

The Weber number We is defined as the ratio between inertial and the surface energy

$$We = \frac{\rho_l u^2 d_b}{\sigma}. \tag{2.74}$$

σ is the surface tension of the fluid. We_{cr} is a constant called the critical Weber number. Values of the modeling constants and the critical Weber number in eq. 2.72 are given in table 2.4.

Table 2.4: Model constants of the interfacial area concentration coalescence source term due to binary bubble collision by Yao and Morel (2004).

K_{c1}	K_{c2}	K_{c3}	We_{cr}
2.86	1.922	1.017	1.24

While the root cause of bubble coalescence was interaction between two bubbles, it is assumed that the breakup of bubbles is caused by the interaction between bubbles and turbulent eddies. Only eddies with a size comparable to the bubble diameter can lead to a breakup of a bubble. With the total number of eddies in a unit control volume known, the collision frequency f_B between bubbles and eddies becomes

$$f_{BK} = \frac{n}{T_{BK,TF}} = C_b \frac{\epsilon^{\frac{1}{3}}}{d_b^{\frac{11}{3}}} \alpha(1-\alpha). \tag{2.75}$$

C_b is a constant with the value 1.6. The breakup interaction time due to turbulence $T_{BK,I}$ is obtained from a modal analysis of an oscillating bubble. The second mode of the natural frequency, under the assumption that the vapor density is much lower than then liquid density, is given as

$$f_2 = 1.56\sqrt{\frac{\sigma}{\rho_l d_b^3}} = \frac{1}{T_{BK,I}}. \tag{2.76}$$

With the breakup efficiency η_{BK} defined as

$$\eta_{BK} = exp(-\frac{We_{cr}}{We}) \tag{2.77}$$

the final expression for the source term due to bubble breakup is obtained (see eq. 2.78 and models constants in table 2.5).

$$\phi_{BK} = K_{b1} \frac{\epsilon^{\frac{1}{3}} \alpha(1-\alpha)}{d_b^{\frac{11}{3}}} \frac{1}{1 + K_{b2}(1-\alpha)\sqrt{\frac{We}{We_{cr}}}} \cdot exp(-\frac{We_{cr}}{We}) \tag{2.78}$$

Table 2.5: Model constants of the interfacial area concentration breakup source term due turbulent breakup by Yao and Morel (2004).

K_{b1}	K_{b2}
1.6	0.42

2.4 Empirical correlations in STH approach

In the one-dimensional system thermal-hydraulic (STH) approach employed for the large scale parts in the coupled system, the same conservation equations as described above (see 2.1) are used. The main difference is that the dimension of the partial differential equations is reduced to one and that the pressure loss and the heat transfer is modeled with empirical correlations.

Empirical Correlations for Pressure Drop

The frictional pressure drop Δp_{fric} (see eq. 2.79) in a pipe consists according to Lerchl (2012) of two components. The pressure loss due to wall friction Δp_{wall} and the form pressure loss Δp_{form} due to changes in the geometry, like bendings or change of the cross-sectional area.

$$\Delta p_{fric} = \Delta p_{wall} + \Delta p_{form} \tag{2.79}$$

The pressure loss due to wall friction is defined as

$$\Delta p_{wall} = -kG|G| \tag{2.80}$$

with

$$k = \lambda_{f,liquid} \frac{L}{d_h A^2} \frac{1}{2\rho_{liquid}} C^\phi. \tag{2.81}$$

$\lambda_{f,liquid}$ is the wall friction coefficient for the liquid phase and C^ϕ is the two-phase friction multiplier, accounting for additional pressure losses due to the presence of a second phase. d_h is the hydraulic diameter of the flow domain, A is the flow area and G the mass flow rate. The wall friction coefficient λ_f and the two-phase friction multiplier C^ϕ need to be modeled. For laminar flow, the Hagen-Poiseuille equation is used to determine $\lambda_{f,lam}$

$$\lambda_{f,lam} = \frac{64}{Re}, \tag{2.82}$$

and for turbulent flow the Colebrook correlation with

$$\frac{1}{\sqrt{\lambda_{f,turb}}} = 2log(\frac{2.51}{Re\sqrt{\lambda_{f,turb}}} + 0.27\frac{r_{rough}}{d_h}). \tag{2.83}$$

r_{rough} is the absolute wall roughness. The two-phase friction multiplier C^ϕ is modeled with the Martinelli-Nelson (Martinelli and Nelson (1948)) model. Here an interpolation of table files is used to get the correct value of C^ϕ instead of solving an empirical correlation. C^ϕ depends on the steam quality and the pressure. C^ϕ gets larger with larger steam qualities and lower pressures.

Empirical Correlations for Heat Transfer

The wall heat transfer is also modeled by means of empirical correlations. With Newtons law of heat transfer (see eq. 2.84) a heat transfer coefficient htc is defined as a constant of proportionality between the applied wall heat flux and the temperature difference between the wall and the bulk fluid.

$$q = htc(T_{wall} - T_{bulk}) \tag{2.84}$$

The heat transfer coefficient htc is determined by the well known Dittus-Boelter correlation

$$htc = 0.023\frac{\lambda}{d_h}Re^{0.8}Pr^{0.4}. \tag{2.85}$$

This correlation is valid for turbulent single-phase forced convection heat transfer for fluids with a Prandtl number in the region of 1.

For the heat transfer at subcooled nucleate boiling conditions, ATHLET uses a modified version of the Chen correlation (see Lerchl (2012) and Collier and Thome (1996)). This correlation is also the basis of the model further developed in this study and will be explained in detail in chapter 3.

2.5 Melting and Solidification

The RPV wall, reactor core and its support structures are, under nominal operation conditions, all well below their respective melting temperatures. In case of a severe accident, these components can heat up above their melting temperature and potentially partially or completely melt. As a result, their internal mode of heat transfer changes from pure heat conduction to a mixture of convection and conduction. It is important to know which parts of the system are in solid and which in liquid state in order to apply the appropriate governing equations. To gain this information, a *fixed grid enthalpy* model proposed by Voller and Prakash (1987) and later refined by Swaminathan and Voller (1992) will be used. The key point of this model is that the boundary between solid and liquid parts in the domain are obtained by adapting a common set of governing equations as opposed to moving the grid with the liquid-solid boundary. The presence of the solid phase is modeled with a porous media approach in the momentum equation and a source term in the enthalpy equation to account for the thermal energy consumed or released due to phase change. The melting takes place at a fixed melting temperature T_{melt}. This is a modeling assumption that holds true for the melting of pure material, but might be questionable for binary alloys. The solid fraction β_{solid} is computed in an explicit manner

$$\beta_{solid} = \beta_{solid,old} + \frac{c_p(T - T_{melt})}{L}. \tag{2.86}$$

L is the latent heat of solidification. In case of complete solidification, we expect the velocity to be zero, while we expect no influence of the solidification process on the velocity in parts of pure melt. For cases in between the two states ($0 < \beta_{solid} < 1$), the flow is assumed to be governed by Carman-Koseny equation, a form of the better known Darcy equation

$$\nabla p = -C_u \frac{(1 - \beta_{solid})^2}{\beta_{solid}^3} u. \tag{2.87}$$

From eq. 2.87, the porosity source term for the momentum equation can be derived as

$$S_{m,pc} = -u C_u \frac{(1 - \beta_{solid})^2}{\beta_{solid}^3 + c_n}. \tag{2.88}$$

C_u is a constant with a recommended value of $1.6e3$ and c_n is purely used to avoid division by 0 and set to a small value (eg. 0.001). The source term in the enthalpy equation due to phase change $S_{h,pc}$ is proportional to the rate of change as well as the latent heat consumed or released by the process

$$S_{h,pc} = L \frac{\partial \rho \alpha}{\partial t}. \tag{2.89}$$

2.6 Discretization in Time and Space

The discretization method for the solution of the previously described transport equations employed in this thesis is the Finite Volume Method (FVM). The discretization is required to transform the partial differential equations into a set of linear algebraic equations that can be solved by iterative methods on computers. Detailed explanation of the FVM can be found in many standard books on computational fluid dynamics like Ferziger and Peric (2012) or in De Villiers (2007). The discretization process of the FVM is now explained for a solution variable ϕ, starting from the conservation equation of ϕ in its integral form and with Gauss's theorem already applied

$$\frac{\partial}{\partial t} \int_\Omega \rho\phi d\Omega + \int_{S_s} \rho\phi u \cdot n dS_s = \int_{S_s} \Gamma\nabla\phi \cdot n dS_s + \int_\Omega S_\phi d\Omega. \tag{2.90}$$

The computational domain is divided into cells of arbitrary shapes. These cells consist of a cell center P and a number of enclosing cell faces with the surface S_s. Ω is the volume of the cell and n its outwards pointing unit normal vector. Equation 2.90 has to be solved for each individual cell. The surface and volume integrals of 2.90 need to be approximated in order to compute them.

Approximation of the Surface Integrals

The approximation of the surface integrals is based on the fact that the flux of ϕ through one cell has to be the same as the sum of the fluxes through each of the cell faces

$$\int_S f dS_s = \sum_k \int_{S_sk} f dS_s. \tag{2.91}$$

In eq. 2.91, k is the k-th face of the cell and f is either the part of the convective term ($\rho\phi u \cdot n$) or the part of the diffusive term ($\Gamma\nabla\phi \cdot n$). In order to evaluate the surface integral in 2.91, f would have to be known on each face, but is only available at the cell center P. In a first step, the surface integral on the face k is approximated through the midpoint rule

$$F_k = \int_{S_sk} f dS_s \approx f_k S_{sk}. \tag{2.92}$$

Here the integral is simply approximated as the product of the integrand at the face center f_k and the face area S_{sk}. The second step is to get the face centered value f_k by interpolation.

Interpolation of Face Values

A popular interpolation scheme is the *upwind interpolation*. Here the value at the cell face center is simply assumed to be the same as the one in the cell center upstream of the face

$$\phi_e = \begin{cases} \phi_P & \text{for } (u \cdot n)_e > 0 \\ \phi_E & \text{for } (u \cdot n)_e < 0. \end{cases} \tag{2.93}$$

ϕ_e is the face center value of ϕ on the east side face of the cell with the center P and ϕ_E is the value of ϕ in the cell center of the east neighbor cell of the cell with the center P. This interpolation scheme is first order accurate and very stable but numerically diffusive.

A more accurate interpolation scheme is the *linear interpolation* between two neighboring cell centers. On a Cartesian grid the face center value ϕ_e could be written as

$$\phi_e = \phi_E \lambda_e + \phi_P (1 - \lambda_e). \tag{2.94}$$

With the linear interpolation factor λ_e

$$\lambda_e = \frac{x_e - x_P}{x_E - x_P}. \tag{2.95}$$

$(x_E - x_P)$ is the distance between the two cell centers and $(x_e - x_P)$ is the distance between the face center and the cell center of the cell P. This interpolation scheme is second order accurate and can thus produce oscillating results.

Approximation of the Volume Integrals

The approximation of the volume integrals in eq. 2.90 is done in a similar as the approximation of the surface integrals with the midpoint rule. Here the volume integral is approximated as the product of the integrand in the center of the cell and the volume of the cell

$$\int_\Omega S_\phi d\Omega \approx S_{\phi,P} \Delta\Omega. \tag{2.96}$$

$S_{\phi,P}$ is the value of S_ϕ in the cell center P. In contrast to the approximation of the surface integrals, no interpolation is necessary as all other variables are available in the cell center P.

Temporal Discretization

In addition to the spacial discretization described above, a temporal discretization is necessary as well. The special property of time, having only one direction of influence, is taken into account in the temporal discretization methods, the so-called *marching methods*. The Euler implicit scheme uses the value of ϕ at a new time step $\phi^n = (t + \Delta t)$ and at an old time step $\phi^o = \phi(t)$ to discretize the term

$$\frac{\partial}{\partial t} \int_\Omega \rho\phi d\Omega = \frac{(\rho_P \phi_P \Omega)^n - (\rho_P \phi_P \Omega)^o}{\Delta t}. \tag{2.97}$$

Summary

In summary the convective, diffusive and source term in eq. 2.90 are approximated as

$$\int_\Omega \nabla \cdot (\rho\phi u) d\Omega = \sum_k (S_{sk} \cdot u)_k (\rho\phi)_k = \sum_k F_V (\rho\phi)_k, \tag{2.98}$$

$$\int_\Omega \nabla \cdot (\Gamma\nabla\phi) d\Omega = \sum_k S_{sk} \cdot (\Gamma\nabla\phi)_k, \tag{2.99}$$

$$\int_\Omega S_\phi(\phi) d\Omega = S_{\phi,P} \Delta\Omega. \tag{2.100}$$

With the volume flux F_V

$$F_V = S_s * u. \tag{2.101}$$

3. Modeling of Two-Phase Flow Wall Heat Transfer

Kolev (1995) describes nucleate boiling as the most investigated phenomena in thermal science in the last 60 years. Despite all these efforts made in the past, a model on which the scientific community agrees on is still to be established. In this chapter a phenomenological description of the physical processes taking place during subcooled nucleate boiling will be given. After this the development of a new model based on previous studies is shown. The conclusion of this chapter is the implementation of said model in the 3- dimensional CFD framework.

3.1 Phenomenological Description of Flow Boiling

A descriptive and simple description of nucleate boiling is given by Dhir (1991). It starts with the basic assumptions of a solid surface being in contact with a liquid. At first the solid surface and the liquid are in thermal equilibrium. With an increase of heat flux on the surface, the mode of convective heat transfer is engaged. The fluid is set to motion either by buoyancy or by an external source driving a pressure difference. It can be experimentally observed that at a further increase of heat flux at some point, bubbles occur randomly on the heated surface. It was later found out that the bubbles originate at surface-impurities like scratches or small holes on the heated surface. These back than called *dark holes* are now termed as *nucleation sites* in the modern literature.

In figure 3.1 the fluid bulk temperature T_{bulk} and the temperature of the heated surface T_{wall} are compared qualitatively along the flow path of a pipe or channel, which is heated with a constant heat flux. The interesting feature of subcooled nucleate flow boiling lies in the increase of the heat transfer coefficient along the pipe. The total heat transfer coefficient htc can he expressed with Newtons law of cooling (2.84) solved for the heat transfer coefficient

$$htc = \frac{q}{T_{wall} - T_{bulk}}. \tag{3.1}$$

As the first bubbles are created, the rise of wall temperature gets to a halt. While the heat flux is constant and the bulk temperature keeps on increasing until close to the saturation temperature of the fluid, the denominator of eq. 3.1 becomes smaller and thus the heat transfer coefficient becomes larger. This increase of heat transfer coefficient makes this mode of heat transfer so appealing for the cooling of system components of many kinds.
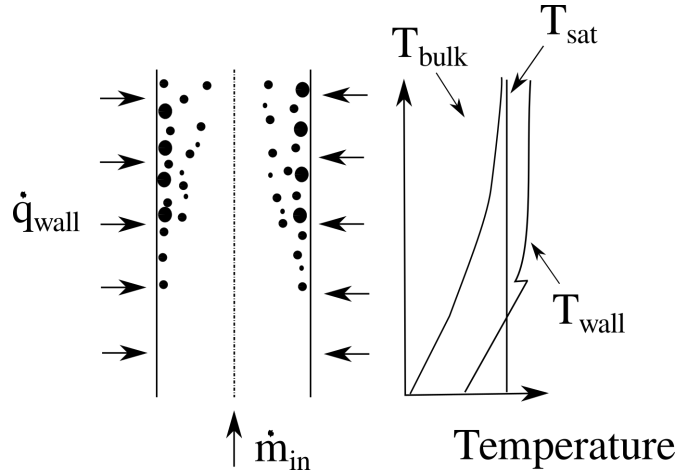
Figure 3.1: Evolution of the wall and bulk fluid temperature along a pipe in subcooled nucleate flow boiling.

3.2 Flow Boiling Model Development

The basis for the model developed in this thesis is the approach presented by Chen (1966). This model, despite its age, can still be considered state of the art, as it is the standard model in many modern 1D STH codes like ATHLET (see Lerchl (2012)). It is based on the assumption that the complex heat transfer phenomena can be broken down into two parts. One part is similar to forced convection heat transfer and another part is responsible for the generation of the bubbles at the nucleation sites of the heated surface. Chen (1966) describes these two parts as macroscopic h_{mac} and microscopic h_{mic} heat transfer coefficients, which can be easily summed up to form the total heat transfer coefficient htc

$$htc = h_{mac} + h_{mic}. \tag{3.2}$$

For the macroscopic heat transfer coefficient h_{mac}, Chen (1966) used the Dittus Boelter equation (see 2.85) multiplied by a factor F_{conv}

$$h_{mac} = \frac{\lambda}{d} 0.023 Re^{0.8} Pr^{0.4} F_{conv}. \tag{3.3}$$

The factor F_{conv} was introduced to account for the enhanced convective heat transfer due to bubble motion at high steam qualities. In the regime of subcooled nucleate flow boiling this factor is always in the region of 1 and can thus be safely neglected as suggested by Collier and Thome (1996).

The microscopic heat transfer coefficient h_{mic} is based on the work by Forster and Zuber (1955) in the Chen (1966) model. Forster and Zuber (1955) showed, by solving the Rayleigh equation (eq. 3.4), that the product of bubble radius r_b and the bubble growth rate $\dot{r}_b$ is constant for a given superheat in case of pool boiling.

$$r_b \ddot{r}_b + \frac{3}{2} \dot{r}_b^2 + \frac{2\sigma}{\rho_l r_b} = \frac{p_v - p_\infty}{\rho_l} \tag{3.4}$$

In figure 3.2, the temperature boundary layer of pool and flow boiling are qualitatively compared. Chen (1966) argued that in both cases the superheat is not constant. This led him to the introduction of an effective superheat ΔT_e. The difference between this
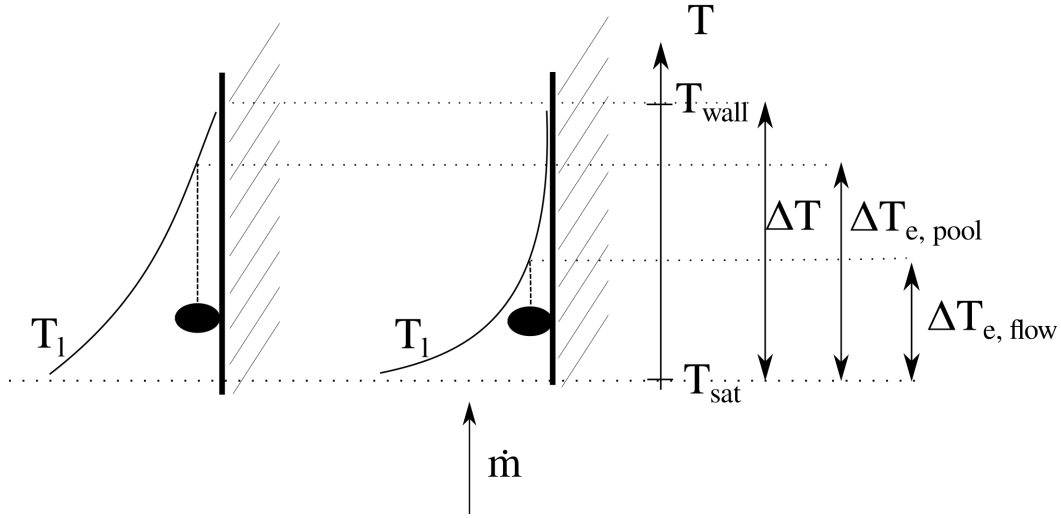
Figure 3.2: Comparison of temperature boundary layer between pool boiling (left) and flow boiling (right) according to Chen (1966). Graphic from Sonntag and Cheng (2016).

effective super heat ΔT_e and the actual wall superheat ΔT is small in case of pool boiling so that it can be neglected, but not so in case of flow boiling.

With the help of the effective super heat ΔT_e and effective saturation pressure difference Δp_e the microscopic heat transfer coefficient becomes

$$h_{mic} = 0.00122(\frac{\lambda_l^{0.79} c_{p,l}^{0.45} \rho_l^{0.49} g^{0.25}}{\sigma^{0.5} \mu_l^{0.29} i^{0.24} \rho_v^{0.24}})(\Delta T_e)^{0.24}(\Delta p_e)^{0.75}. \tag{3.5}$$

To express the effective super heat ΔT_e and the effective saturation pressure difference Δp_e, a suppression factor S_{total} is introduced

$$S_{total} = (\frac{\Delta T_e}{\Delta T})^{0.99}. \tag{3.6}$$

S_{total} is defined as the ratio of effective superheat and the actual superheat. The relation between the effective superheat temperature and the effective saturation pressure difference is establish with the Clausius Clapeyron equation

$$S_{total} = (\frac{\Delta T_e}{\Delta T})^{0.24}(\frac{\Delta p_e}{\Delta p})^{0.75}, \tag{3.7}$$

$$\Delta p = \frac{L}{(\frac{1}{\rho_v} - \frac{1}{\rho_l})T_{sat}}T_{sup}. \tag{3.8}$$

Eq. 3.5 combined with eq. 3.8 leads to the final expression for the microscopic heat transfer coefficient in the Chen (1966) model

$$h_{mic} = 0.00122(\frac{\lambda_l^{0.79} c_{p,l}^{0.45} \rho_l^{0.49} g^{0.25}}{\sigma^{0.5} \mu_l^{0.29} L^{0.24} \rho_v^{0.24}})(\Delta T)^{0.24}(\Delta p)^{0.75} S_{total}. \tag{3.9}$$

The suppression factor S_{total} can be seen as a blending factor between pool and flow boiling. It approaches 1 in pool boiling conditions (zero flow rate) and zero at infinite flow rate. It can be expressed as a function of the local two-phase Reynolds number only. Values for S_{total} were obtained empirically from experimental data.

The Chen correlation is valid for *saturated* flow boiling of water in tubes and annular geometries. Chen also validated his correlation against organic fluids, which are of no relevance for this study. It be extended to a subcooled nucleate boiling regime as suggested by Collier and Thome (1996)

$$q = h_{mic}(T_{wall} - T_{sat}) + h_{mac}(T_{wall} - T_l). \tag{3.10}$$

This model as presented until here is implemented in 1D STH codes like ATHLET (see Lerchl (2012)) to predict the heat transfer coefficients at saturated and subcooled flow boiling conditions. This is possible as it only depends on material properties and integral flow parameters like Reynolds number and the bulk fluid temperature. In a 3-dimensional fluid domain of arbitrary geometry, the meaning of a bulk temperature and a Reynolds number become questionable. Steiner et al. (2005) addressed this issue and proposed the so called *Bubble Departure Lift-off* (BDL) model. His idea was to free the suppression factor S_{total} from the dependency of the Reynolds number and describe it purely with properties available in the near wall cell of the computational domain. This gives the model on the one hand a more physical sound base and on the other makes it possible to implement the suppression factor S in 3D CFD codes.

Steiner et al. (2005) suggested to split S_{total} into two parts. One part suppresses the microscopic heat transfer because of subcooling in the boundary layer S_{sub} and the other part S_{flow} is defined as the ratio of bubble departure radius and the bubble lift off radius

$$S_{total} = S_{sub}S_{flow}. \tag{3.11}$$

The suppression due to subcooling is a simple measure for the subcooling in the boundary layer near the heated wall and defined as

$$S_{sub} = \frac{T_{wall} - T_{sat}}{T_{wall} - T_l}. \tag{3.12}$$

T_l in equation 3.12 is implemented, as the fluid temperature in the first cell center next to the heated wall, in this study.

The flow induced suppression factor S_{flow}

$$S_{flow} = \frac{r_{dep}}{r_{lift}} \tag{3.13}$$

accounts for the fact, that bubbles slide along the heated surface after detachment from their nucleation site before they finally lift off into the bulk fluid. To determine the bubble departure and lift-off radius, Steiner et al. (2005) used a force balance proposed by Zeng et al. (1993).
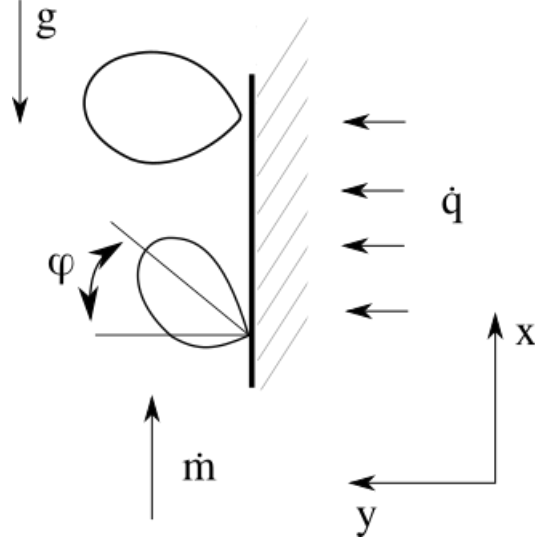
Figure 3.3: Bubble departure, sliding and lift-off from a heated surface at flow boiling conditions. Graphic from Sonntag and Cheng (2016).

Figure 3.3 illustrates the process of bubble departure and lift-off from a heated surface. At the moment of departure from its nucleation site, the bubble is inclined by the angle ϕ, and a force balance of the form

$$\sum F_x = F_{byc} + F_d + F_{du} \cdot sin(\phi) = 0 \qquad (3.14)$$

$$\sum F_y = F_{sl} + F_{du} \cdot cos(\phi) = 0 \qquad (3.15)$$

can be written in the x and y directions.

Buoyancy Force

The buoyancy force acting on the bubble is

$$F_{byc} = \frac{4}{3}r^3\pi g(\rho_l - \rho_v). \qquad (3.16)$$

Drag Force

The drag force F_d and the shear lift force F_{sl} are given by Klausner et al. (1993) as

$$F_d = 6\pi\mu_l u_r r(\frac{2}{3} + ((\frac{12}{Re_{nb}})^n + 0.796^n)^{-\frac{1}{n}}), \qquad (3.17)$$

Shear Lift Force

$$F_{sl} = \frac{1}{2}C_l\rho_l u_r^2\pi r^2. \qquad (3.18)$$

Re_{nb} is the bubble Reynolds number

$$Re_{nb} = \frac{\rho_l u_r 2r}{\mu_l}, \qquad (3.19)$$

n an empirical constant with the value of 0.65, u_r the relative velocity ($u_r = u_l - u_v$) and C_l the lift coefficient. The shear lift coefficient C_l is calculated as suggested by Situ et al. (2005) as a function of the shear rate G_s and the bubble Reynolds number Re_{nb}

$$C_l = 3.877 G_s^{0.5} (Re_{nb}^{-2} + 0.014 G_s^2)^{0.25}. \tag{3.20}$$

The shear rate G_s is defined as

$$G_s = |\frac{du_l}{dx}| \frac{r}{u_r}. \tag{3.21}$$

The near wall velocity gradient $\frac{du_l}{dx}$ is calculated with the help of the logarithmic law of the wall

$$u^+ = \frac{1}{\kappa} ln x^+ + C^+. \tag{3.22}$$

The dimensionless velocity u^+ is the ratio between the velocity parallel to the wall of x and the friction velocity u_τ

$$u^+ = \frac{u_l}{u_\tau} = \frac{u_l}{\sqrt{\tau_w/\rho_l}} \tag{3.23}$$

and the dimensionless distance to the wall x^+ is

$$x^+ = \frac{x u_\tau}{\nu_l}. \tag{3.24}$$

The near wall velocity gradient $\frac{du_l}{dx}$ can now be expressed with eq. 3.22 as

$$\frac{du_l}{dx} = \frac{u_\tau^2}{u_l} \frac{du^+}{dx^+} = \frac{u_\tau^2}{u_l} \frac{1}{\kappa x^+} = \frac{u_\tau}{\kappa x}. \tag{3.25}$$

The wall friction velocity u_τ is simply obtained from the turbulent kinetic energy in the near wall cell through

$$u_\tau = C_\mu^{0.25} \sqrt{k}. \tag{3.26}$$

Bubble Growth Force

The last force missing in the bubble force balance equations at bubble departure (eq. 3.14 and eq. 3.15) is the bubble growth force F_{du}. Steiner et al. (2005) suggested to use an approach proposed by Zeng et al. (1993) to model the bubble growth force. This approach is based on the modeling of a growing hemisphere in an inviscid liquid. The authors came up with an expression for the growth force that depends on the expansion rate $\dot{r}$ and acceleration of the bubble radius $\ddot{r}$

$$F_{du} = -\rho_l \pi r^2 (10\dot{r}^2 + r\ddot{r}). \tag{3.27}$$

The empirical factor 10 was not in the original model, but has later been introduced by Zeng et al. (1993) to account for the presence of a wall. As the temporal derivative of

the bubble radius r indicate, it now has to be considered as a function of time during its growth period. A model for diffusion controlled bubble growth was presented by Zuber (1961). The temporal evolution of the bubble radius during its growth is expressed as a function of the Jakob number Ja, the thermal diffusivity of the liquid phase κ_l and the time t

$$r(t) = \frac{2b}{\sqrt{\pi}} Ja \sqrt{\kappa_l t}. \tag{3.28}$$

The empirical constant b has been tuned experimentally to a value of 0.21. The Jakob number describes the ratio of the sensible heat and the latent heat of evaporation

$$Ja = \frac{\rho_l c_{p,l}(T_w - T_{sat})}{\rho_v L}. \tag{3.29}$$

Because of the dependency of the temporal evolution of the bubble radius $r = r(t)$ on the Jakob number and so the wall temperature T_w, an iterative procedure is required to solve the force balance.

The first and second temporal derivative of the bubble radius (eq. 3.28) are also required by the model for the bubble growth force (eq. 3.27) and can be obtained as

$$\dot{r} = \frac{Ja}{\sqrt{\pi}} \frac{b\kappa_l}{\sqrt{\kappa_l t}} \tag{3.30}$$

and

$$\ddot{r} = -\frac{1}{2} \frac{b\kappa_l^2 Ja}{\sqrt{\pi}(\kappa_l t)^{\frac{3}{2}}}. \tag{3.31}$$

The two force balances eq. 3.14 and eq. 3.15 are solved for the departure radius r_{dep} and the departure inclination angle ϕ simultaneously. With eq. 3.28 solved for the time t and eq. 3.16 for the buoyancy force, eq. 3.17 for the drag force, eq. 3.18 for the shear lift force and finally eq. 3.27 for the growth force inserted in the force balance equations (eq. 3.14 and eq. 3.15), the following system of equations is obtained

$$
\begin{aligned}
\sum F_x &= 2/3 \frac{b^3 Ja^3 \sqrt{4} g(\rho_l - \rho_v)}{\sqrt{\pi}} \left(\frac{\pi r^2}{b^2 Ja^2}\right)^{3/2} \\
&+ 3\sqrt{\pi} \mu_l \, u_r \, bJa \sqrt{4} \sqrt{\frac{\pi r^2}{b^2 Ja^2}} \\
&\cdot \left(2/3 + \left(\left(3\frac{\sqrt{\pi}\sqrt{4}\mu_l}{\rho_l \, u_r \, bJa}\left(\sqrt{\frac{\pi r^2}{b^2 Ja^2}}\right)^{-1}\right)^n + 0.796^n\right)^{-n^{-1}}\right) \\
&\cdot \frac{\rho_l \, b^4 Ja^4 \alpha^2 \sin(\phi)}{\pi} \\
&= 0
\end{aligned}
\tag{3.32}
$$

$$\sum F_y = 1/2\, Cl\, \rho_l\, \pi\, r^2 u_r{}^2 - 36\frac{\rho_l\, b^4 Ja^4 \alpha^2 \cos(\phi)}{\pi} = 0 \tag{3.33}$$

Eq. 3.32 can now be solve for $sin(\phi)$ and eq. 3.33 for $cos(\phi)$. With the trigonometric identity

$$sin(\phi)^2 + cos(\phi)^2 - 1 = 0, \tag{3.34}$$

a bubble departure radius can be found for a given wall temperature T_w.

With the bubble departure radius r_{dep} obtained, the missing parameter is now the bubble lift-off radius r_{lift}. With the assumption of zero inclination at lift-off, the complete growth force F_{du} acts in the flow normal direction and is only encountered by the shear lift force F_{sl}. This results in the force balance in the y direction at bubble lift-off as

$$F_{y,lift} = 0 = F_{du} + F_{sl}. \tag{3.35}$$

With the inclination angle $\phi = 0$, eq. 3.35 can be solved directly for a given wall temperature T_w and the bubble lift off radius is finally obtained as

$$r_{lift} = \frac{6\sqrt{2}Ja^2b^2\kappa_l}{\sqrt{Cl}u_r\pi}. \tag{3.36}$$

The microscopic heat transfer coefficient h_{mic} (see eq. 3.10) can now be calculated with variables available in the near-wall cell of the computational domain, and a dependency of global flow properties like the Reynolds number is eliminated.

The macroscopic heat transfer coefficient h_{mac} is calculated with the well known Dittus Boelter equation (eq. 2.85) in the model of Steiner et al. (2005), which again is relying on the Reynolds number. In the model proposed in this study, the macroscopic part of the heat transfer coefficient is obtained from the turbulent thermal diffusivity κ_t computed in the near wall cell. The wall heat flux applied on the outside wall of the computational domain is expressed with the definition of the thermal conductivity λ of the fluid as

$$q = -\lambda\nabla T. \tag{3.37}$$

The wall heat flux q is proportional to the thermal conductivity multiplied with the negative temperature gradient. If the dimension of the heat flux is reduced to 1, eq. 3.37 becomes

$$q_y = -\lambda\frac{\partial T}{\partial y}. \tag{3.38}$$

In an Eulerian two-fluid approach as employed in this study, the grid size should be bigger than the interface details (see Niceno et al. (2008)). This means that the center of the first near-wall cell is not in the laminar sublayer and thus the influence of turbulence on the thermal conductivity has to be considered. The applied heat flux can now be expressed as

$$q_{y,eff} = -(\lambda + \lambda_t)\frac{\partial T}{\partial y}. \tag{3.39}$$

The one-dimensional temperature gradient $\frac{\partial T}{\partial y}$ can be linearized with a differential quotient as

$$\frac{\partial T}{\partial y} = \frac{T_w - T_P}{\Delta y}. \tag{3.40}$$

The positions of the wall temperature T_w and the cell-center temperature T_P in the computational grid, as well as the distance from the near-wall cell center to the wall Δy are depicted in figure 3.4.
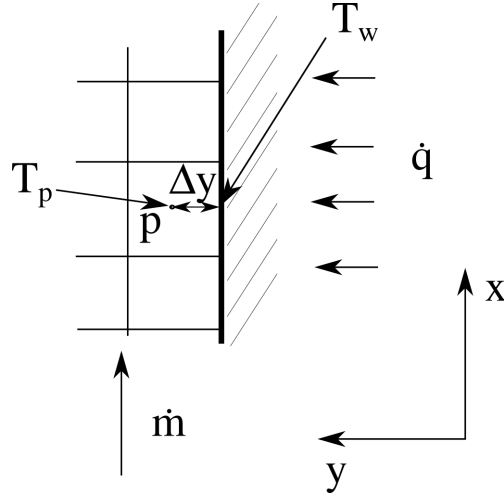
Figure 3.4: Distance from cell center to the heated wall. Graphic from Sonntag and Cheng (2016).

The turbulent thermal conductivity λ_t is obtained from the formulation of the logarithmic temperature law of the wall in terms of the dimensionless temperature T^+

$$T^+ = \frac{(T_w - T_p)\rho c_p k^{\frac{1}{2}}}{q} = \begin{cases} y^+ Pr + \frac{1}{2}\rho Pr \frac{u_\tau}{q} u^2 & \text{for } y^+ < y_{therm} \\ Pr_t[\frac{1}{\kappa}ln(Ey^+) + P] + \frac{1}{2}\rho\frac{u_\tau}{q}[Pr_t u^2 + (Pr - Pr_t)u_c^2] & \text{for } y^+ > y_{therm}. \end{cases}$$

$$(3.41)$$

E is an empirical constant with a value of 9.793. The dimensionless temperature T^+ is calculated differently depending on whether the dimensionless wall distance y^+ is smaller or greater than the dimensionless temperature sub-layer y_{therm}. y_{therm} is defined as the dimensionless distance from the wall at the intersection between the linear law and the logarithmic law of the wall and u_c is the mean velocity magnitude at $y^+ = y_{therm}$.

A common choice for the model of the sublayer resistance function P from eq. 3.41 is the model proposed by Jayatilleke (see Malin (1987) as the original paper by Jayatilleke is unfortunately not available to the author)

$$P = 9.24(\gamma^{\frac{3}{4}} - 1)[1 + 0.28exp(-0.007\gamma)].$$

$$(3.42)$$

γ is the ratio of Prandtl number to the turbulent Prandtl number. With the sublayer resistance function P (see. eq 3.42), the dimensionless temperature T^+ and so the denominator of eq. 3.40 can be calculated. For a given heat flux, the effective thermal conductivity due to convection

$$\lambda_{eff,conv} = \lambda + \lambda_t$$

$$(3.43)$$

is then obtained from eq. 3.39. The macroscopic heat transfer coefficient h_{mac} can then be calculated from the linearized form of the heat conduction equation with

$$h_{mac} = \frac{\lambda_{eff,conv}}{\Delta y}.$$

$$(3.44)$$

This closes the model for the heat transfer coefficient under subcooled nucleate flow boiling. This model only relies on properties found or calculated in the near-wall cell of the

computational domain, which makes it suitable for the application in 3D-CFD computer codes. The validation of the model will be shown in chapter 5.

4. Efficient coupling of STH and CFD

The coupling methodology and implementation presented here can be seen as a continuation of the work by Lerchl (2007). Lerchl (2007) extended the STH code ATHLET in a way that makes it possible to stop the calculation at certain temporal positions in the program flow, based on keywords, and resume it afterwards. This enables an ATHLET run to be halted, transfer variables to or from ATHLET to or from another program, let the other program do some computation and return back to the ATHLET run. An ATHLET run is divided into the following steps:

1. Initialization and parsing of input data

2. Steady state calculation

3. Initialization of coupling and start of transient calculation

4. Temporal progression of transient run

5. End of run

The majority of computational time will be spent on step 4, the transient run. In a coupled calculation, the data will have to be exchanged at least once per time step. For a assumed simulation of just 1000 s physical time and a typical time step for a multiphase RANS simulation of 0.0005 s, this will be 2e6 operations just for the exchange of information between the two coupled codes. This shows that if the data exchanges between the two codes are done in an efficient way, a lot of computational resources can be saved.

The most simple way to couple two computer codes is to execute them as separate kernel processes and exchange the information between the processes with file I/O operations. This means, one program writes the information it wants to transfer to the other onto the hard disk and the other program reads this information again from the hard disk. Kenway (2013) gives a comparison between file I/O and in ram information transfer and comes to the conclusion that file based data exchange is not a viable solution for the coupling of high performance numerical codes. Running the two codes as separate processes that have to be restarted after every time step is also not an efficient solution, as the creation and destruction of kernel threads is an expensive operation.

This leads to the conclusion that the most efficient way to coupled two numerical codes is to execute them in the same memory space for fast information exchange and to either execute them in the same kernel thread or keep the kernel threads alive during the simulation to avoid the cost of creation and destruction of kernel threads.
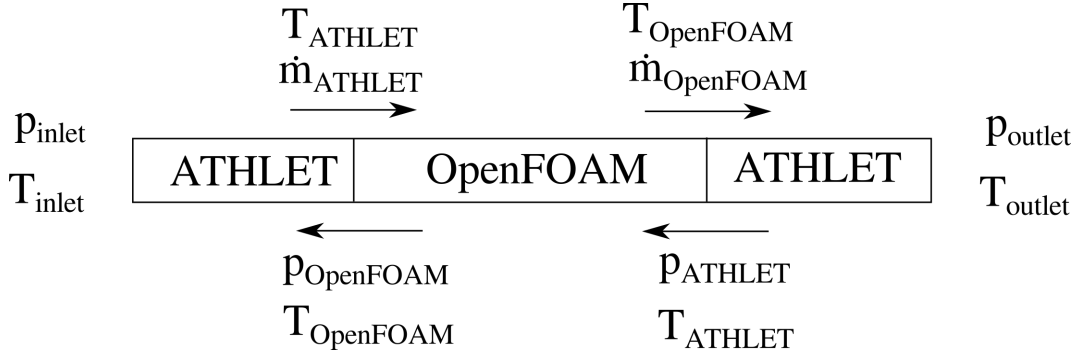
Figure 4.1: Position of coupling variables for a simple pipe (single phase).

4.1 Coupling Methodology

The coupling methodology presented here can be considered as *explicit coupling with domain decomposition.* Domain decomposition means that the whole computational domain is split up into parts for each code and each code simulates just that part. This is in contrast to domain overlapping approaches, where the system code computes the whole domain and the CFD code simulates a part of it as well (see Jeltsov et al. (2013)). Explicit means that the simulation is progressed in time only with information available at the current time step.

In figure 4.1, the exchange of variables for a coupled open pipe simulation is depicted. Here an ATHLET pipe is split up into tree parts and the middle part is replaced with a 3D-CFD mesh. Boundary conditions, from the user input side, are only set on the outer parts of the ATHLET domain. The boundary conditions for the 3D-CFD mesh are obtained at every time step from ATHLET, through the newly developed coupling interface. In this example, the pressure and temperature at the inlet and outlet of the ATHLET domain are given by the user. At the first coupling interface between ATHLET and OpenFOAM, ATHLET supplies the mass flow rate and the temperature to OpenFOAM, while OpenFOAM returns pressure and temperature to ATHLET. At the second coupling interface, OpenFOAM hands the mass flow rate and the temperature over to ATHLET and ATHLET gives OpenFOAM the pressure and temperature as the boundary conditions.

As OpenFOAM is a 3D-CFD library and ATHLET a 1D-STH code, the transferred quantities have to be averaged at the interfaces, when transferred from 3D to 1D. To transfer the mass flow from OpenFOAM to ATHLET, all mass flows through the cell-faces at the coupling interfaces are summed up, to gain the total mass flow through the coupling interface. This total mass flow is handed over to ATHLET as the boundary condition. When the information of mass flow is transferred from ATHLET to OpenFOAM, a uniform velocity is set at the coupling interface on the OpenFOAM side

$$u_{liquid,uniform,OpenFOAM} = \frac{G_{liquid,ATHLET} * GeomSclaingFactor}{\rho_{liquid} * A_{interface}}. \tag{4.1}$$

A geometric scaling factor is used, to allow 3D simulations where only a part of the full geometry is used. For example, a pipe could be split along its axial direction to reduce computational time of the CFD side. $A_{interface}$ is the sum of all cell-face areas at the coupling interface on the OpenFOAM side. The gas phase velocity is calculated in an analogous way to eq. 4.1. To transfer pressure, liquid and vapor temperatures, void
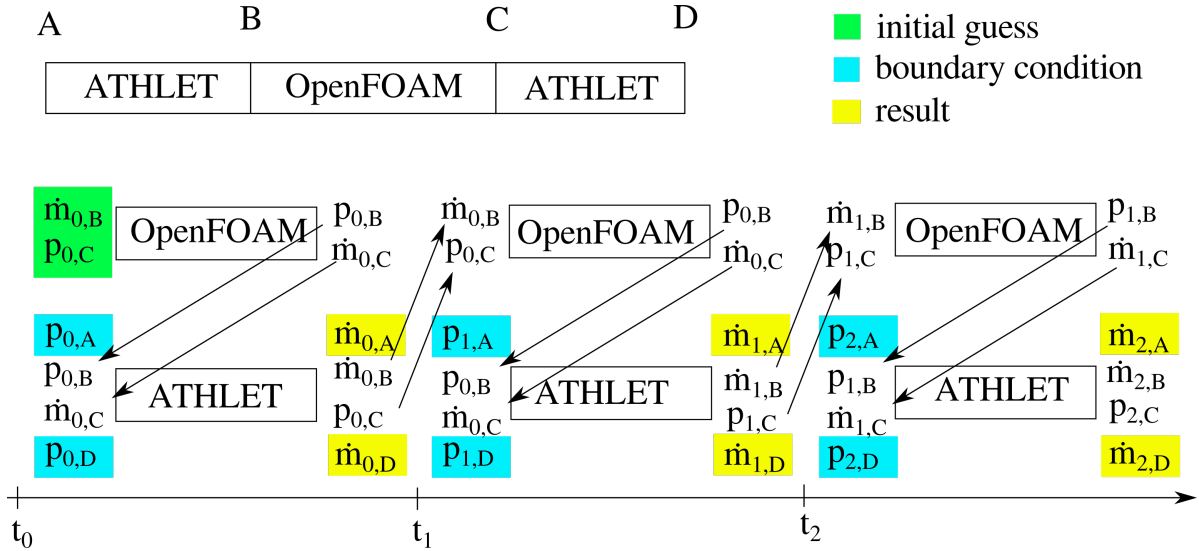
Figure 4.2: Evolution of coupling variables over time (single phase).

fraction and quality from 3D to 1D, a surface weighted averaged value is used

$$\phi_{averaged} = \frac{\sum(\phi_{face,i} * A_{face,i})}{A_{interface}}. \tag{4.2}$$

In the reverse direction, from ATHLET to OpenFOAM, the ATHLET values are applied as a uniform boundary field on the OpenFOAM side.

In the OpenFoam simulation, additional inlet boundary conditions for the turbulence model have to be applied, that are not available from the ATHLET side. These have to be estimated beforehand. A common choice is to assume a turbulent intensity I_t of 5 %. This is also done in all CFD simulations in this study.

The temporal evolution of this exchange of information between the codes is shown in figure 4.2. The configuration of the coupled system is the same as in the example above, but for the sake of simplicity only an isothermal system is shown. The inlet and outlet pressure will be again the user input boundary condition (shown in blue) and the mass flow rate will be the result (yellow) of the simulation. At the beginning of every coupled simulation, an initial guess (green) has to be made for the inlet mass flow rate and outlet pressure for the CFD domain. This guess is trivial if the transient simulation is initialized with zero mass flow rate as the pressure will be the same as the hydrostatic pressure which can be calculated analytically beforehand.

Parallelization of CFD codes can be considered as standard procedure today to reduce the computational time for large simulations. A popular way to parallelization is to decompose the computational domain into the same number of smaller domains, as CPU cores are available for the simulation. The exchange at the boundaries between these sub-domains is often realized with the message passing interface (MPI, see Forum (1994)). This is also the case for OpenFOAM. Parallelization of system codes, especially ATHLET, is of less importance as the run-times of these codes are very short in comparison to the run-time of CFD codes. The way how a parallel computation is achieved, in the proposed coupling approach, is illustrated in figure 4.3. ATHLET is running on one CPU-core and OpenFOAM on as many CPU-cores as needed. Because CFD domains get split up into smaller sub-domains, the coupling interfaces might also get split up. In order to exchange the coupling variables at the split up interfaces between the two codes, the
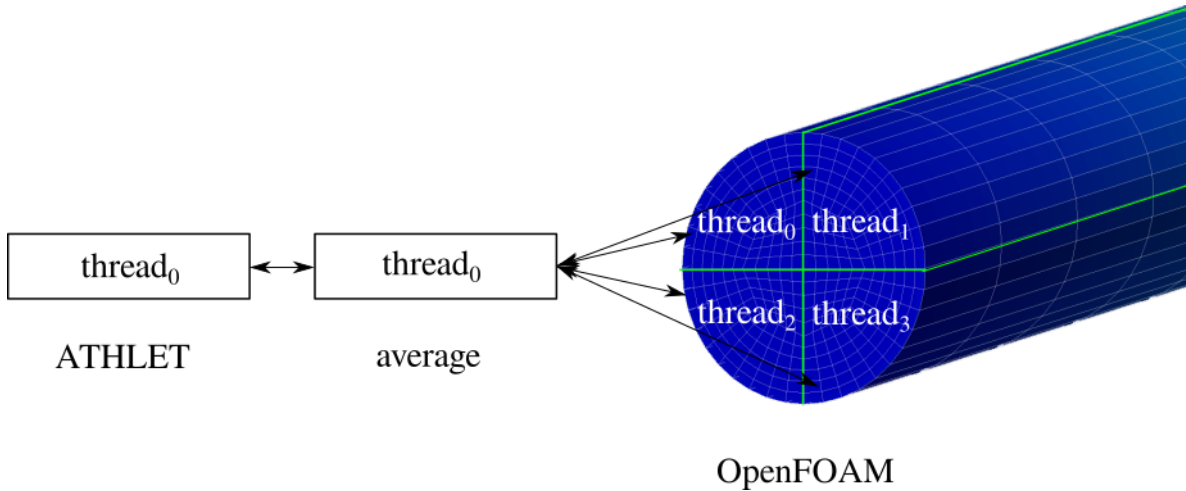
Figure 4.3: Coupled parallel dataflow.

information from all CFD sub-domains has to be either retrieved and averaged before it can be transfered from OpenFOAM to ATHLET or it has to be sent to all sub-domains in case the information is transfered from ATHLET to OpenFOAM. This process has been implemented with the MPI in the here proposed coupling approach.

4.2 Coupling Implementation

Different physical processes are grouped into separate solver applications, while sharing a set of common libraries in OpenFOAM. There is one solver application for incompressible, isothermal, non-turbulent flow for example. Or another one for isothermal multiphase flow. This is done to reduce the complexity of the applications. But coupling between STH and CFD is interesting for many physical processes (single and multiphase flow for example). If the coupling would be integrated into the solver application itself, it would not be universal to other solvers and it would have to be rewritten for every solver application of interest. Another problem would be that solver applications get frequent updates from the core development of OpenFOAM. In order to make use of the updates, the new code would always have to be integrated into the coupled solver. For these reasons, the coupling interface has been implemented in an OpenFOAM specific framework called functionObjects (see figure 4.4). These functionObjects are libraries that get linked during runtime to the main application. A certain set of functions in this class is executed at specific positions in the evolution of the program run. The same functionObject can be used by many different solver applications. The newly developed coupling interface detects if the applied solver is a single phase or a multiphase solver, and handles the exchange of variables at the coupling interfaces accordingly.

In order to use ATHLET as a functionObject, the FORTRAN routines have to be exposed to the OpenFOAM C++ code via bindings. A C function name has to be provided to every FORTRAN subroutine that is to be called directly from the C++ code (see listing 4.1). The following code listings are shortened to make them more comprehensible.

```
1  subroutine acoupleini() bind(C, name="acoupleini")
2  use iso_c_binding
```

Listing 4.1: Exposition of a FORTRAN routine to C.

The data type of the variables also has to be given for both languages. In listing 4.2, this procedure is shown for *real* data types in FORTRAN to be used as type *double* in C++.
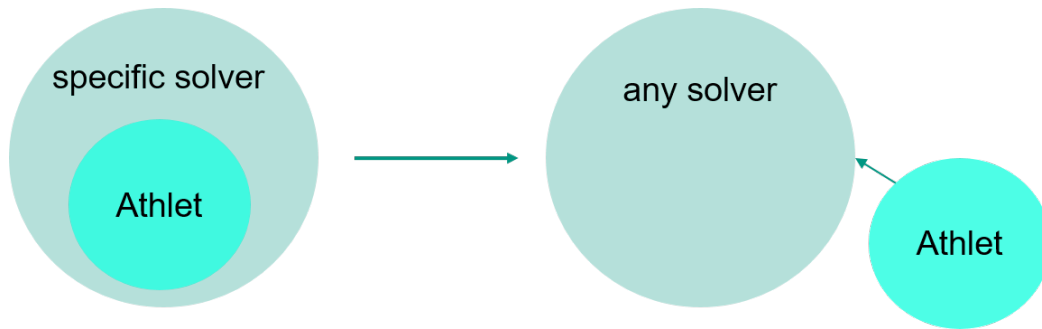
Figure 4.4: Universal implementation of the coupling interface.

```
1  real(c_double), value :: TIFOAM, TIFOAMO, PFOAM,XFOAM, XFOAMO,
2    & TLFOAM, TVFOAM, GLFOAMO, GVFOAMO, GHLFOAMO, GHVFOAMO
```

Listing 4.2: Exposition of FORTAN data types to C.

With the FORTRAN subroutine names exported and the exchange variable data types declared, the FORTRAN subroutines have to be declared in the C++ class implementation as external C functions (see listing 4.3).

```
1  extern ”C”
2  {
3    void athlet();
4    void acoupleini(double PFOAMINITL, double PFOAMINITR);
5    double _massflow_athlet;
6  }
```

Listing 4.3: Declaration of FORTRAN functions and variables in C++ as external C code.

Variables that are transfered from FORTRAN code to C++ also have to be declared in the *extern* statement. To make them available to the C++ library, the variables are stored in a FORTRAN module and are provided again with C variable names (see listing 4.4).

```
1  MODULE ACOUPLE
2    USE ISO_C_BINDING
3    real(c_double), bind(C, name=”_massflow_athlet”) :: MATHL
4    real(c_double), bind(C, name=”_pressure_athlet”) :: PATHL
5  END MODULE
```

Listing 4.4: Declaration of FORTRAN variables with C names in a FORTRAN module.

The ATHLET library and OpenFOAM have to be compiled with the same compiler family in order to make the binding work. ATHLET used to be compiled with an INTEL compiler while OpenFOAM is compiled with the GNU compiler as standard. The compilation process of ATHLET was organized with the help of plain make files originally. This is unpractical for a code base that consists of 838 different files. For this reason, ATHLET was modified to be compiled with the GNU Compiler Collection, and the compilation process was simplified with the help of the build system *scons* (see Knight (2005)).

Post-processing of Coupled Simulations

For post-processing of the coupled simulations, a conversion tool for the results from ATHLET to a *visualization tool kit* (VTK) (see Schroeder et al. (1996)) conform data format has been developed in this study. ATHLET results are usually visualized with a proprietary tool provided by GRS. This tool is very limited and is not able to visualize data in any other format than the special ATHLET result format. In order to gain an understanding of the interaction between the domains simulated by the two code systems, it

Inlet	ATHLET Pipe1	OpenFOAM	ATHLET Pipe2	Outlet

Figure 4.5: Configuration of coupling verification case no 1. Open system.

is of great importance to be able to visualize both results in a common place. OpenFOAM results can be exported to a variety of post processing formats with VTK being the most common one. An example for a visualization of a coupled simulation is given in figure 4.10.

4.3 Coupling Verification

Verification of the coupling interface is presented in the following according to the definition of verification by Mahaffy et al. (2007). It will be checked if simulations with the implemented coupling interface will produce expected results. These expected results are obtained from ATHLET standalone simulations of simple geometries and well defined boundary conditions. A total of four test cases will be recalculated for the verification and explained in detail (see table 4.1 for an overview of the verification test cases).

Table 4.1: Verification matrix for coupling interface ATHLET - OpenFOAM.

Case No	flow type	isothermal/heated	system type
1	single-phase	isothermal	open system
2	single-phase	heated	natural circulation loop
3	two-phase	isothermal	forced circulation loop
4	two-phase	heated	mixed circulation loop

4.3.1 Case No 1. System with Inlet and Outlet

The first verification test case is a horizontal, isothermal three pipe configuration with one inlet and one outlet. An overview of the system configuration is shown in figure 4.5. The two outer pipes (labeled with *ATHLET Pipe1* and *ATHLET Pipe2*), with a length of 7.5m will be simulated with ATHLET and the inner pipe, with a length of 2.5 m will be simulated with OpenFOAM. The diameter of all pipes is 0.05 m. The result of the coupled simulation is compared with a simulation, where all pipes are simulated by ATHLET. The main goal of this verification case is to test the if the coupling interface is capable to handle flow reversal.

The OpenFOAM mesh has the geometry of a 3D pipe. The mesh is block-structured with an O-grid in the center. The total cell size for the mesh is 6800. This leads to a y^+ of 150 at the highest velocity. Standard wall functions along with the $k - \omega$ SST turbulence model are applied.

The ATHLET pipes are discretized with 10 control volumina. The sampling in the ATHLET pipes is taken in the third control volume of each pipe.

Description of the Boundary Conditions

The boundary conditions are applied on the outer endings of the ATHLET pipes. The left ending will be called inlet and the right ending will be called outlet. The transient simulation is initialized with zero mass flow and a uniform temperature and pressure distribution. The pressure applied at both boundaries is 2.0 bar and the specific enthalpy

Table 4.2: Transient boundary conditions for Inlet-Outlet simulation.

Time [s]	Inlet Specific Enthalpy $[\frac{J}{kg}]$	Outlet Pressure [Pa]
0	$81.75e3$	$2.0e5$
5	$81.75e3$	$2.0e5$
6	$81.75e3$	$1.75e5$
15	$81.75e3$	linear interpolation
16	$125.0e3$	linear interpolation
30	$125.0e3$	$2.25e5$

is specified to be $81.75e3$ $\frac{J}{kg}$. The system is kept in this state for 5 s. From second 5 to 6 the pressure at the outlet is reduced to 1.75 bar and then gradually increased to 2.25 bar until 30 s. The inlet specific enthalpy is increased to $125.0e3$ $\frac{J}{kg}$ from second 15 to 16. The specific enthalpy at the outlet is always kept at its initial value of $81.75e3$ $\frac{J}{kg}$. An overview of the transient boundary conditions is given in table 4.2.

Interpretation of simulation Results

The results of the first verification case are presented in figure 4.6. Here the mass flow, pressure, and temperature at two locations (third control volume of each outer ATHLET pipe) of a coupled simulation are compared with an ATHLET standalone simulation. The results are expected to be very similar, as ATHLET as well as OpenFOAM have shown to be able to recalculate simple pipe geometries. So the introduction of the coupling interface should cause no change in the results. In the first period of the simulation from 0 s to 5 s, no mass flow is expected to be seen, as the inlet and outlet pressure are the same. As a result, the temperatures are also expected to be uniform in this time period. With the decrease in outlet pressure after 5 s, a mass flow from left to right is expected to occur. As the specific inlet enthalpy is unchanged, no difference in the temperature is expected. The increase in mass flow can be seen in figures 4.6 (a) and 4.6 (b) and the steady temperature in figures 4.6 (e) and 4.6 (f). Not only the temporal evolution of the mass flow, but also the absolute values can been regarded as identical. This shows that no pressure is added or lost through the two coupling interfaces that have been introduced here.

As the pressure at the outlet is then increased above the value of the inlet pressure, a flow reversal is expected. This can also be observed in the simulation results. The pressure difference between inlet and outlet is again 0.25 bar in the last part of the simulation and the same absolute value of the mass flow established as before, but in the other direction, now from right to left.

The enthalpy transfer through the coupling interface is verified with the increase of specific inlet enthalpy after 15 s at the inlet boundary. As long as the mass flow in the system is positive, this increase of specific enthalpy should also be seen in the sampling locations after some time. If the mass flow is reversed, the temperature should revert to its initial temperature as the specific enthalpy at the outlet is unchanged throughout the simulation. Both expected events can be observed in figure 4.6 (e) and (f).

In figure 4.7, radial profiles of the velocity component in axial direction and the temperature are shown for the time steps $t = 10s$, $t = 20s$, $t = 30s$ and $t = 40s$. The velocity profiles show typical turbulent velocity profiles. The reversal of the flow direction is also clearly visible. The temperature profiles are flat, as expected for an adiabatic pipe flow.
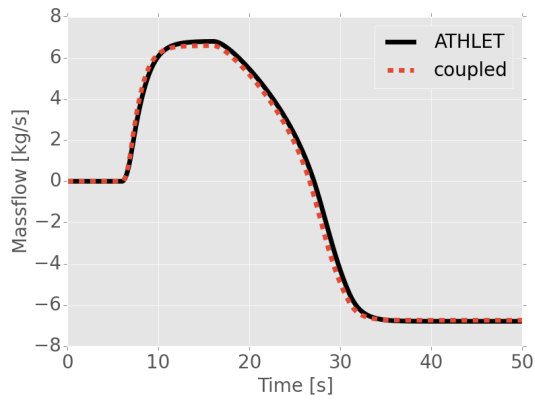
(a) Massflow in ATHLET Pipe1.
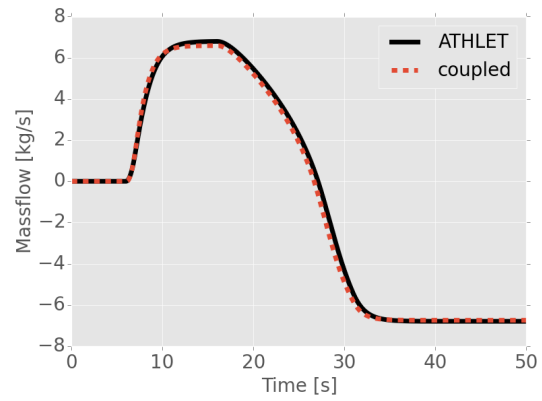
(b) Massflow in ATHLET Pipe2.
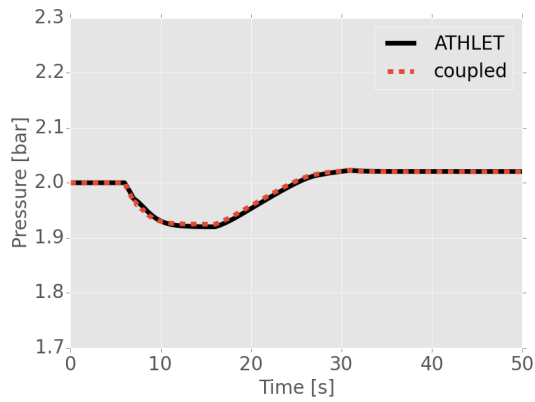
(c) Pressure in ATHLET Pipe1.
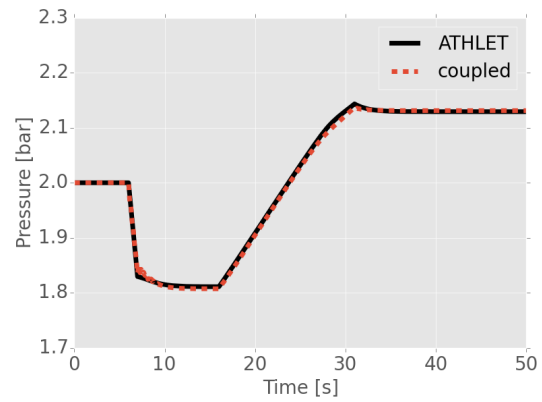
(d) Pressure in ATHLET Pipe2.
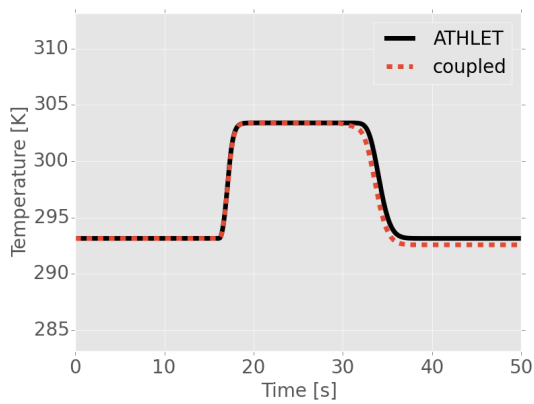
(e) Fluid temperature in ATHLET Pipe1.
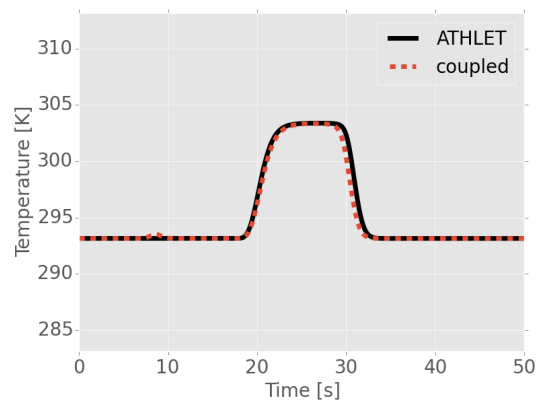
(f) Fluid temperature in ATHLET Pipe2.

Figure 4.6: Comparison of coupled OpenFOAM-ATHLET simulation with ATHLET standalone of a system with one inlet and one outlet. Case No. 1.

(a) Velocity profiles in the middle of the Open-FOAM pipe.

(b) Temperature profiles in the middle of the OpenFOAM pipe.
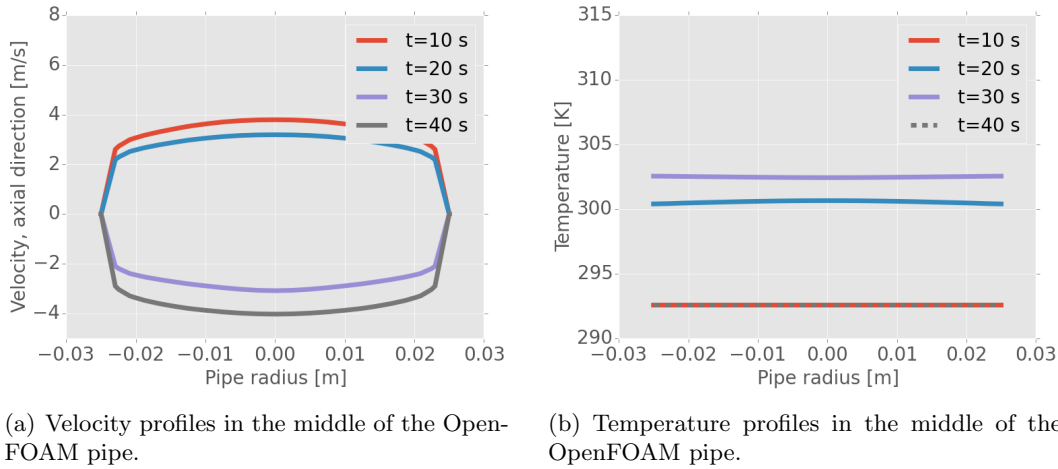
Figure 4.7: Radial velocity and temperature profiles over time, sampled in the middle of the pipe. Case No. 1.

4.3.2 Case No 2. Single Phase Natural Circulation Loop

The second verification example is the simulation of a natural circulation loop. The loop has a total height of 5 m and the length of the heated section is 2.5 m, starting from an elevation of 0.25 m above the lowest point of the loop (0 m). The complete configuration of the loop is shown in figure 4.8. All parts have a cylindrical shape with a diameter of 0.05 m. The cooled pipe is located at a higher location than the heated pipe and also has a length of 2.5 m. The pipe with a heat source will be simulated by OpenFOAM in the coupled version. The top of the loop is connected to an open end, where a fixed pressure of 2 bar is applied. The bottom sample is taken in the last control volume of the pipe, which is connected to the left side of the OpenFOAM pipe at an elevation of 0.24 m. The top sample is taken from the first control volume of the pipe connected at the right side of the OpenFOAM pipe at an elevation of 2.75 m. In the ATHLET standalone version, all pipes will be simulated by ATHLET again. The main purpose of this simulation is to test if a stable mass flow can be achieved in a closed coupled loop.

The OpenFOAM mesh is a 5 degree wedge with a total of 5000 cells. This results in a y^+ value of 3. Standard wall functions are used with a $k - \omega$ SST turbulence model.

Description of the Boundary Conditions

The only boundary conditions for this simulation are a constant temperature at the outer wall of the heated pipe of 313.15 K and a constant temperature of 278.15 K at the outer wall of the cooled pipe. All other pipes are treated as adiabatic. The working fluid is water and an initial pressure of 2 bar is assumed. The initial temperature in the loop is set to 293.15 K.

Interpretation of simulation Results

A positive mass flow in clockwise direction is assumed, caused by the density difference of the heated water at the low elevation and the cooled water at the higher elevation. A comparison of the temperature, mass flow and pressure evolution over time of the standalone and the coupled simulation is given in figure 4.9. In both cases, a stable mass flow is established after an initialization phase of about 300 to 400 s. A stable pressure distribution can be observed in both cases (see figures 4.9 (c) and 4.9 (d)). The coupled simulation shows a slightly higher mass flow than the standalone simulation. An
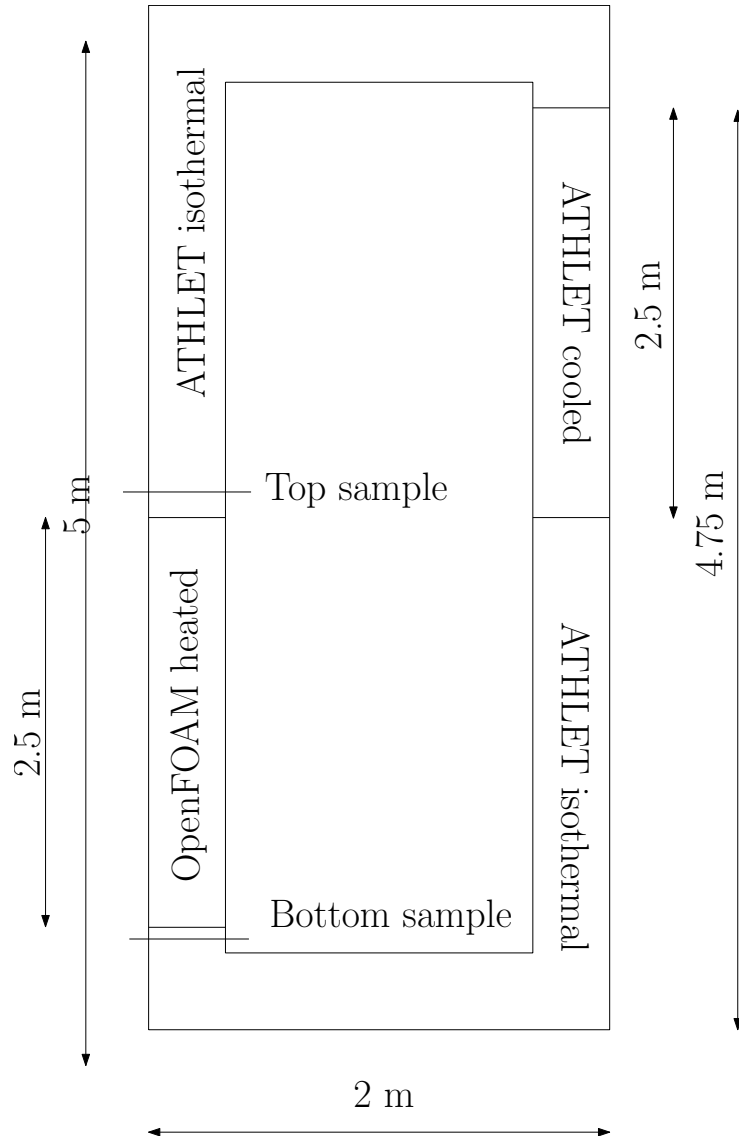
Figure 4.8: Configuration of coupling verification case no 2. Natural circulation loop.

explanation for this can be found in the temperature evolution sampled right after the heated pipe (figure 4.9 (e)). A higher temperature can be seen in the case of the coupled simulation, which caused a higher density difference and leads to a higher mass flow. The temperature difference itself can be explained by the fact that the heat transfer processes are treated differently in the two compared simulations. In the ATHLET standalone simulation, the liquid fluid temperature is calculated with a heat transfer correlation (see 2.85) while in case of the OpenFOAM simulation, wall temperature is applied at the wall bounded cells and from there on transported by the solution of the Navier-Stokes equations and the turbulence model. This does not explain why the temperature is higher in the case of the coupled simulation, but shows that a difference in temperature can occur. In figure 4.10 the result of coupled simulation at time 600 s is presented. On the left, the pressure distribution of the coupled system can be seen and on the right the temperature distribution. This combined visualization of coupled results is possible with the newly developed post processing tool for ATHLET results. Important here is the continuous pressure and temperature distribution throughout the different simulation domains.

4.3.3 Case No 3. Two-Phase Isothermal Closed Loop

The third verification example for the ATHLET - OpenFOAM coupling is the simulation of an isothermal closed loop. All geometries are of cylindrical shape, with a diameter of 0.05 m. The total height of the loop is 3 m. The bottom sample is placed at an elevation of 0.05 m, and the top sample at an elevation of 2.95 m. The highest part of the loop is connected to an open pipe end where a pressure of 2 bar is applied. The configuration of the loop is shown in figure 4.11. The driving pressure in this simulation is provided by a pump model, with a constant pressure of 0.02 bar, by ATHLET. The void fraction is kept at zero throughout the simulation. The main difference in this example is that the two-fluid solver is now employed on the OpenFOAM side. This can be done without recompiling the solver as the coupling interface in packaged into the functionObject that gets linked to the solver at runtime. The purpose of this test is to verify that the coupling interface correctly detects that the OpenFOAM solver is now a two-fluid solver and not single phase solver as in the previous examples and adapts to this change accordingly.

The OpenFOAM mesh is a 5 degree wedge geometry with a total cell number of 5000 cells.

Description of the Boundary Conditions

No heat is added or removed in this simulation. The initial fluid temperature is set to 373.15 K and a pressure of 2 bar is set at the highest point of the loop. The initial mass flow rate is set to 0 $\frac{kg}{s}$. The driving pressure for the fluid circulation is supplied by a pump model with a fixed pressure difference of 0.02 bar throughout the simulation.

Interpretation of Simulation Results

Results for verification case number three are presented in figure 4.12. The mass flow starts to evolve from its initial value of 0 $\frac{kg}{s}$ to a constant value of 2.1 $\frac{kg}{s}$ due to the pressure difference created by the pump. This development of the mass flow rate can be observed in both, the coupled and the standalone simulation. The pressure is constant throughout the simulation in both cases. Also for the temperature as well as for the void fraction, no change is occurring as expected.
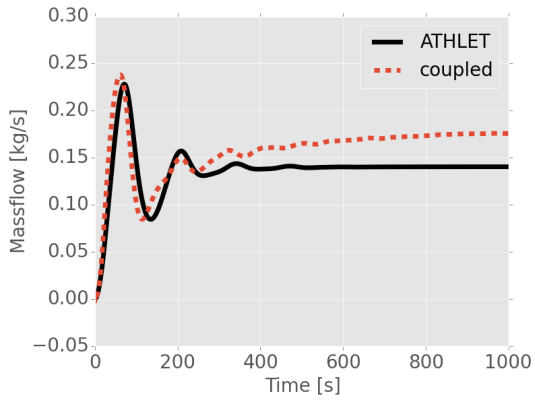
(a) Massflow at the bottom sample.
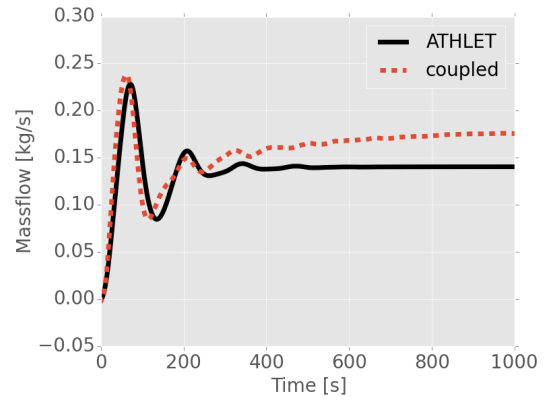
(b) Massflow at the top sample.
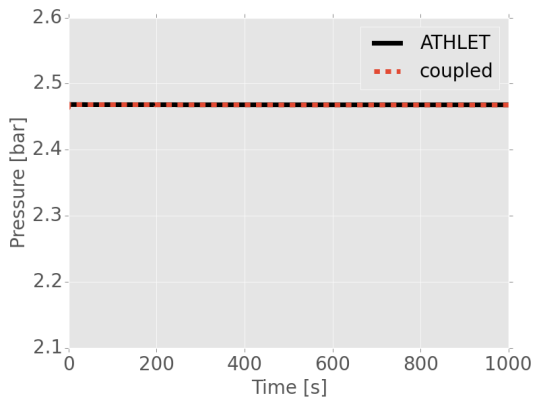
(c) Pressure at the bottom sample.
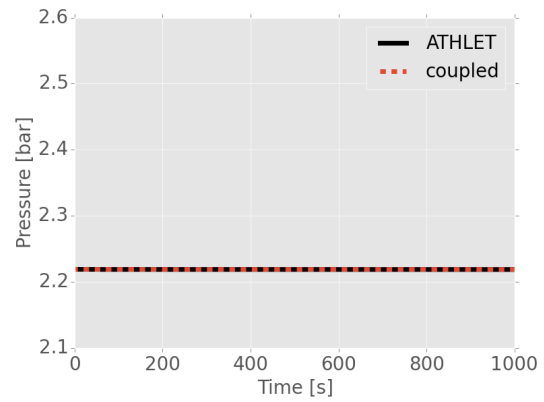
(d) Pressure at the top sample.
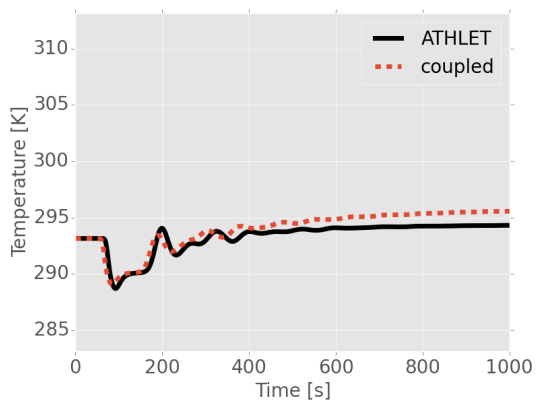
(e) Fluid temperature at the bottom sample.
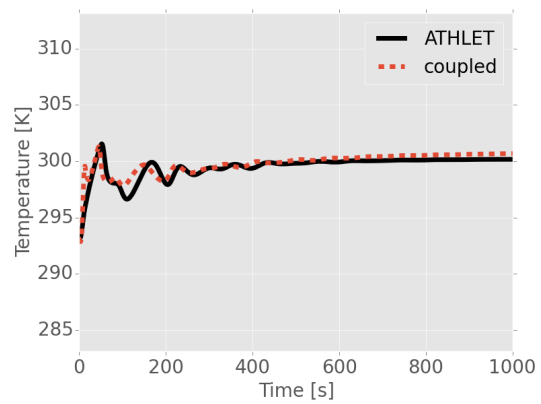
(f) Fluid temperature at the top sample.

Figure 4.9: Comparison of coupled OpenFOAM-ATHLET simulation with ATHLET standalone in a natural circulation loop. Case No. 2.

(a) Pressure distribution in the coupled natural circulation loop.

(b) Temperature distribution in the coupled natural circulation loop.
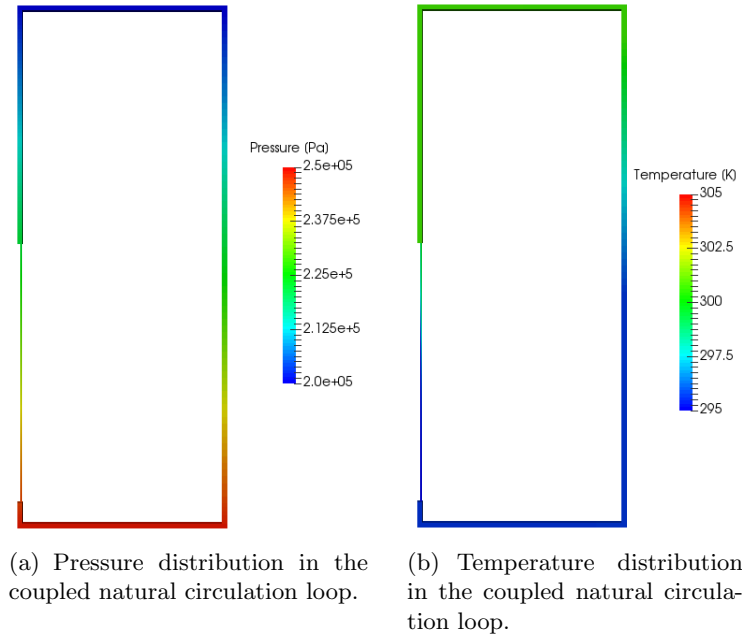
Figure 4.10: Pressure and temperature distribution in a natural circulation loop (3D View) calculated with the coupled ATHLET and OpenFOAM system.

4.3.4 Case No 4. Two-Phase closed Loop with Heat Transfer and Phase Change

The purpose of the last verification simulations is to test, if the properties of the gas phase are transported through the coupling interface correctly. Another outcome of this test is the demonstration of stability of the coupled system during two-phase flow conditions. All ATHLET fluid objects have a cylindrical shape with a diameter of 0.05m. The height of the loop is 3 m and the top is connected to an open pipe end, where a constant pressure of 2 bar is applied. A 2.5 m long section is replaced with an OpenFOAM part. The bottom sample is placed in the ATHLET pipe connected to the left end of the OpenFOAM pipe at an elevation of 0.23 m. The top sample is placed in the ATHLET pipe connected at the right end of the OpenFOAM pipe in its second control volume at an elevation of 2.77 m. The configuration of the test loop is shown in figure 4.13.

The OpenFOAM mesh is again the same 5 degree wedge geometry, as in the two cases before, with 5000 cells.

Description of the boundary conditions

A constant driving pressure of 0.02 bar is supplied by an ATHLET pump model. The fluid is initialized with a temperature of 373.15 K. The mass flow rate at the beginning is 0 $\frac{kg}{s}$. A heat source is introduced through an ATHLET pipe object with a wall temperature increasing linearly from 373.15 K to 428.15 K from second 1 to 10 of the simulation. The heat source is placed at the lowest position of the loop with a heating length of 0.25 m. At the top of the loop, a heat sink in installed. This heat sink is also a pipe object with a constant wall temperature of 373.15 K. All other pipes are treated as adiabatic. The OpenFOAM section is placed right after the heated part with a length of 2.5 m. An overview of the boundary conditions is given in table 4.3.
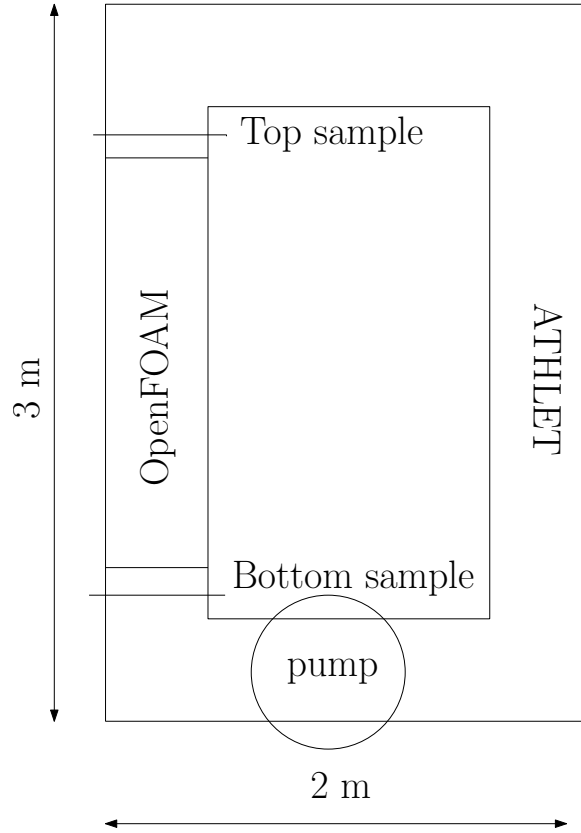
Figure 4.11: Configuration of coupling verification case no 3. Two-Phase Isothermal Closed Loop.

Table 4.3: Transient boundary conditions for two-phase closed loop with heat transfer and phase change.

| Parameter	Simulation time [s]	Value
pump pressure difference	0 - end	0.02 bar
temperature hot wall	1 - 10	linear from 373.15 K to 428.15 K
temperature hot wall	10 - end	428.15 K
temperature cold wall	0 - end	373.15 K

Interpretation of simulation Results

The mass flow starts again at 0.0 $\frac{kg}{s}$ and reaches a steady state of 2 $\frac{kg}{s}$ in both cases. The absolute value of the coupled and the standalone case are close but not the same. The mass flow rate in the standalone simulation is around 0.2 $\frac{kg}{s}$ higher than in the coupled simulation. The mass flow before and after the OpenFOAM section (see figures 4.14 (a) and 4.14 (b)) are the same. This leads to the conclusion that the pressure drop simulated by OpenFOAM is bigger than that simulated by ATHLET. The evolution of the pressure before and after the OpenFOAM pipe is shown in figures 4.14 (c) and 4.14 (d). The pressure can be considered as stable with slight oscillations that have not been observed in the other verification cases before. The temperature on the other hand is very stable and the difference between coupled and standalone simulation is small (see figures 4.14 (e) and 4.14 (f)). The most interesting solution variable in this test case is the void fraction shown in figure 4.14 (g) and 4.14 (h). The bulk liquid temperature is below the saturation temperature of 393.36 K throughout the simulation. It can be expected that after the vapor generation in the heated section, condensation will take place and reduce
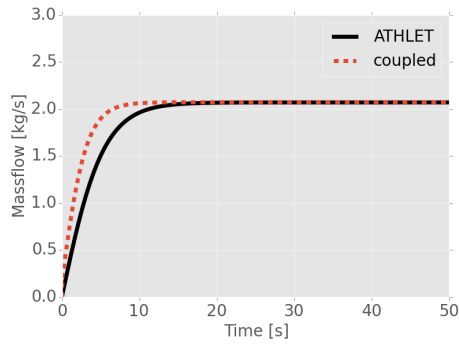
(a) Massflow at the bottom sample.
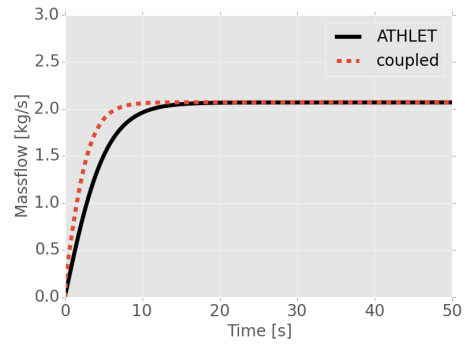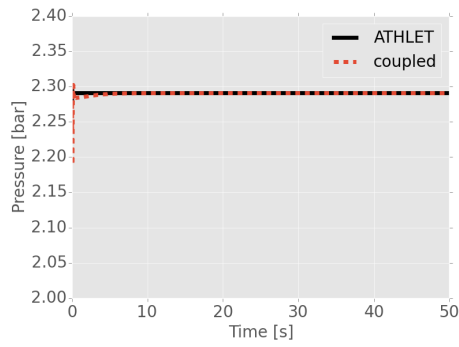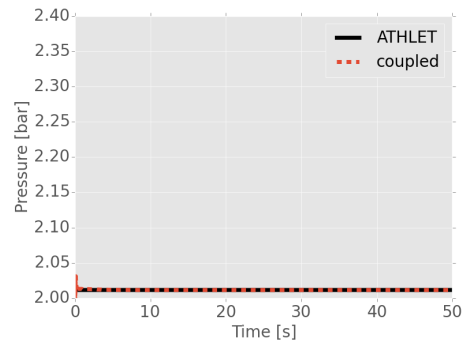
(b) Massflow at the top sample.

(c) Pressure at the bottom sample.

(d) Pressure at the top sample.
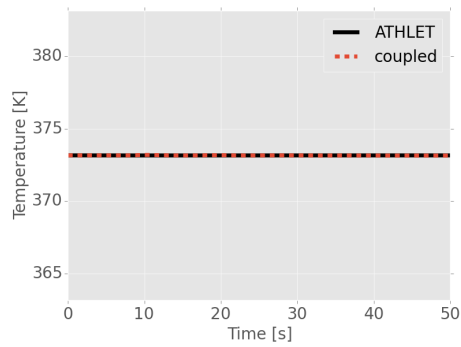
(e) Liquid temperature at the bottom sample.
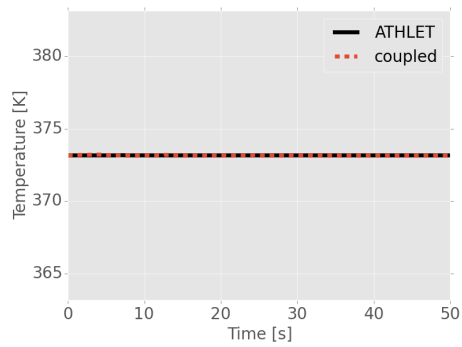
(f) Liquid temperature at the top sample.
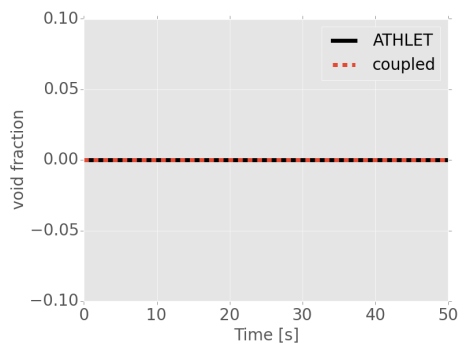
(g) Void fraction at the bottom sample.
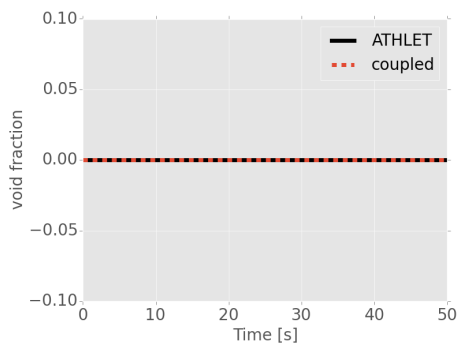
(h) Void fraction at the top sample.

Figure 4.12: Comparison of coupled two phase OpenFOAM-ATHLET simulation with ATHLET standalone in a isothermal loop. Driving pressure head is obtained from a pump. Case No. 3.
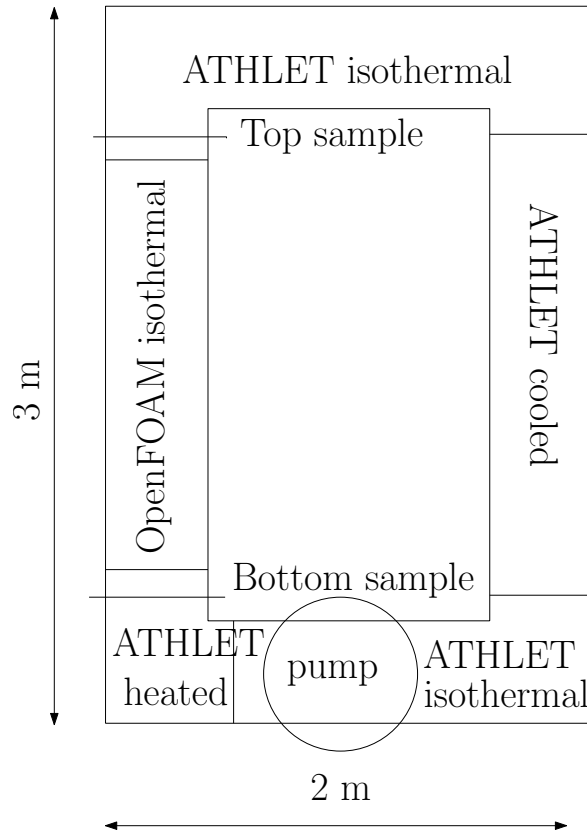
Figure 4.13: Configuration of coupling verification case no 4. Two-Phase closed Loop with Heat Transfer and Phase Change.

the amount of vapor in the loop downstream from the heated section. At about 10 s of simulation time, a maximum in void fraction is reached. At this time, the mass flow rate has not reached its peak yet, so that the fluid is still accelerating. When the mass flow has reached its steady state at 17 s, the void fraction also reaches a steady state. The values of void fraction peak and steady state of coupled simulation and ATHLET standalone are close, with a slightly higher void fraction in the coupled case. This higher void fraction can be explained by the lower mass flow in the coupled case.

In figure 4.15, the liquid- and the vapor velocities are shown at time step $t = 30s$. They show typical turbulent velocity profiles, with a slightly higher velocity for the vapor phase. As this is horizontal upwards bubbly flow, the higher vapor velocity can be explain by the lower density of the vapor phase.

Void fraction and liquid temperature are shown for the same time step in figure 4.16. The void fraction profile clearly explains the difference in void, seen in figures 4.14 (g) and 4.14 (h) in the two ATHLET samples before and after the OpenFOAM section. The subcooled mixture enters the OpenFOAM section with a void fraction of about 0.5 %. Because of the high subcooling, the vapor bubbles condense quickly in the first half of the OpenFOAM pipe. Pure water leaves the OpenFOAM section. The liquid temperature profile, shown in figure 4.16 (b) shows the slight increase in liquid bulk temperature over time seen in figure 4.14 (e) and 4.14 (f) in the ATHLET samples. The bottom of the pipe is warmer than the top.
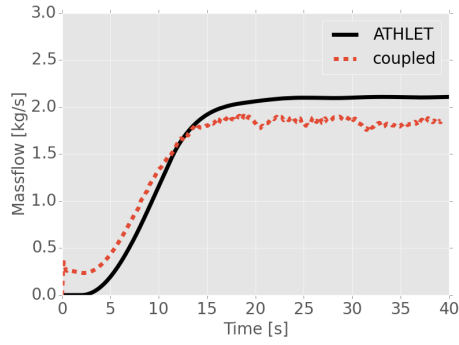
(a) Massflow at the bottom sample.
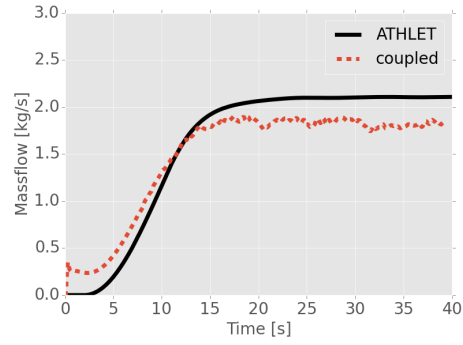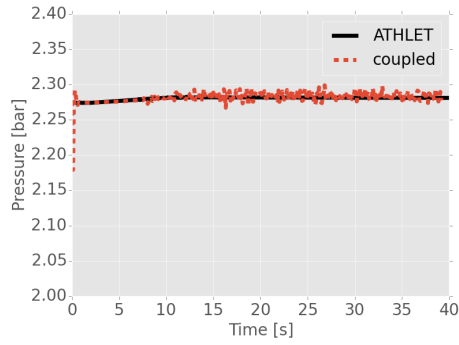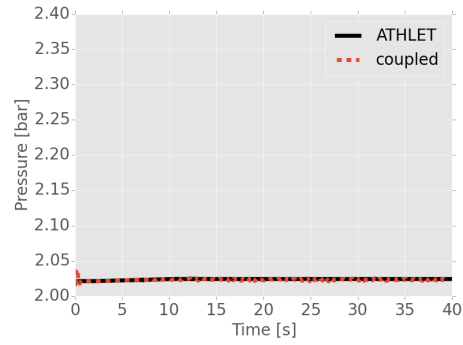
(b) Massflow at the top sample.

(c) Pressure at the bottom sample.

(d) Pressure at the top sample.
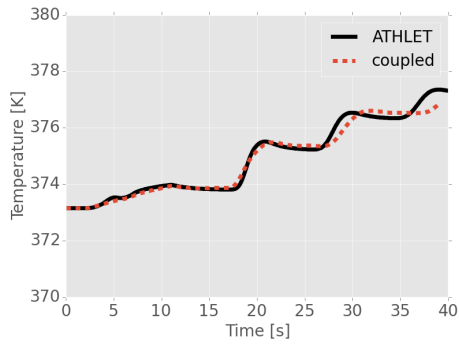
(e) Liquid temperature at the bottom sample.
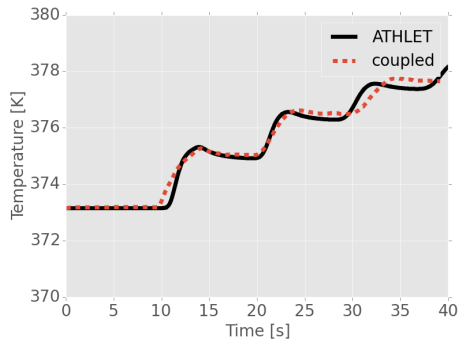
(f) Liquid temperature at the top sample.
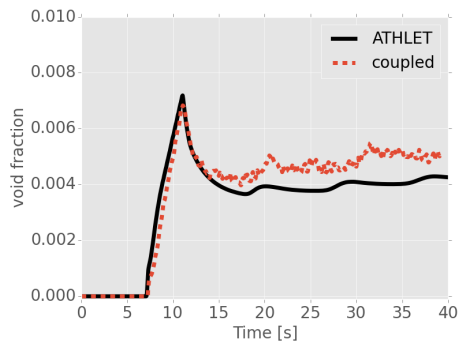
(g) Void fraction at the bottom sample.
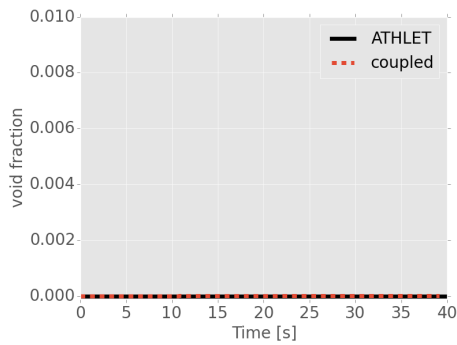
(h) Void fraction at the top sample.

Figure 4.14: Comparison of coupled two phase OpenFOAM-ATHLET simulation with ATHLET standalone in a heated loop. Driving pressure head is obtained from a pump. Case No. 4.
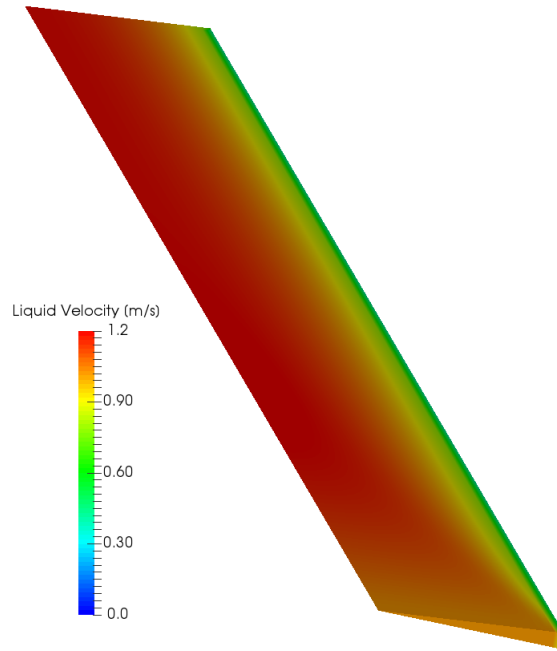
(a) Liquid velocity at time $t = 30s$.
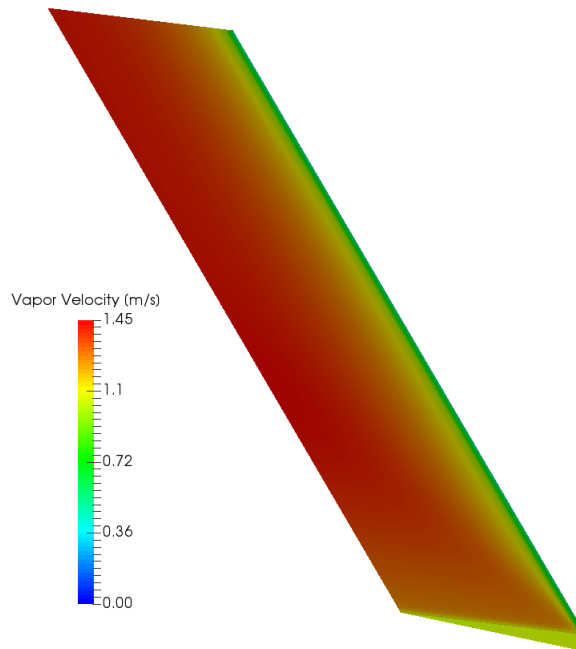
(b) Vapor velocity at time $t = 30s$.

Figure 4.15: Liquid and vapor velocity at time $t = 30s$ for the OpenFOAM part. Case No. 4.
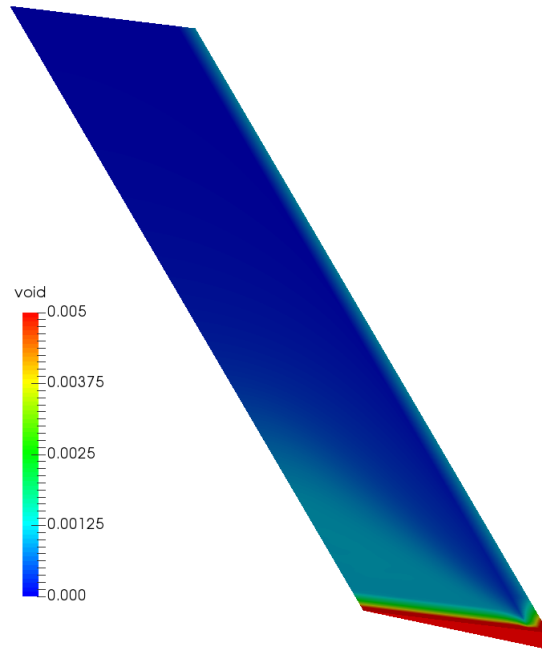
(a) Void fraction at time $t = 30s$.
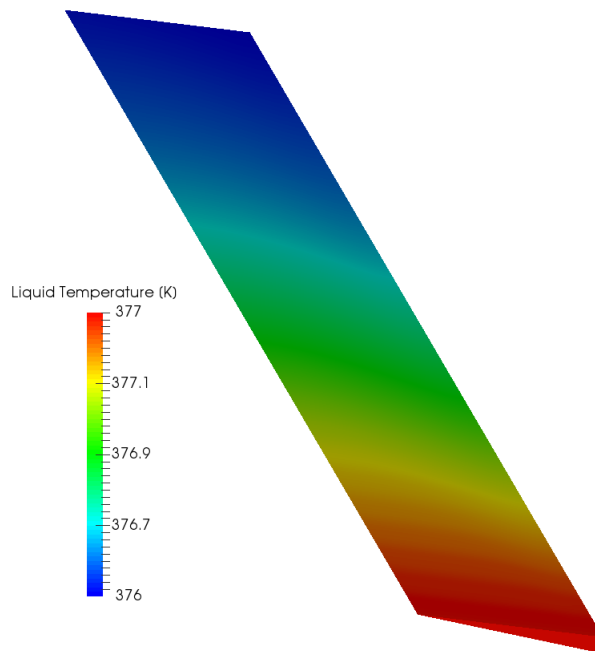
(b) Liquid temperature at time $t = 30s$.

Figure 4.16: Void fraction and liquid temperature at time $t = 30s$ for the OpenFOAM part. Case No. 4.

5. Validation

Validation of the software packages used for numerical simulations is of great importance, especially in the case of free software. With many collaborators working on the software and lots of changes introduced every day, validation and code review are the only ways to ensure that the version one is working with is behaving in an expected way. In this chapter, the results of a series of recalculations of experiments available in the literature will be presented and discussed. This chapter is divided into two parts. At first, the recalculation of a melting and solidification experiment will be explained followed by a series of recalculations of experiments done with the Eulerian two-fluid solver. This choice of experiments has been made as solidification and two-phase flow heat transfer can be seen as the most challenging and unusual physical phenomena related to an IVR-scenario. Lots of experimental data of subcooled nucleate flow boiling is available in the literature, so that the most common experiments have been chosen to simplify the comparison with the results of other numerical results published. Authors that have chosen the same experiments (or some of them) for the validation of their codes are Bui et al. (2013), Krepper and Rzehak (2011), Janssens-Maenhout (1999) or Yao and Morel (2004) for example. An overview of the selected experiments for validation of the CFD solver is given in table 5.1.

Table 5.1: Validation Matrix of CFD solver.

Typ	Author	Geometry	Target
Melting/Solidification	Gau and Viskanta (1986)	box	melting front progression
Two-phase isothermal	Bestion et al. (2009)	vertical pipe	radial void fraction distribution, IAC
SNB	Bibeau and Salcudean (1994)	annulus	wall temperature, cross section average void fraction
SNB	Bartolomei et al. (1980)	vertical pipe	cross section average void fraction
SNB	Lee et al. (2002)	annulus	radial void fraction distribution
SNB/CHF	Russian academy of science	vertical pipe	high heat flux
SNB/CHF	Park et al. (2013)	2D half sphere	high heat flux

5.1 Solidification and Melting

The method described in chapter 2.5 has been successfully employed by Gubaidullin (2001) to recalculate experiments with natural convection in solid liquid phase change pools with internal heat sources. This model has not been implemented in the scope of this thesis into OpenFOAM, but is available from the main upstream repository. As no validation of the implementation of this model is known to the author of this study, a recalculation of an experiment involving convection and melting/solidification will be performed.

Description of the Melting/Solidification Experiment by Gau and Viskanta (1986)

The experimental setup by Gau and Viskanta (1986) consists of a box filled with initially solid gallium at a temperature of 301.45 K. The dimensions of the box are 88.9 mm in x direction and 63.6 mm in y direction and 38.1 mm in z direction (see figure 5.1 for a schematic drawing of the experimental setup). The left wall is held at a constant temperature of 311.15 K and the right wall at 301.45 K while the top and bottom walls are assumed to be adiabatic. The melting temperature of gallium is 302.93 K, density ρ 6093.0 $\frac{kg}{m^3}$ and the linear thermal expansion coefficient β is $1.2 * 10^{-4}$ $\frac{1}{K}$. The latent heat of fusion L is 80160.0 $\frac{J}{kg}$, the specific heat capacity c_p 381.5 $\frac{J}{kgK}$ and a dynamic viscosity η of $1.81 * 10^{-3}$ $\frac{kg}{ms}$. A summary of the material properties of gallium is given in table 5.2.

Table 5.2: Material Properties of Gallium taken from Rösler and Brüggemann (2011)

Property	value
Density [ρ]	6093.0$\frac{kg}{m^3}$
Linear thermal expansion coefficient [β]	$1.2 * 10^{-4}$ $\frac{1}{K}$
Thermal conductivity [λ]	32.0$\frac{W}{mK}$
Melting point [T_m]	302.93K
Latent heat of fusion [L]	80160$\frac{J}{kg}$
Specific Heat capacity [c_P]	381.5$\frac{J}{kgK}$
Dynamic Viscosity [η]	$1.81 * 10^{-3}$ $\frac{kg}{ms}$

Description of the Numerical setup - Melting/Solidification

A 2D computational domain is used to represent the box. The spacial discretization is done with 88 cells in x direction and 64 cells in y direction. A mesh study with meshes of dimension 176 by 128 and with 352 by 256 cells has been performed and the solution of the small mesh can be considered as mesh independent. The velocity boundary condition on all walls is a no-slip boundary condition. Fixed temperature boundary conditions have been applied to the hot and cold wall and zero gradient boundary conditions have been applied to the adiabatic walls. An overview of the numerical boundary conditions is given in table 5.3.

Table 5.3: Boundary Conditions for Simulation of Melt Front Experiments.

| Property	PatchName	BC Type	Value
Temperature	$wall_{hot}$	Dirichlet	311.15 [K]
Temperature	$wall_{cold}$	Dirichlet	301.45 [K]
Temperature	adiabaticWalls	von Neumann	$0[\frac{K}{m}]$
Velocity	$wall_{hot}, wall_{cold}, adiabaticWalls$	Dirichlet	$(000)[\frac{m}{s}]$
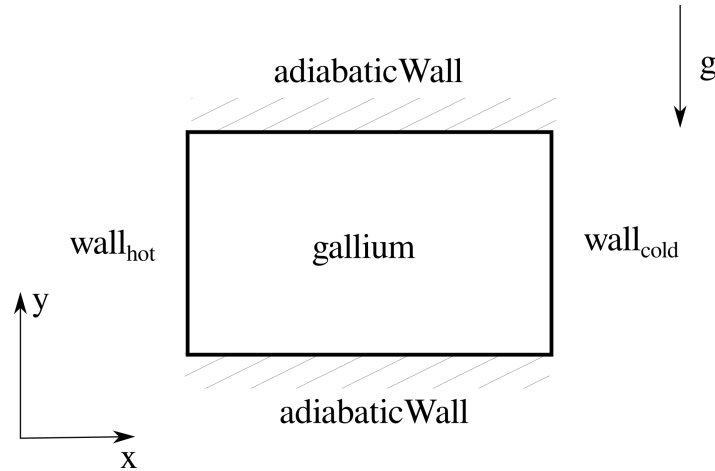
Figure 5.1: Schematic setup of melting experiment by Gau and Viskanta (1986).

Numerical results - Melting/Solidification

Gallium is heated from the left wall above its melting point of 302.93 K and starts to liquefy. A natural circulation flow is established due to the buoyancy force caused by the density difference between hot and cold gallium. The position of the melt front at different times is available as experimental data for comparison with the numerical results. In figure 5.2, the velocity vectors are plotted after 600 s into the simulation domain. Their magnitude is represented by the underlying color. It can be seen that a natural circulation flow with one big cell in the upper half of the box is established while the right half of the gallium is still frozen. The maximum velocity is located near the heated wall.

A comparison of the melt front computed by the simulation and the experimental results is given in figure 5.3. The melt front is reported at times 120 s, 360 s, 600 s and 1020 s. Experimental data is denoted by triangles and simulation results by stars with the same color for the same time step.

At the earliest time reported (120 s), the melt front is almost a straight vertical line, which leads to the assumption that no natural circulation cell has been formed at this time. This behavior is captured by the simulation with a light tendency to over-predict the melt progression in the upper part. As the time goes on, the formation of a natural circulation cell is clearly visible due to the round shape of the upper part of the melt front. The position of the melt front at 360 s has the greatest deviation from the experimental data, but only in the upper part of the melt front, the lower part is still captured exactly by the simulation. In the latest time reported (1020 s), perfect agreement of the simulation and the experimental data is achieved.

The model for solidification and melting found in the upstream repository of OpenFOAM is capable to simulate convection combined with melting/solidification phenomena.
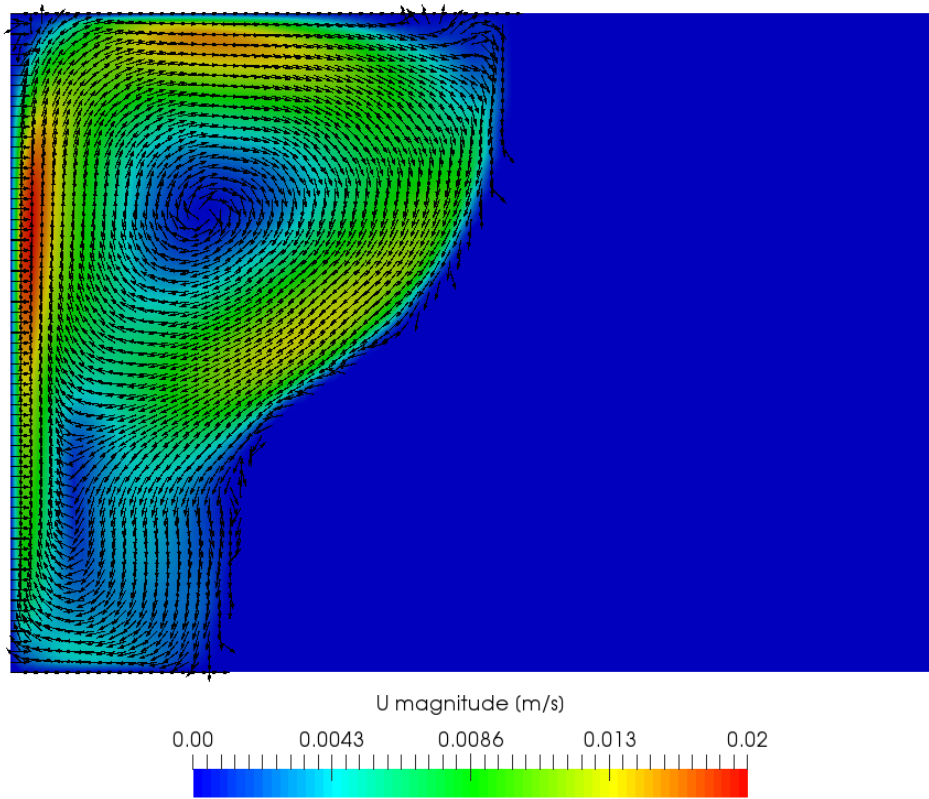
Figure 5.2: Velocity vectors 600 s after the start of the simulation. Natural circulation loop is established in the molten area.
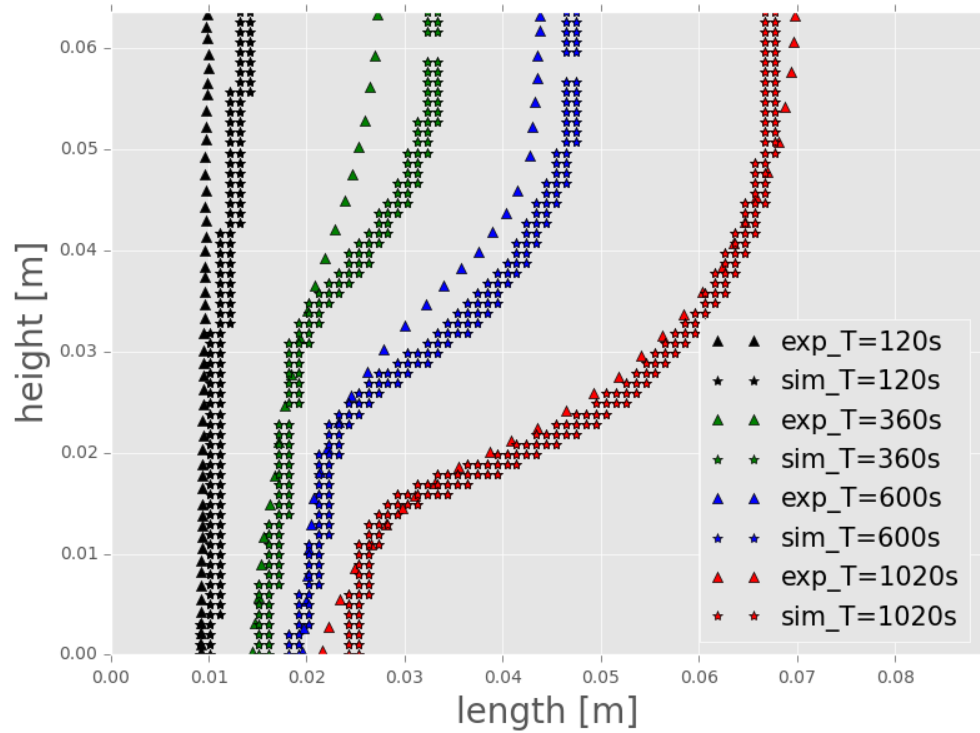

Figure 5.3: Comparison of experimental data from Gau and Viskanta (1986) with simulation results. Temporal evolution of the melt front.

5.2 Two-Phase Flow

Validation of the two-phase flow solver is carried out in three steps. In the first step, the influence of the most important models for isothermal flows is studied. Different models for drag force and the influence of bubble diameter on the velocity profile and void fraction distribution are compared with experimental data of upwards bubbly pipe flow. The second step is the comparison of void fractions and velocity profiles under subcooled nucleate boiling conditions. For all simulations, the same set of models for interfacial momentum transfer as described in chapter 2.3 has been applied unless stated otherwise. Table 5.4 gives a compact list of these models. Simulation results will be compared with three different experiments, two in an annular geometry and one pipe flow experiment. The last step of the validation is the recalculation of two experiments with high heat fluxes. The first one is a simple pipe geometry and the second one a geometry, which is representative for a lower head of a reactor pressure vessel.

Table 5.4: Models for interfacial momentum transfer.

Force	Model
Drag	Schiller and Naumann (1933) or Ishii and Zuber (1979)
Lift	Behzadi et al. (2004)
Turbulent Dispersion	Burns et al. (2004)
Virtual Mass	Constant; 0.5
Wall	Antal et al. (1991)

5.2.1 Isothermal Two-Phase Flow

Grossetete (1995) conducted experiments with adiabatic air water bubbly flow in pipes. These experiments will be used to validate the CFD solver under adiabatic two-phase flow conditions and to examine the influence of different models for drag force and interfacial area concentration.

Description of the experiment by Grossetete (1995) - Isothermal Two-Phase Flow

Working fluid of these experiments is an adiabatic ($T = 303.15K$) air - water mixture at atmospheric pressure. The test section is a vertical pipe with a length of 6 m and an inner diameter of 38.1 mm. Air is injected at the bottom of the pipe through 80 holes with a diameter of 0.6 mm. The exact placement of these holes in not described. The data used for comparison are water and air velocity profiles, and void fraction profiles at two different measurement locations. The position of the measurements are expressed by multiples of the inner diameter of the pipe d. The first measurement location is at $\frac{y}{d} = 55$ and the second one at $\frac{y}{d} = 155$. A comparison will be made for two different runs of the experiment, one with low inlet void fraction (run 1101) and one with high inlet void fraction (run 1103). Both runs share the same superficial liquid velocity J_l of 0.877 $\frac{m}{s}$. Run 1101 has a superficial air velocity J_g of 0.0588 $\frac{m}{s}$ and run 1103 of 0.1851 $\frac{m}{s}$. The void fraction, that is specified as an inlet boundary condition in the simulations, is only reported as an average value at the position $\frac{y}{d} = 8$ in the experimental report. A summary of the boundary conditions for the two test cases is given in table 5.5.

Numerical setup - Isothermal Two-Phase Flow

The geometric domain was discretized with a 5 degree 2D wedge. Three different meshes were used for the mesh sensitivity study. The first mesh with 20 cells in radial direction and 200 in axial, the second with 30 cells in radial direction and again 200 in axial and a

Table 5.5: Boundary conditions for isothermal experiments by Grossetete (1995).

Run No	J_l $[\frac{m}{s}]$	J_g $[\frac{m}{s}]$	p $[bar]$	void fraction	T $[K]$
1101	0.877	0.0588	1.0	0.048	303.15
1103	0.877	0.1851	1.0	0.152	303.15

third mesh with 30 cells in radial direction and 300 cells in axial direction. The turbulence model employed was the mixture k-epsilon model described in chapter 2.2. A fixed time step of 0.001 seconds was used for all simulations. Material properties of air and water at atmospheric pressure were obtained from the cool prop library (Bell et al. (2014)).

Mesh sensitivity study - Isothermal Two-Phase Flow

Results of the mesh study for run 1101 are shown in figure 5.4. The differences in velocities between the different mesh sizes for both locations are negligible. Only the void fraction distribution shows a small difference when the mesh is refined in the radial direction. The overall agreement for both water and air velocity with the experimental data is excellent. For the void fraction distribution, bigger differences can be seen. Especially at the first measurement section at $\frac{y}{d} = 55$ (see figure 5.4 (e)), the simulation results show a core peak which is not present in the experimental data. The core peak of the void fraction develops at a later point in the experiment and is visible at the next measurement section at $\frac{y}{d} = 155$ (see figure 5.4 (f)). Here the simulation is capable of capturing the peak very well. The model for the drag force in the mesh sensitivity study was the Ishii-Zuber model (see 2.56). The effect of drag model on the void fraction distribution will be studied in the next simulations. The following results were obtained with the mesh with 30 cells in radial and 200 cells in axial direction.

Influence of drag model - Isothermal Two-Phase Flow

The influence of drag model on velocity profiles and void fraction distribution is investigated in this section. Different models for drag force result in different relative velocities between the two phases. In this study, the drag models by Schiller and Naumann (1933) and Ishii and Zuber (1979) are compared. The results of this comparison are shown in figure 5.5. The Schiller-Naumann model causes a slightly higher air velocity than the Ishii-Zuber model, while the water velocities are unchanged as expected. Another noticeable difference can be seen in the void fraction distributions at both measurement locations. While both models falsely predict a core peak at the first measurement location, the difference for the Schiller-Naumann model is bigger in comparison to the experimental data than for the Ishii-Zuber Model. The same over-prediction of the core peak with the Schiller-Naumann model can be observed at the second measurement location. The conclusion can be drawn that the difference between both models is rather small, but the Ishii-Zuber model is slightly closer to the experimental data as the Schiller-Naumann model. For this reason the Ishii-Zuber model will be chosen for the rest of the simulations as the default drag force model.

Influence of bubble diameter - Isothermal Two-Phase Flow

The second parameter to be investigated is the bubble diameter or the interfacial area concentration. It is either possible to set a constant bubble diameter, which is used throughout the simulation or to solve a transport equation for the interfacial area concentration (see chapter 2.3.2). In this section, the influence of this choice of model parameter on the velocity profiles and void fraction distributions is to be investigated. Four different constant bubble diameters, 2 mm, 3, mm, 4 mm and 5 mm have been compared against experimental data and a simulation where a transport equation for the interfacial area concentration

(a) Velocity of air at $\frac{y}{d} = 55$.

(b) Velocity of air at $\frac{y}{d} = 155$.

(c) Velocity of water at $\frac{y}{d} = 55$.

(d) Velocity of water at $\frac{y}{d} = 155$.

(e) Void fraction at $\frac{y}{d} = 55$.

(f) Void fraction at $\frac{y}{d} = 155$.
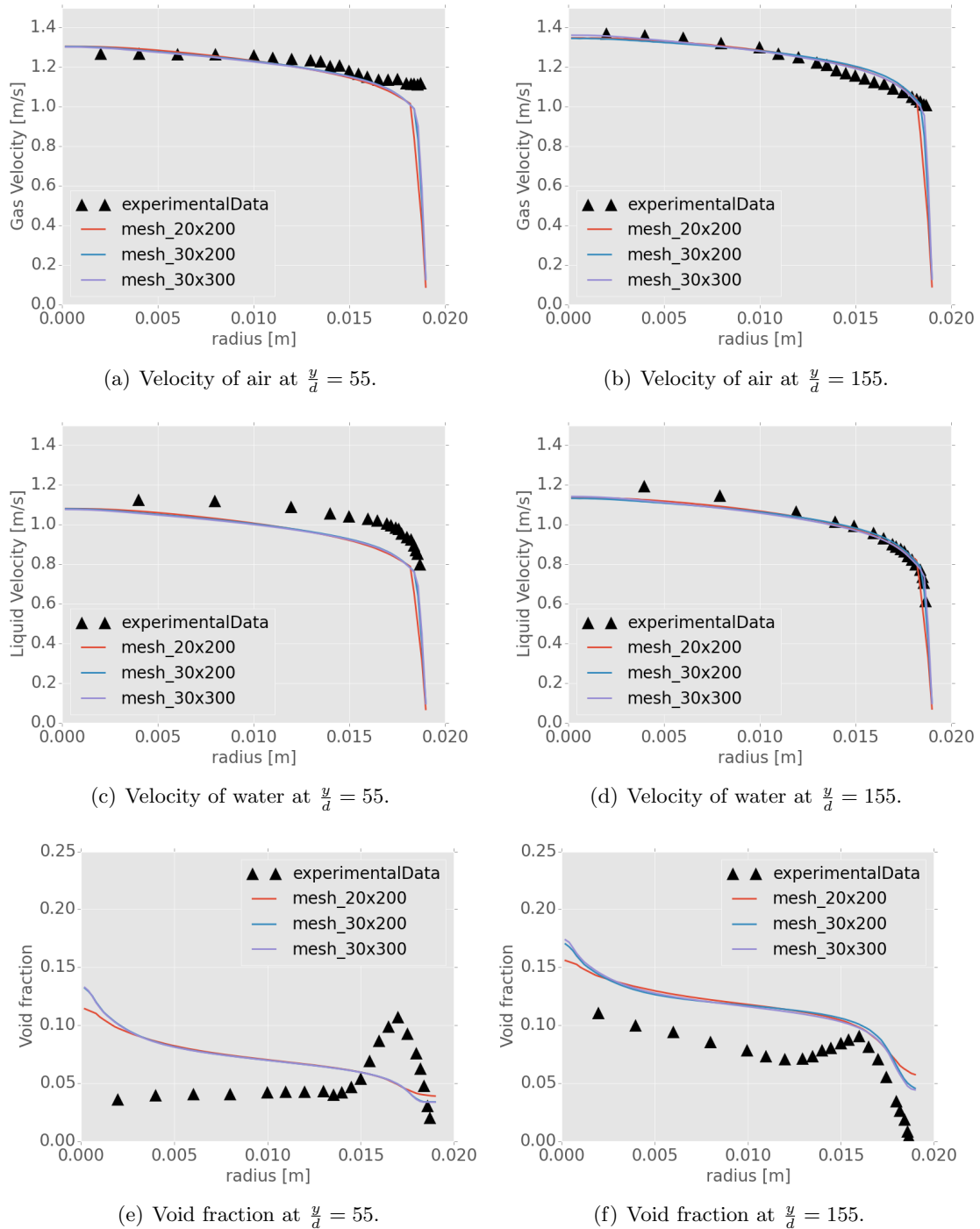
Figure 5.4: Mesh study for recalculation of isothermal experiments by Grossetete (1995).
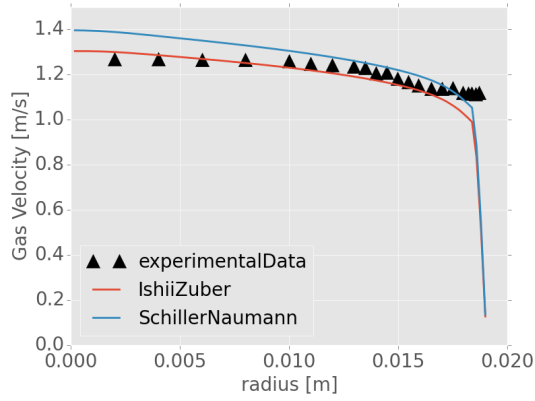
(a) Velocity of air at $\frac{y}{d} = 55$.
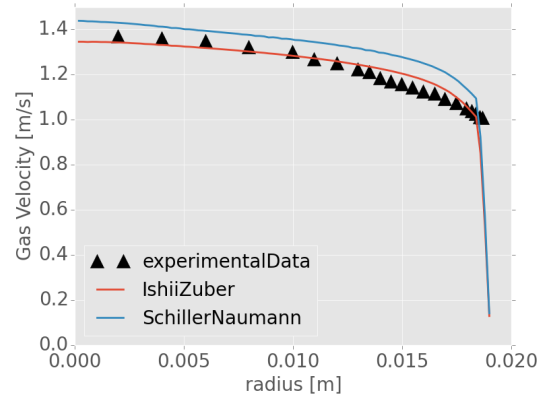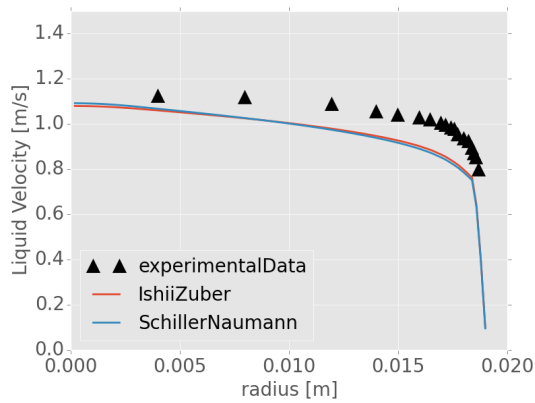
(b) Velocity of air at $\frac{y}{d} = 155$.

(c) Velocity of water at $\frac{y}{d} = 55$.
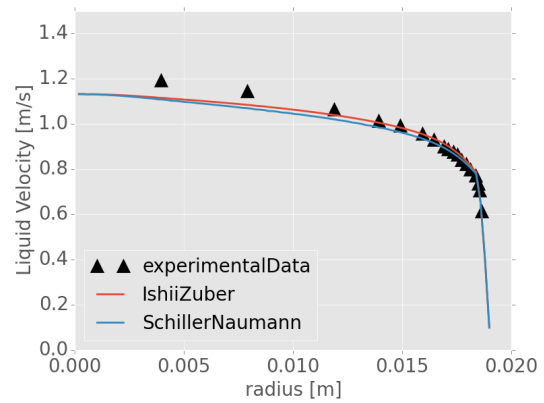
(d) Velocity of water at $\frac{y}{d} = 155$.
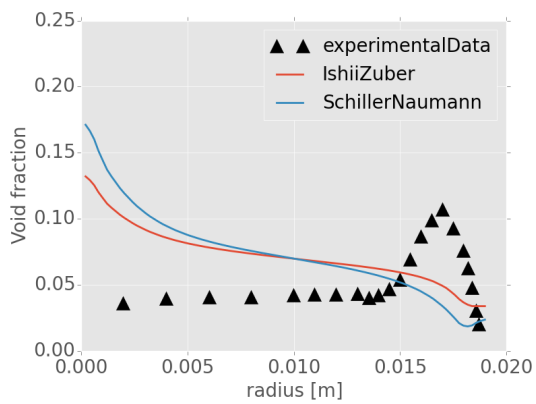
(e) Void fraction at $\frac{y}{d} = 55$.
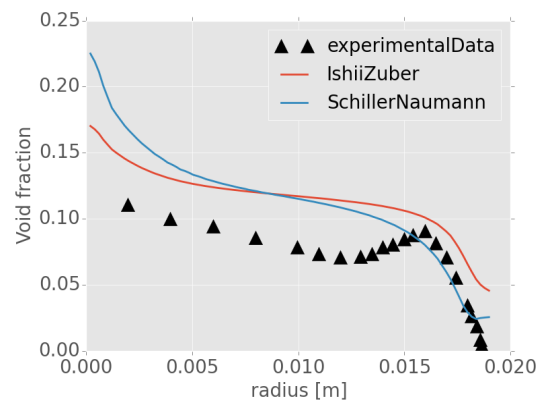
(f) Void fraction at $fracyd = 155$.

Figure 5.5: Influence of drag force modeling in case of isothermal flow.

(IATE) is solved. It can be seen that the influence of bubble diameter is hardly noticeable in this simulation. Also the extra effort for solving a transport equation for the interfacial area concentration does not lead to different simulation results.


(a) Velocity of air at $\frac{y}{d} = 55$

(b) Velocity of air at $\frac{y}{d} = 155$

(c) Velocity of water at $\frac{y}{d} = 55$

(d) Velocity of water at $\frac{y}{d} = 155$

(e) Void fraction at $\frac{y}{d} = 55$

(f) Void fraction at $\frac{y}{d} = 155$
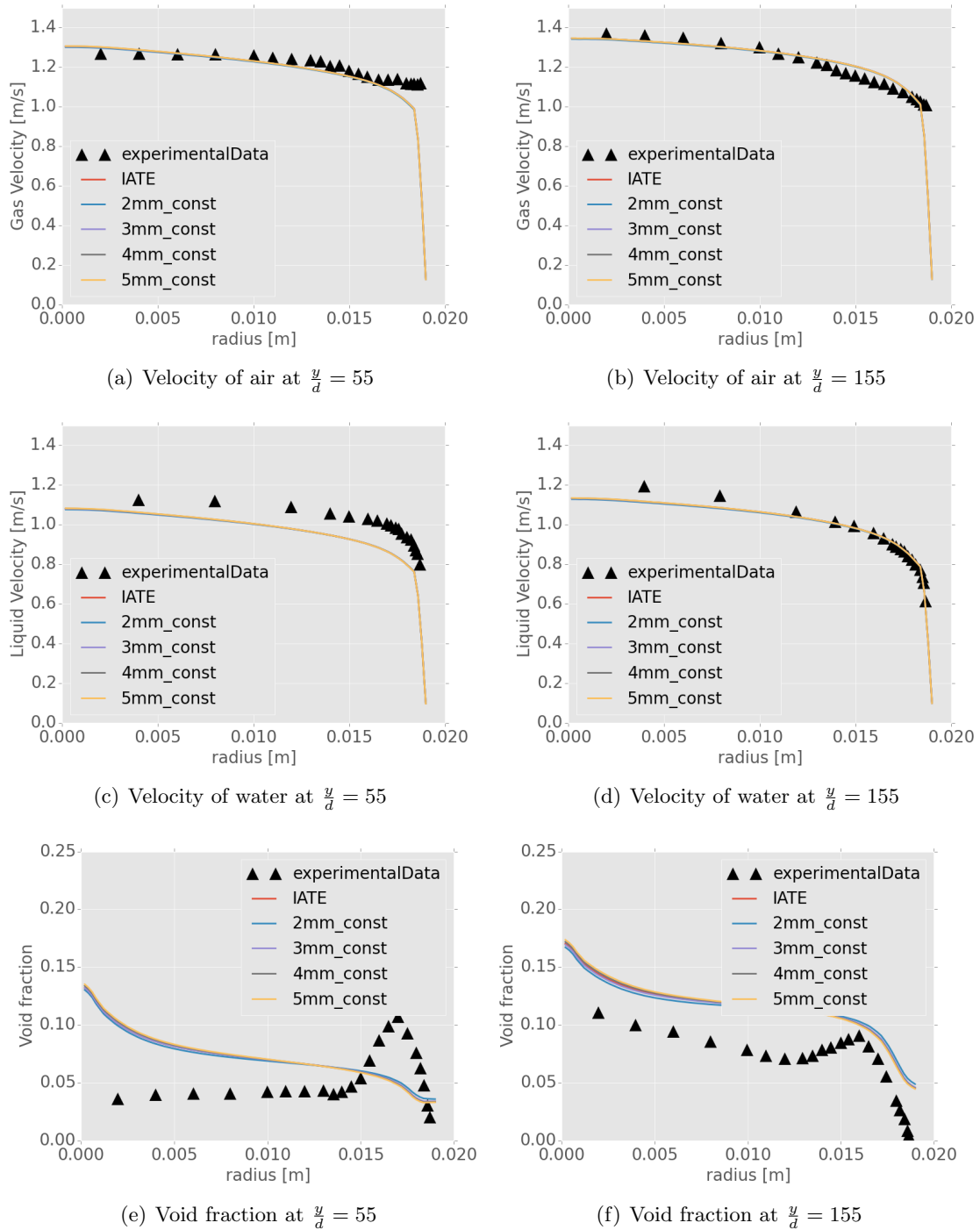
Figure 5.6: Influence of modeling the interfacial area concentration or bubble diameter

Influence of initial void fraction - Isothermal-Two Phase Flow

The last recalculation of an isothermal experiment is done to investigate the behavior of the solver under higher void fractions. The influence of the dispersed phase is becoming greater which challenges the modeling of the turbulence. Also different profiles for void fractions are to be expected. The results of the recalculation of run 1103 are shown in

figure 5.7. The experimental void fraction distribution at location $\frac{y}{d} = 155$ indicates that a transition from bubbly flow to a slug regime has appeared. As the bubble shapes differ from a spherical shape, the models loose their validity. It is nevertheless interesting to observe the behavior of the solver, as in the later cases, at high heat flux situations, distorted bubble shapes can also be expected to occur. In general, it can be seen that the simulated velocity profiles are in agreement with the experiment, especially at the first measurement location. The largest deviation of simulated data from experimental data can be observed in the middle of the pipe at the second measurement location. The void fraction profile at the first measurement section is in good agreement with the experimental data, although again the wall peak is under-predicted by the simulation. But the agreement in the core region is even greater than for the case of low void fraction. After the flow regime transition (at $\frac{y}{d} = 155$), the simulation has greater difficulties to catch the trend of the experimental data and only a qualitative agreement can be achieved (see figure 5.7 (f)).

Conclusion of Validation - Isothermal Two-Phase Flow

The recalculation of isothermal experiments and the comparison of the simulation results with the experimental data has been done to asses the capabilities of the Eulerian two-phase flow solver available in OpenFOAM under isothermal flow conditions. The results achieved, for the velocities of the two phases, are generally in good agreement with the experimental data. Larger differences, between experimental data and simulated results, have been observed for the void fraction profiles. Possible reasons for these differences lie in the uncertainties related to the inflow conditions of the air phase. Here a uniform inlet profile was applied, as only an integral value for the inlet is known from the experiments. This validation step is important to rule out possible errors introduced by the implementation of the models required to simulate wall heat transfer and phase change by evaporation and condensation. The influence of chosen models for drag force or bubble diameter can be considered as small in case of isothermal flow in comparison to the measurement uncertainties usually associated with two-phase flows.

(a) Velocity of air at $\frac{y}{d} = 55$

(b) Velocity of air at $\frac{y}{d} = 155$

(c) Velocity of water at $\frac{y}{d} = 55$

(d) Velocity of water at $\frac{y}{d} = 155$

(e) Void fraction at $\frac{y}{d} = 55$

(f) Void fraction at $\frac{y}{d} = 155$
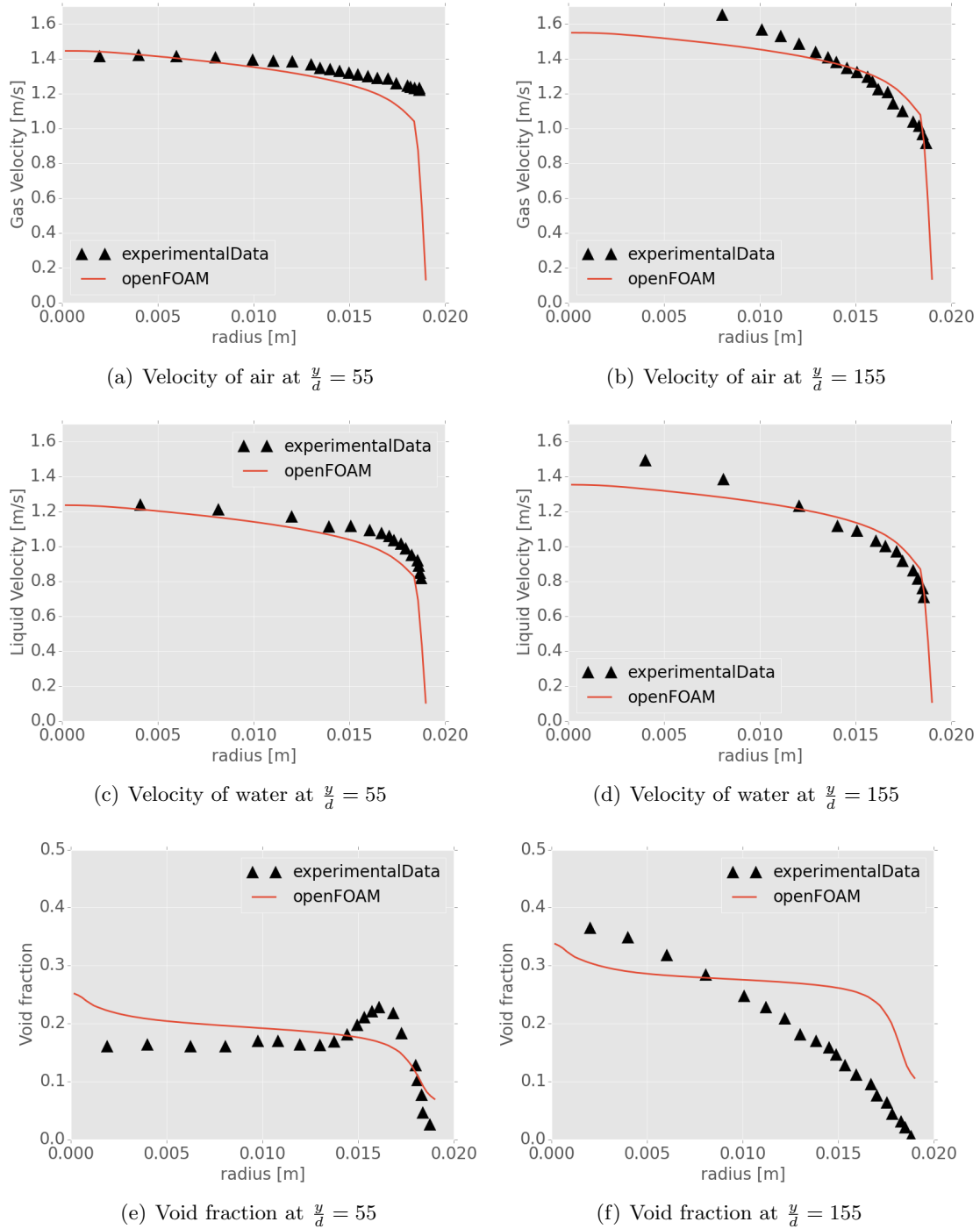
Figure 5.7: Validation against isothermal experimental run 1103 (High void fraction case).

5.2.2 Two-Phase Wall Heat Transfer Solver Validation

The second part of the validation process for the two-phase flow solver is the validation of the newly developed and implemented model for wall heat transfer under subcooled nucleate flow boiling conditions. At first three experiments at subcooled nucleate boiling conditions will be recalculated and compared with their experimental data. Later, the two experiments with higher wall heat flux will be recalculated and evaluated.

Experiments by Bibeau and Salcudean (1994)

Bibeau and Salcudean (1994) conducted flow boiling experiments in a vertical annular geometry, with water as the working fluid. The heated rod had a diameter of 9 mm and the glass tube surrounding the rod had an inner diameter of 17 mm. The rod was heated uniform over its entire length of 0.6 m. Wall temperatures and cross-section averaged void fractions were reported at the distance of 0.55 m from the inlet. The experimental setup is shown in figure 5.8.
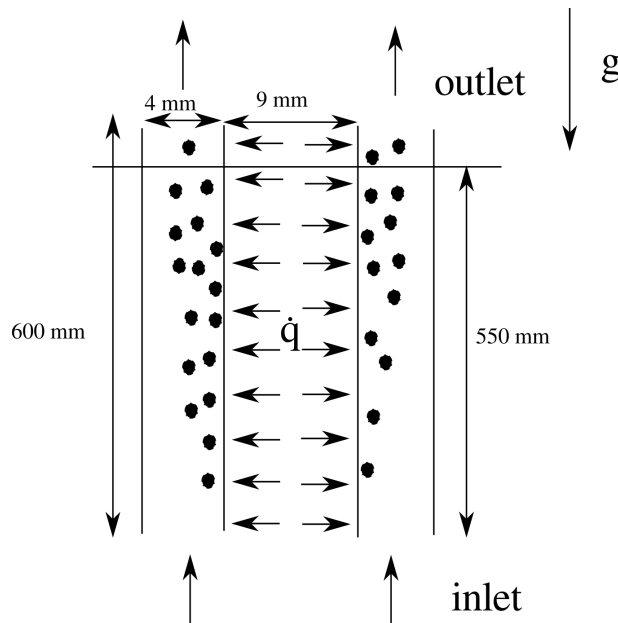

Figure 5.8: Experimental setup of the wall boiling experiments by Bibeau and Salcudean (1994).

The pressure at the outlet was 2 bar and subcooled water with an inlet temperature of $303K$ were supplied to the test section. The low mass flow rate of 0.02 $\frac{kg}{s}$ leads to a laminar flow pattern. Different heat fluxed were applied at the rod surface and a range of $10 - 200$ $\frac{kW}{m^2}$ was chosen for recalculation. The corresponding equilibrium quality was calculated as

$$x_{eq} = \frac{\frac{q\pi d_{rod}l}{G} + c_{p,l}\Delta T_{sub}}{i}. \tag{5.1}$$

With the heated length of the rod l. Table 5.6 gives an overview of the boundary conditions for this experiment.

Table 5.6: Boundary conditions for flow boiling experiments by Bibeau and Salcudean (1994).

p_{out} [bar]	q [$\frac{kW}{m^2}$]	G [$\frac{kg}{s}$]	T_{in} [K]
2	10-200	0.02	303

Numerical Setup - Bibeau cases

A 2D, five degree wedge geometry was used for the simulation. The mesh had 20 cells in radial and 200 cells in axial direction. To prevent flow reversal at the outlet, the geometry was enlarged with an outlet region of 0.2 m. As the flow pattern is expected to be laminar, no turbulence model was applied in this simulation. This also leads to a boiling suppression factor (S_{total}) of 1. As no turbulence is expected, no interfacial model for turbulent dispersion is used in the recalculation of this experiment. No bubble diameter has been reported for this experiment, so that it has to be estimated. A bubble diameter of 1 mm has been chosen for all recalculations. Six different simulations with heat fluxes of 10 $\frac{kW}{m^2}$, 100 $\frac{kW}{m^2}$, 120 $\frac{kW}{m^2}$, 150 $\frac{kW}{m^2}$, 175 $\frac{kW}{m^2}$ and 200 $\frac{kW}{m^2}$ were run to a steady-state.

Numerical Results - Bibeau cases

The results for the six recalculations of the experiments by Bibeau and Salcudean (1994) are shown in figure 5.9. In figure 5.9 (a), wall temperatures at the sampling location are compared and figure 5.9 (b) shows the comparison of the integral void fractions at the sampling location, which was located 0.55 m from the inlet. The wall temperatures, as well as the void fractions, are slightly under-predicted by the simulations, although the general trend is being captured well for both quantities. The transition from pure single-phase convection, at the lowest heat flux of 10 $\frac{kW}{m^2}$, to the onset of nucleate boiling, at a heat flux of 100 $\frac{kW}{m^2}$, is clearly visible. The lower integral void fractions could be a result of a too small chosen bubble diameter. The larger interfacial area could lead to an over-prediction of condensation in the highly subcooled bulk fluid in this experiment.


(a) Wall temperature over quality.

(b) Cross-section averaged void fraction over quality.
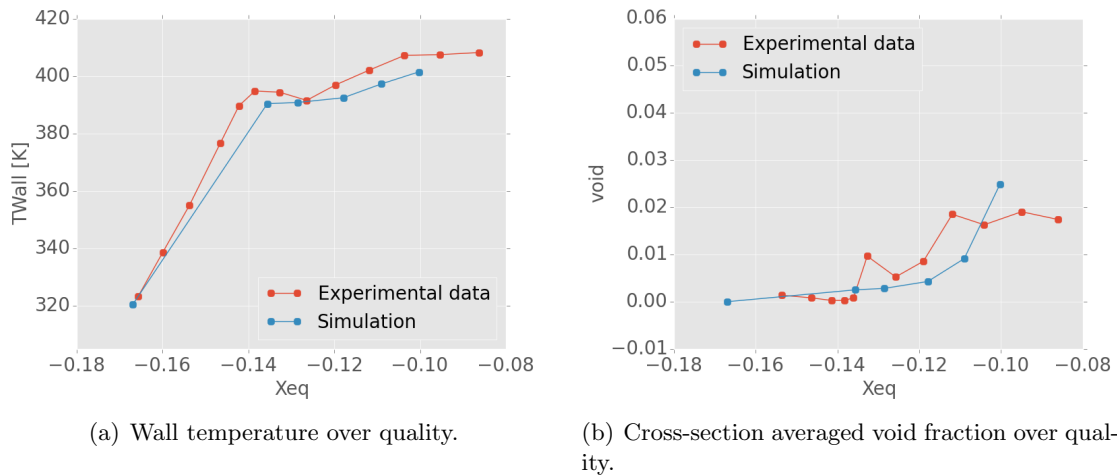
Figure 5.9: Comparison of experimental wall temperature and void fraction with recalculation results for experiments by Bibeau and Salcudean (1994).

Experiments by Bartolomei et al. (1980)

Bartolomei et al. (1980) conducted experiments on subcooled nucleated flow boiling of water in a heated pipe. The flow direction is upwards. The data used for comparison in this study is the data republished by Ustinenko et al. (2008) as the original publication is not available to the authors of this study. The pipe has an inner diameter of 12.03 mm. The interesting part of the experiments is the division of the pipe in the axial direction into a heated and an adiabatic section. As the water enters the heated section, with a certain subcooling T_{sub}, it gets partly evaporated at the heated wall. In the adiabatic section, the water is condensed as the bulk temperature is still below the saturation temperature. This helps to validate the separate models of evaporation and condensation of the numerical

solver. The heated section has a length of 1 m and the adiabatic section is 0.4 m long. A schematic drawing of the test section is given in figure 5.10. Three runs of the series of experiments will be recalculated in the following. All experiments have been conducted at the same pressure of 6.89 MPa, which can be seen as a reference pressure for a BWR subchannel flow. The experimental runs differ in mass flux, wall heat flux and inlet subcooling. The first run has the highest wall heat flux of $q = 1.2 \frac{MW}{m^2}$, the biggest subcooling of $T_{sub} = 63 \ K$ and also the highest mass flux of $G_A = 1500 \ \frac{kg}{m^2s}$. Run number 2 shares the mass flux with run number 1, but has a lower wall heat flux of $q = 0.8 \frac{MW}{m^2}$. The inlet subcooling is also decreased to $T_{sub} = 39 \ K$. The last run has the lowest mass flux of $G_A = 1000 \ \frac{kg}{m^2s}$ and the same wall heat flux as run number 2. The inlet subcooling is between the subcooling of run 1 and 2 with $T_{sub} = 55 \ K$. The experimental data used for comparison with the numerical results are cross-section averaged void fractions at different axial positions. A summary of the experimental boundary conditions is given in table 5.7.
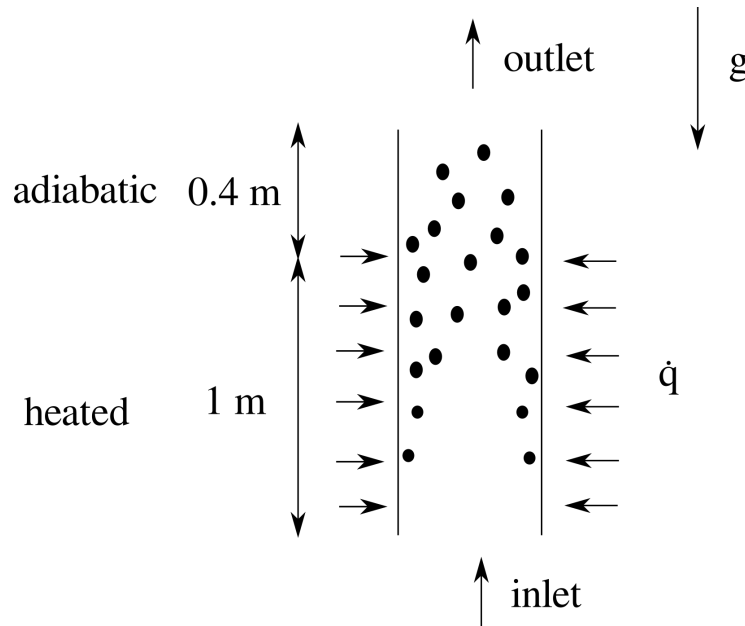

Figure 5.10: Experimental setup of the wall boiling experiments by Bartolomei et al. (1980).

Table 5.7: Boundary conditions for flow boiling experiments by Bartolomei et al. (1980).

| Case No	$q \ [\frac{MW}{m^2}]$	$G_A \ [\frac{kg}{m^2s}]$	$T_{sub} \ [K]$	$p_{out} \ [MPa]$
1	1.2	1500	63	6.89
2	0.8	1500	39	6.89
3	0.8	1000	55	6.89

Numerical Setup - Bartolomei cases

The pipe geometry is again approximated by a two dimensional 5 degree wedge. The mesh has 30 cells in radial and 480 cells ins axial direction. A mesh sensitivity study (see figure 5.11) with 240 and 480 cells in axial direction showed no difference in the results. In radial direction, 15, 20, 30 and 40 cells have been tested. The inlet was enlarged by a 1 m long inflow section. The interfacial area concentration was modeled with the transport equation described in chapter 2.3.2. The velocities at the inlet were specified with a uniform velocity distribution.
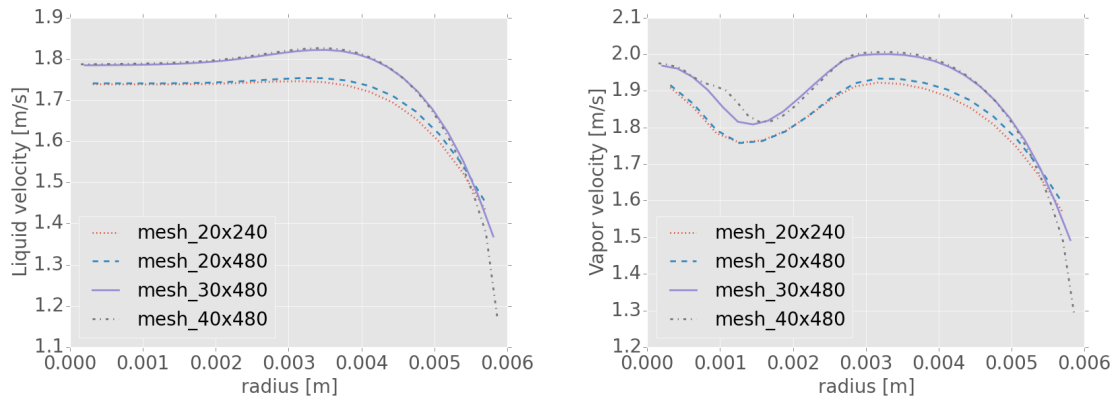
(a) Liquid phase velocity for Bartolomei case.

(b) Vapor phase velocity for Bartolomei case.
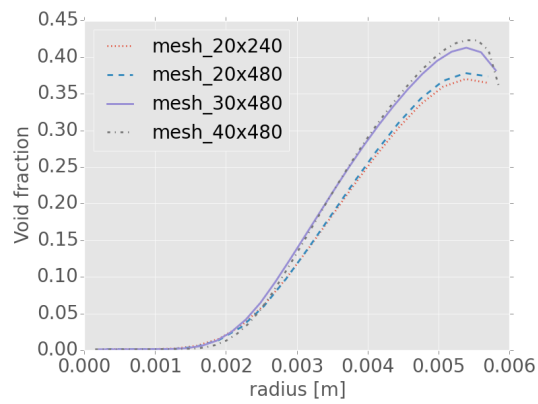
(c) Void fraction distribution for Bartolomei case.

Figure 5.11: Mesh sensitivity study for Bartolomei cases. The sampling location is 0.95 m away from the beginning of the heated section.

Numerical Results - Bartolomei cases

In figure 5.12, the results from the numerical simulations are compared with the available experimental data for the three cases. The cross-section averaged void fractions increase in all cases until they reach a maximum at 1 m distance from the inlet. This also marks the end of the heated section. After the heated section, the void fractions decrease again, caused by the condensation in the bulk as no heat is added to the fluid anymore. The results from the simulations follow this trend for all three cases. This shows that the balance between evaporation and condensation is modeled correctly. The peak values of cross-section averaged void fraction at the end of the heated sections are also captured very well, with a slight tendency to over-predict the peak value for case number one and an under-prediction for case number three. Case number three has the highest values for void fractions. This can be explained by the low mass flow for this case (heat flux is the same as case number two and the subcooling is even higher). This shows that the new wall heat flux model is capable to reproduce the suppression of boiling in case number two very well, as the predicted void fraction are much lower than for case number three. The values in the condensation region are again in good agreement with the experimental data for all cases.

Experiments by Lee et al. (2002)

While only cross-section averaged values for void fractions have been available in the previous detailed experiments, Lee et al. (2002) conducted experiments with subcooled nucleate flow boiling and measured radial void fraction profiles at one axial location. Besides the void fraction distribution, also velocity profiles for the vapor and liquid phases are available at the same location. The test section in this experiment is an annular geometry with a heated central rod. The rod has a diameter of 19 mm. The gap between the rod and the outer tube is 9.25 mm. The heated length is 1.67 m and measurements are reported at a distance of 1.61 m away from the inlet. Flow direction is again upwards. The experimental setup is schematically shown in figure 5.13. Three cases are recalculated and compared against experimental data from this series. Pressure varies between 0.142 MPa in the first run, 0.137 MPa in the second and 0.143 MPa in the third run. The wall heat flux increases from case to case starting with 152.3 $\frac{kW}{m^2}$ in the first run to 192.2 $\frac{kW}{m^2}$ in the second run and the maximum heat flux of 251.5 $\frac{kW}{m^2}$ in the third run. The mass flux of the first run is 474.0 $\frac{kg}{m^2 s}$, 714.4 $\frac{kg}{m^2 s}$ for the second run and 1059.2 $\frac{kg}{m^2 s}$ is the maximum mass flux in the last run. The difference in subcooling is rather small with 13.4 K in the first, 13.8 K in the second and 17.9 K in the last run. Table 5.8 gives an overview of boundary conditions for the three experimental runs. Experimental uncertainties have also been reported and are summarized in table 5.9.

Table 5.8: Boundary conditions for flow boiling experiments by Lee et al. (2002)

Case No	$p[MPa]$	$q\ [\frac{kW}{m^2}]$	$G_A\ [\frac{kg}{m^2 s}]$	$T_{sub}\ [K]$
1	0.142	152.3	474.0	13.4
2	0.137	192.2	714.4	13.8
3	0.143	251.5	1059.2	17.9
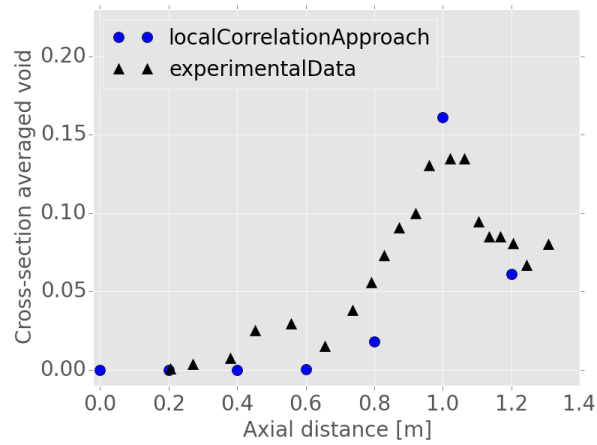
(a) Bartolomei Case No 1.
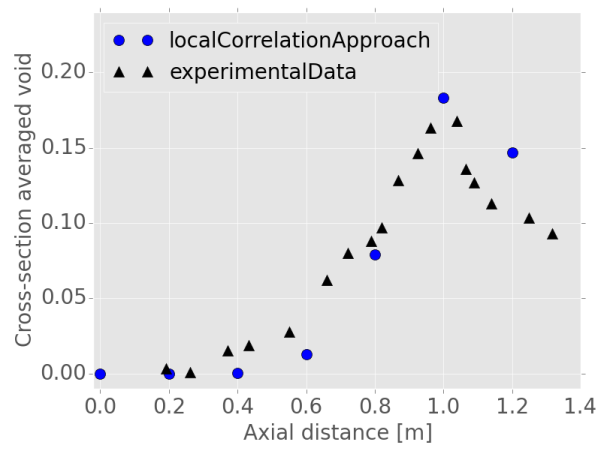
(b) Bartolomei Case No 2.
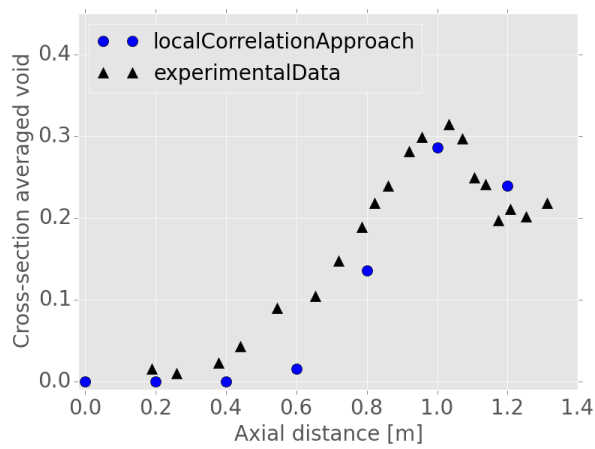
(c) Bartolomei Case No 3.

Figure 5.12: Axial evolution of cross-section averaged void fraction. Bartolomei cases 1 - 3.

Table 5.9: Uncertainties for experiments by Lee et al. (2002)

| Parameter	Uncertainty
Temperature	$\pm 0.2 K$
Pressure (inlet and measuring plane)	± 0.001 MPa and ± 0.0005 MPa
Inlet mass flux	± 1.9 %
Heat flux	± 1.7 %
Local void fraction	± 3 %
Velocity	± 3 %
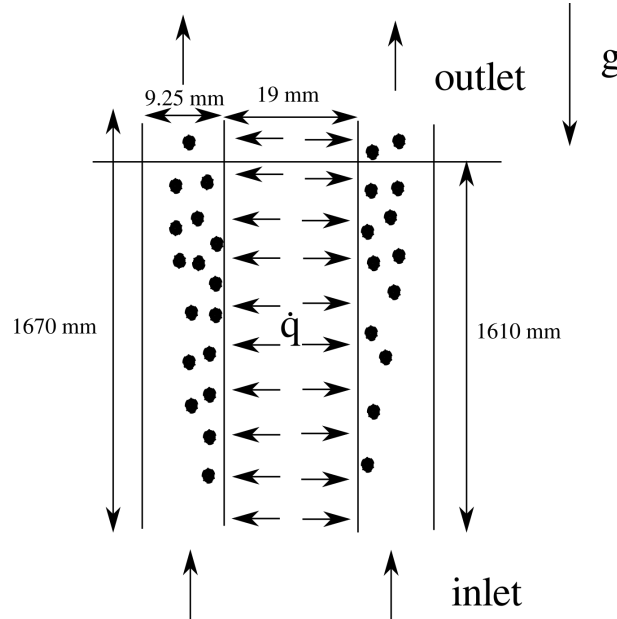
Figure 5.13: Experimental setup of the wall boiling experiments by Lee et al. (2002). Graphic from Sonntag and Cheng (2016).

Numerical Setup - Lee cases

The annular geometry is again discretized with a two-dimensional 5 degree wedge. After a mesh sensitivity study (see 5.14 for results), a mesh with 20 cells in radial and 200 cells in axial direction has been chosen for the further simulations of this series of experiments. A fixed time step of 0.0005 seconds has been set for all simulations. The simulations were initiated with a uniform temperature distribution with the value of the inlet temperature. A steady state was reached after about 5 seconds. The bubble diameter was reported by Yeoh and Tu (2006) to be about 4 *mm* for all three cases, so that this constant value was also used in the recalculation of the experiments.

Numerical Results - Lee cases

Lee case number 1 is the case with the lowest wall heat flux, but also the lowest mass flux. The experimental results show a clear void peak near the rod (see figure 5.15 (c)). The peak as well as the decrease in void away from the heated rod are perfectly reproduced by the simulation. The decrease in void with further distance to the wall is a clear sign of the condensation happening due to the subcooled bulk liquid. The liquid velocity profile is also captured very well by the simulation, while the vapor velocity is slightly over predicted by the simulation (see figure 5.15 (a) and 5.15 (b)).

(a) Liquid phase velocity for Lee case no 1.

(b) Vapor phase velocity for Lee case no 1.

(c) Void fraction distribution for Lee case no 1.
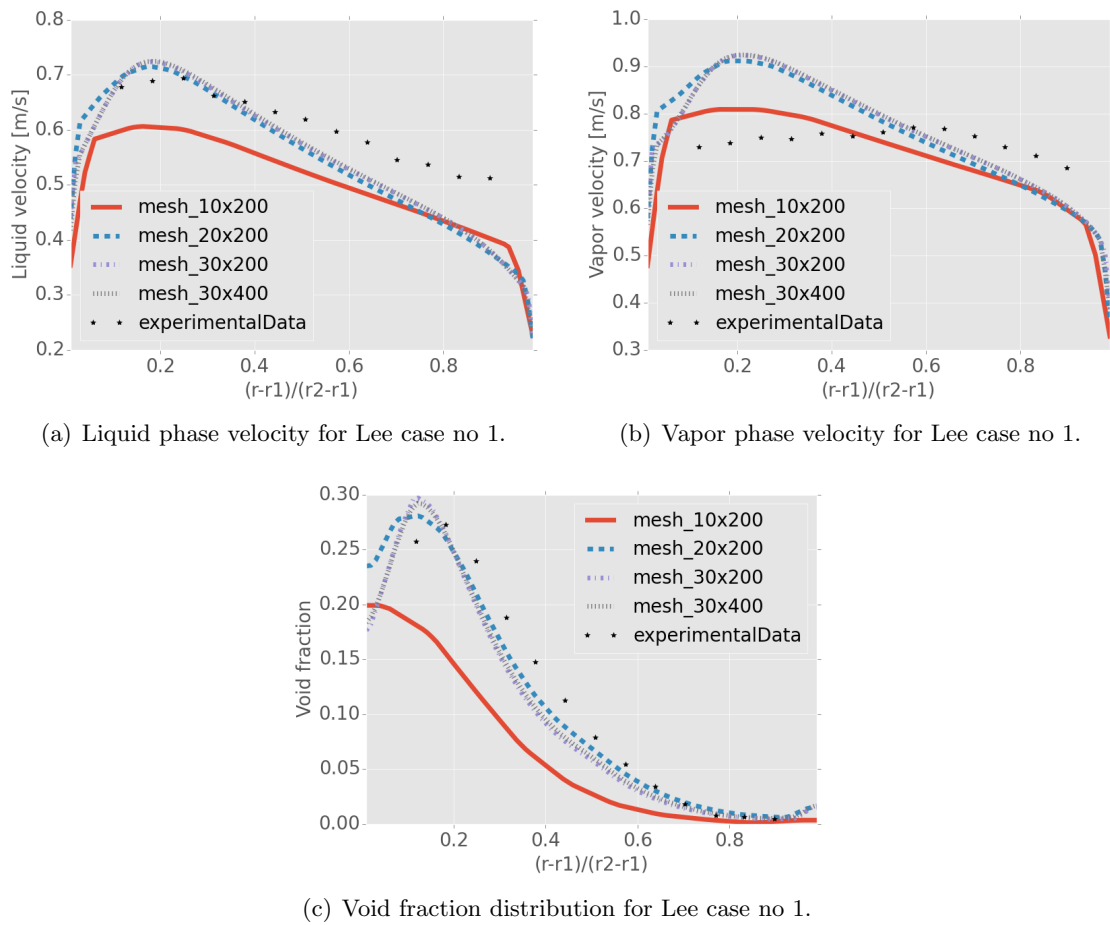
Figure 5.14: Mesh sensitivity study for boiling flow case. Lee No. 1.
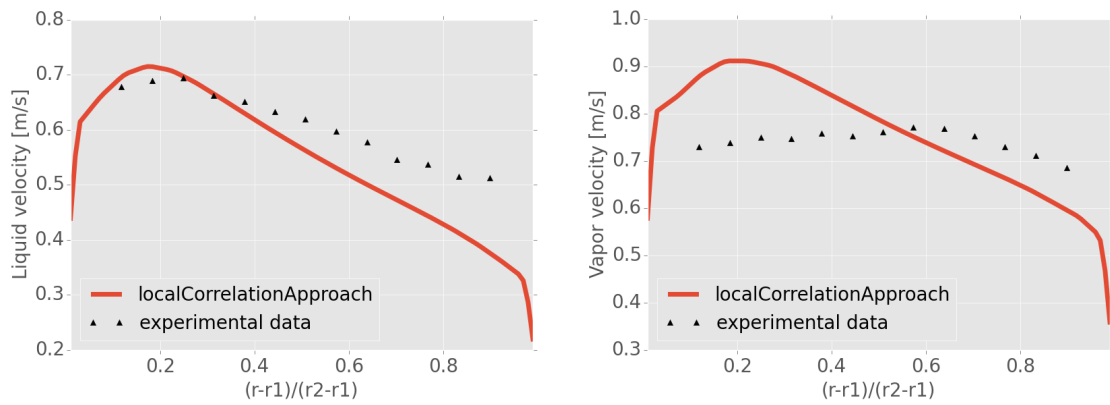
(a) Liquid phase velocity for Lee case no 1.

(b) Vapor phase velocity for Lee case no 1.
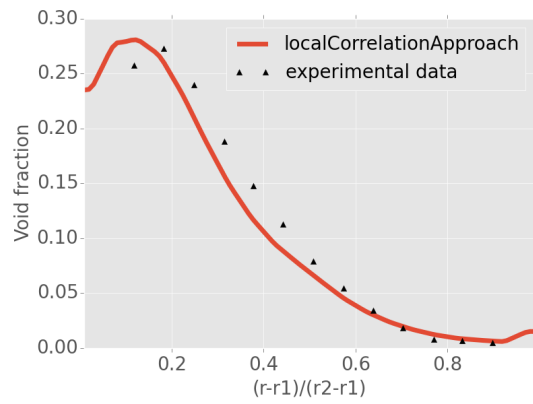
(c) Void fraction distribution for Lee case no 1.

Figure 5.15: Comparison of numerical with experimental results. Lee No. 1.

Lee case number two has a higher mass flux, but also a higher heat flux than case number one. The near rod peak is now not clearly visible anymore in the experiment, with just a maximum near the wall (see 5.16 (c)). The void fraction is decreasing continuously with a larger distance from the rod. The simulation has a problem to catch the high experimental maximum value of over 40 % void fraction and displays a maximum void of just above 25 %. This shows that the suppression of evaporation is over-estimated by the model as the higher mass flow rate seems to over-compensate for the higher wall heat flux. Important is here the comparison of the liquid velocity profile as the main driver for the boiling suppression. Figure 5.16 (a) shows good agreement of the liquid phase velocity with the experimental data. Interesting here is also the comparison of the vapor velocity (see figure 5.16 (b)), which is over estimated by the simulation. This is in contrast to the underestimated void profile, as lower vapor production should lead to lower vapor velocities.
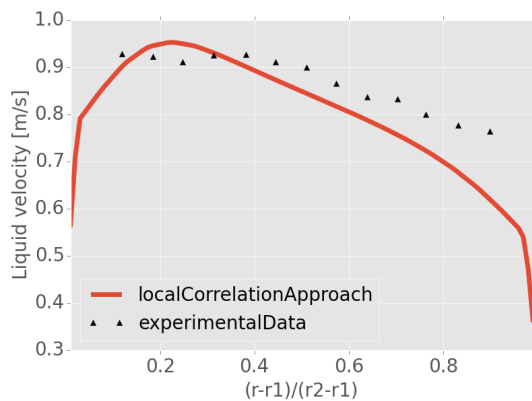
(a) Water velocity for Lee case no 2.
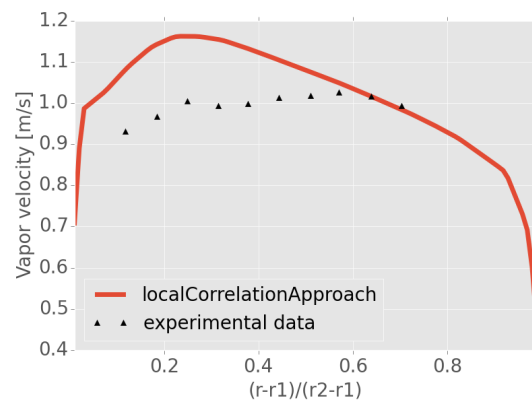
(b) Vapor velocity for Lee case no 2.
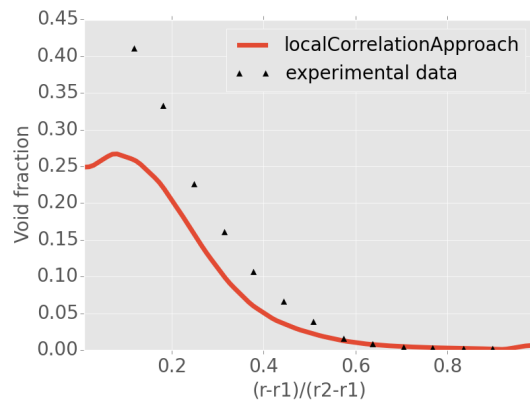
(c) Void fraction distribution for Lee case no 2.

Figure 5.16: Comparison of numerical with experimental results. Lee No. 2.

Lee case number three can be seen as a continuation of the other two cases as the mass flux as well as the heat flux is increased again. The experimental shape of the void fraction profile (see figure 5.17 (c)) is similar to case number two, with no near wall peak but a maximum at the wall. The decrease of void is also sharper than for the other cases which can be explained by the higher inlet subcooling (17.9 K in comparison to 13.8 K for case two and 13.4 K for case one). The simulation also shows the fastest decrease of void fraction and is able to catch the point where no void is present anymore at $\frac{r-r_1}{r_2-r} = 0.4$. The near wall peak in void fraction distribution is now also gone in the simulation and it shows only a maximum at the wall, which is in accordance to the shape of the experimental void fraction. The maximum value of void fraction is again under-estimated in the simulation as it was the case already in run 2. With the similar result that the liquid velocity profile is captured well (see figure 5.17 (a)) and the vapor phase velocity is slightly over predicted (see figure 5.17 (b)). This undermines the notion that the suppression of evaporation is overestimated for high mass flow rates.
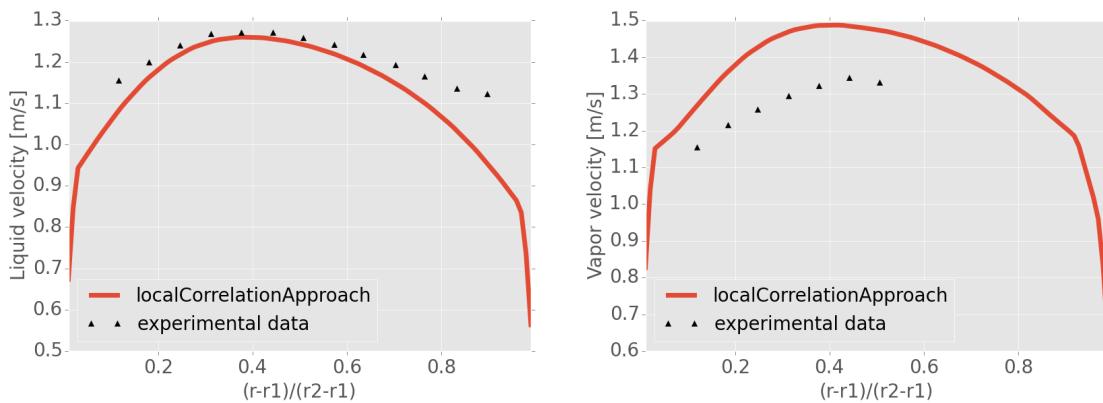
(a) Water velocity for Lee case no 3.

(b) Vapor velocity for Lee case no 3.
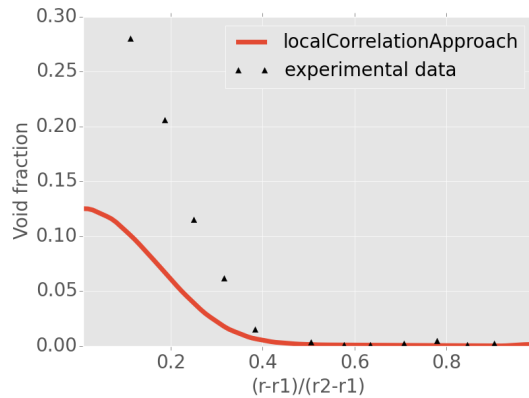
(c) Void fraction distribution for Lee case no 3.

Figure 5.17: Comparison of numerical with experimental results. Lee No. 3.

Recalculation of Experiment with High Heat Fluxes

The next step in the validation of the two-phase flow solver is the recalculation of two different experiments with heat fluxes in the vicinity of the critical heat flux. The first experiment is a simple tube geometry and the second a geometry which is representative for a lower head of a reactor pressure vessel. No experimental data for the void fractions are available for these two experiments, but only the heat flux, that was reported in the experiment as the critical heat flux. The procedure for the recalculation will be, to simulate the same case with heat fluxes, that are lower and higher as the reported critical heat flux.

Russian Academy of Science - 8 mm Tube

The Russian Academy of science conducted experiments in tubes with 8 mm diameter and water as the working fluid. The data of the experiments is assembled in the book by Collier and Thome (1996), which also served as a basis for the data used in this study. The test section has a length of 1 m and a pressure of 15.7 MPa has been used. The mass flux is 2000 $\frac{kg}{m^2 s}$ and the inlet temperature is 510.13 K, which results in a subcooling of 108.85 K. The boundary conditions for the 8 mm tube experiment are summarized in table 5.10.

Table 5.10: Boundary conditions for CHF experiments in 8 mm tube.

Parameter	Value
Diameter	8 mm
Length	1 m
Pressure	15.7 MPa
G_A	2000 $\frac{kg}{m^2 s}$
T_{inlet}	510.13 K
q	2.45 $\frac{MW}{m^2}$
x_{out}	0

Numerical Setup - 8 mm Tube

As in the previous simulations, a two-dimensional 5 degree wedge geometry was used in this case. The geometry was enlarged with a 0.5 m long inlet and a 0.5 m long outlet section to avoid re-circulation at the boundaries. The mesh consists of 15 cells in radial and 400 cells in axial direction. The mesh sensitivity study was performed with meshes with 10, 15 and 20 cells in radial direction and 200 and 400 cells in axial direction. While the refinement in axial direction had no influence on the result, meshes with 20 and more cells in radial direction lead to unstable simulations and could not be used in this case. The time step size was set 0.0001 seconds. The bubble diameter is modeled with the interfacial area transport equation. The interfacial forces follow the base model, as described in table 5.4, with the exception that the wall force was omitted in this case, as suggested by Vyskocil and Macek (2012). The goal of these simulations is to study the effect of wall heat flux on the maximum local void fraction. The critical heat flux is known from the experiment to be 2.45 $\frac{MW}{m^2}$. 4 different simulations have been perform with exactly the same set up and boundary conditions, but with different heat fluxes. The heat fluxes investigated were 80 % CHF, 90 % CHF, 100 % CHF and 105 % CHF.

Numerical Results - 8 mm Tube

Results of the simulations are assembled in figure 5.18. Here, the maximum local, near wall, void fraction found in each simulation is plotted against its fraction of CHF. Additionally, the near wall critical void of 82 %, as used in the CHF model by Weisman and Pei (1983)), is plotted as a reference line. While the maximum void fraction at 80 % CHF is around

0.2 and for 90 % CHF around 0.6, for 100 %CHF a maximum void fraction of 0.81 can be found. When the heat flux is further increased to 105 % CHF a maximum void fraction of 0.86 was found. These findings are in accordance to previous simulations by Macek and Vyskocil (2008) done with the NEPTUNE code, which uses a RPI-type (see Kurul and Podowski (1991)) boiling model.
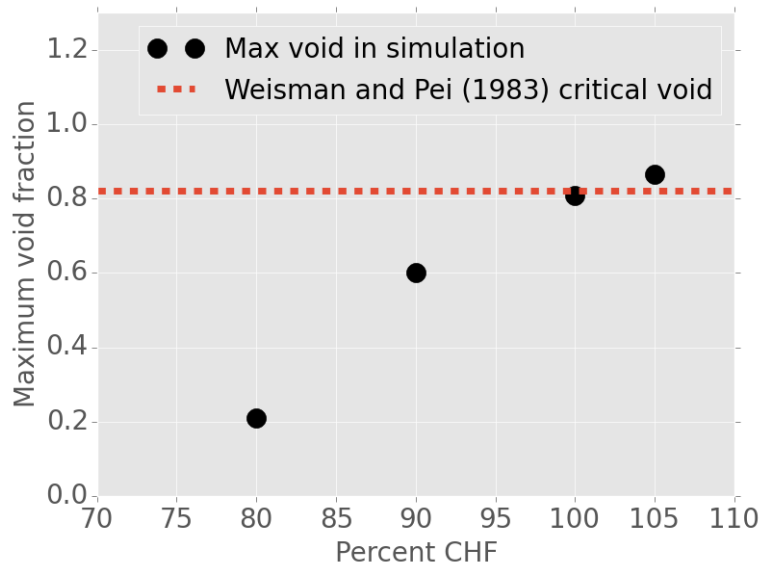

Figure 5.18: Maximum local, near wall void fraction in the simulation domain over wall heat flux for 8 mm tube.

Experiments by Park et al. (2013)

Park et al. (2013) conducted experiments with water in a curved channel to investigate the critical heat flux. The geometry is a 90 degree, 2-dimensional slice-curve, with three different radii, 0.15 m , 0.25 m and 0.5 m. These radii correspond to a scaling of 1/16 th , 1/10 th and 1/5 th of a reactor pressure vessel of type APR1400. A radius of 0.5 m was chosen for the recalculation, as this is the radius closest to the real reactor pressure vessel geometry. Subcooled water enters at the bottom of the 2D curve (horizontally) and is heated up non-uniformly from the inner surface of the slice. The water leaves the test section vertically at the top. The test section has a width of 30 *mm* and a height of 60 *mm*. The experimental setup is shown in figure 5.19.
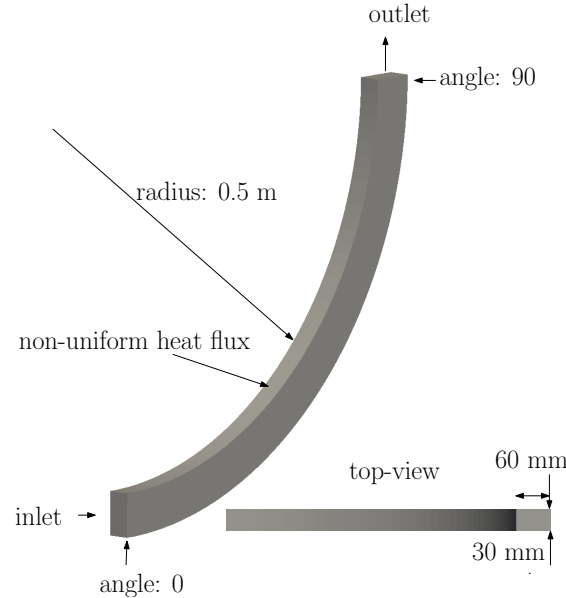
Figure 5.19: Experimental setup for the experiments by Park et al. (2013).

The pressure is atmospheric pressure and an inlet subcooling of 2 K was used. The inlet mass flux is 400 $\frac{kg}{m^2 s}$. The wall heat flux is applied on the inner side of the curve and divided into four zones (see figure 5.20). Each zone has a different heat flux with the heat flux getting larger in direction of the angle of the curve, starting from the bottom. The distribution of the heat flux was chosen to be as close as possible to the heat flux distribution that is expected to occur under a severe accident scenario in a reactor pressure vessel. The highest heat flux is expected to occur in a small region at about 90 degrees where the metallic layer of the molten material is being formed on top of an oxide pool. The CHF in this region measured by Park et al. (2013) was at 1.65 $\frac{MW}{m^2}$ for the previously mentioned boundary conditions. A summary of the boundary conditions is given in table 5.11.

Table 5.11: Boundary conditions for CHF experiments by Park et al. (2013)

Parameter	Value
Radius	0.5 m
T_{sub}	2 K
Pressure	1 bar
G_A	400 $\frac{kg}{m^2 s}$
CHF	1.65 $\frac{MW}{m^2}$
q	non uniform. see figure 5.20
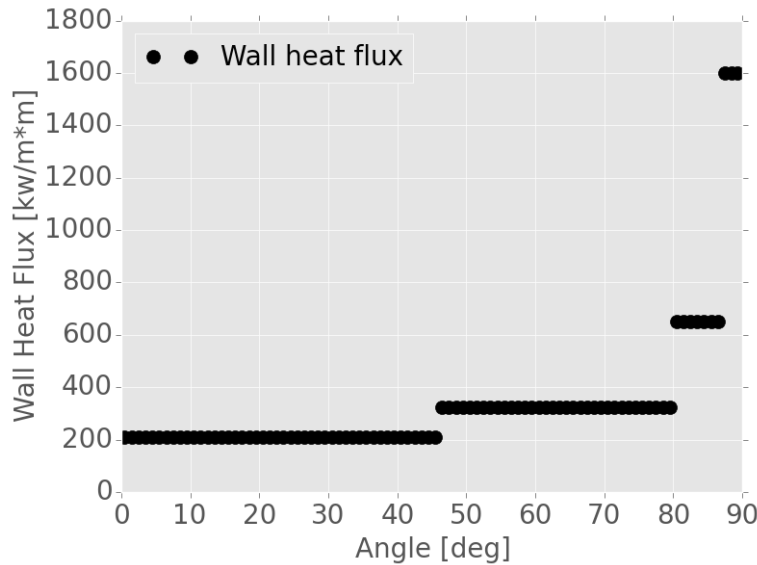
Figure 5.20: Wall heat flux along the curved channel for experiments by Park et al. (2013).

Numerical setup for experiments by Park et al. (2013)

The curved channel was simulated as a 2-dimensional curved channel (see figure 5.21 for the mesh setup). The 90 degree curve was extended by 0.1 m at the inlet in horizontal direction and 0.1 m at the outlet in vertical direction, to ensure that no flow re-circulation is occurring at the inlet and outlet. After a mesh sensitivity study (see 5.22 for results on radial void fraction) a mesh with 25 cells in radial direction and 90 cells along the inclination angle has been used for the subsequent simulations. The interfacial area concentration is again obtained from the transport equation. The setup of interfacial forces is the same, as for the recalculations of the 8 mm tube shown before (all interfacial models as in table 5.4, but no wall force model). The methodology used to study the effect of wall heat flux on the local void fraction is similar as previously described in chapter 5.2.2. The experimental CHF value is known and several simulations are performed with heat fluxes varying from 60 % CHF to 105 % CHF. Only the heat flux in the last heating zone, the *focusing effect zone*, has been adjusted while the other heat fluxes were left all the same for all simulations. A steady-state has been reached after about 10 s for all simulations.

Numerical Results for experiments by Park et al. (2013)

Figure 5.23 shows the void fraction distribution of the 100 % CHF simulation. As expected, the maximum void fraction can be found at around 90 degree. It is also interesting to see that the flow channel is divided into a region with high void fraction near the heater and a relatively large portion of the channel is pure liquid flow, despite the low subcooling of just 2 K. This phenomena is in accordance with observations reported by Park et al. (2013).

A comparison of local void fractions along the heater wall for different heat fluxes is given in figure 5.24. A similar situation to the recalculation of the previous experiment can be observed. At 60 % CHF in the last region a maximum void fraction of 0.62 is reached. When increased to 80 %, the maximum void fraction is 0.74. At 90 % CHF, the maximum void fraction at the steady state is 0.79, and for 100 % CHF 0.81. The differences between the maximum void fractions between 90 and 105 % CHF are much smaller than for the previous case.

Figure 5.21: 2D mesh for the simulation of experiments by Park et al. (2013).
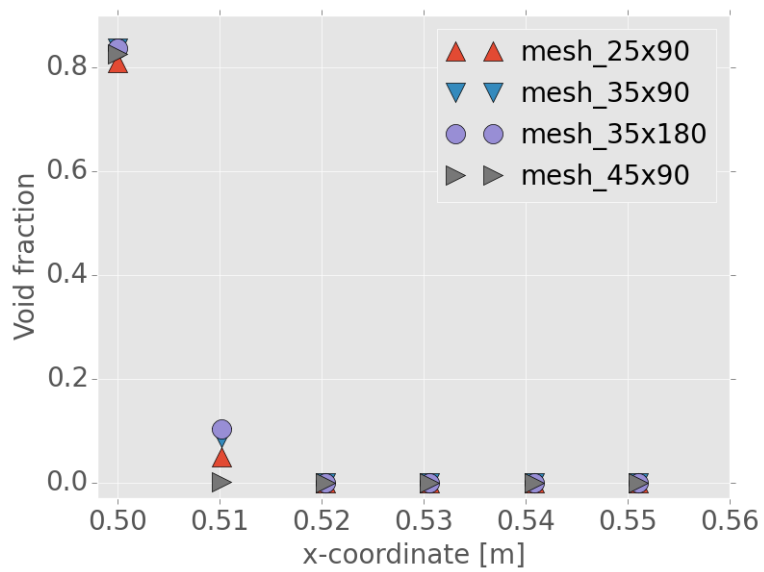
Figure 5.22: Mesh study: Radial void fraction profiles at the location with maximum void for different mesh sizes.
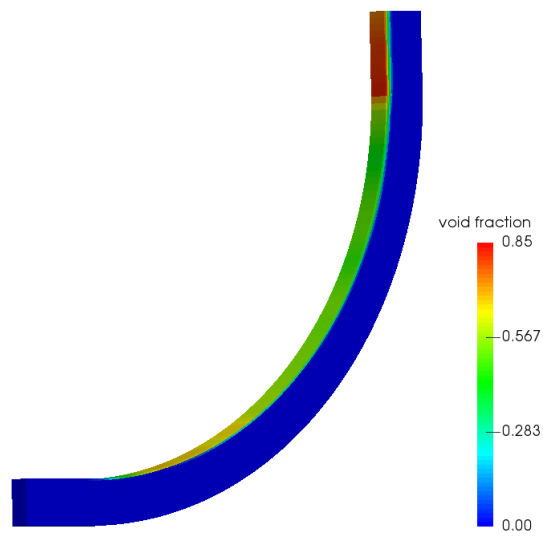
Figure 5.23: Simulation result for void fraction distribution, in case of critical heat flux, for experiment by Park et al. (2013).
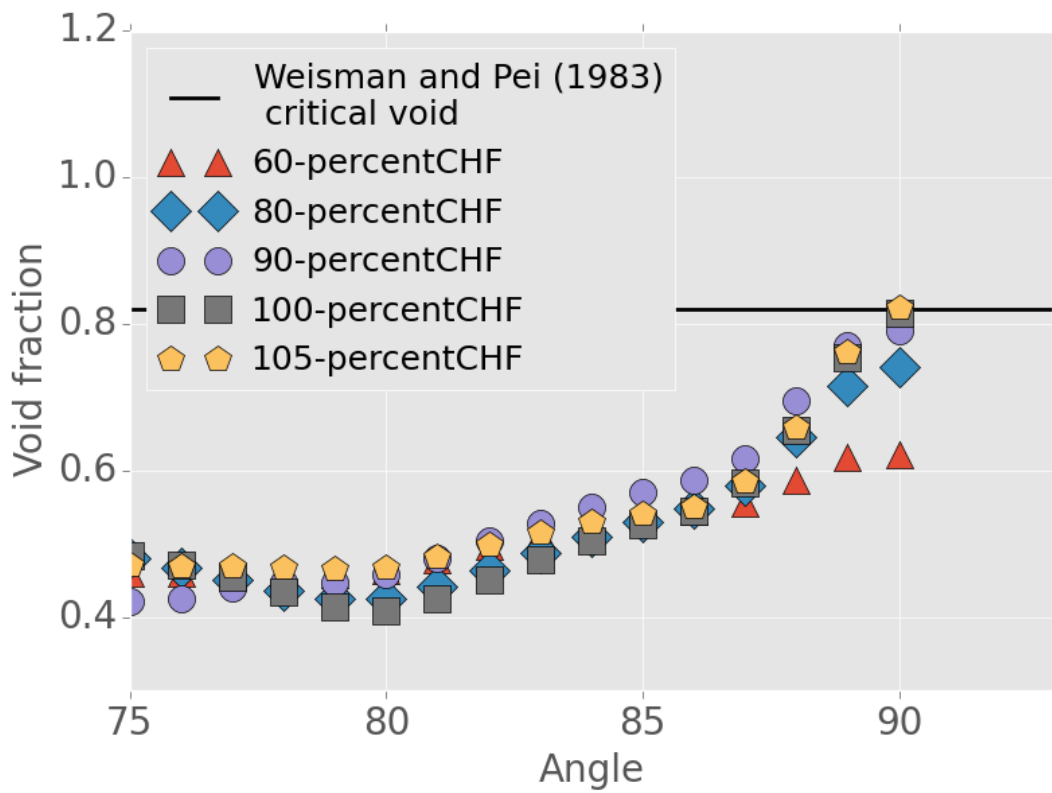

Figure 5.24: Near wall void fractions at different wall heat flux levels.

5.3 Summary of the validation

The validation of the numerical tools to be applied in the following chapter has shown that the simulation of melting and solidification combined with convection is working as expected. To validate this part of the solver, an experimental setup, involving the melting of gallium in a box has been recalculated. The agreement of the simulation results with the experimental data was acceptable.

The next part of the validation was focused on the simulation of two-phase flows with and without heat transfer. As a first step, an experiment without heat transfer has been recalculated to make sure that the implementations regarding the two-phase flow wall heat transfer and phase change do not affect the results in an isothermal environment. A secondary goal of the recalculation of these experiments was to asses the influence of the modeling of interfacial area concentration and the drag force. Both models were found to have a small influence on the results, although in case of the drag model the Ishii-Zuber model produced results that were closer to the experimental data. For this reason the Ishii-Zuber model was selected as the default drag model for the following simulations. The overall agreement with the experimental data for the velocities was excellent, while the void fraction distributions showed larger differences. The possible reasons for these differences can be found in the uncertainty of the inlet distribution of the void fraction, as here only an integral value is available from the experiment. Another possible reason could be an under-estimation of the lateral force by the lift force model.

The recalculation of three experiments of subcooled nucleate flow boiling showed that the effects of evaporation on a superheated wall and the condensation of bubbles in subcooled liquid can be reproduced by the models either developed or implemented during this study. The comparison of wall temperatures, between simulation results and experimental data, showed that the wall temperatures are slightly under-predicted by the wall heat transfer model. Cross-section averaged void fractions were reproduced well by the simulation. Larger differences were found in the comparison of local void fraction distributions for the recalculation of a heated annular geometry. While good agreement, for the void fraction profile, was achieved for a case with low mass flux, the high mass flux case showed large deviations of experimental data and simulation results.

The recalculation of two experiments with high heat fluxes were performed to asses the behavior of the solver in case of high heat fluxes and as a possible result, high local void fractions. No experimental data regarding the void fractions were available for these experiments, but only the value of the critical heat flux. The solver was capable to simulate local void fractions of over 80 %. When scaling the heat flux down and up, in relation to the experimentally determined critical heat flux, a maximum local void fraction of about 80 % was simulated in both cases. This observation is in accordance with simulations performed by Vyskocil and Macek (2012). As only two cases were simulated with high heat fluxes in this study, this is not meant to be an assessment of critical heat flux, but rather a test of the solver under high heat flux conditions.

6. Modeling of a Prototypical IVR Cooling System

The application of previously derived, implemented and verified or validated models to a real world example is the major goal of this chapter. This work will be done in two main steps. Step number one is the comparison of simulation results with lumped parameter calculations done by Esmaili and Khatib (2004) and Zhang et al. (2010) of the AP 1000 reactor pressure vessel in case of a severe accident involving a complete core melt down. Step number two is the extension of this simulation by employing the coupled two-phase flow solver developed in this study to test the structural integrity of the AP 1000 vessel under two-phase flow natural circulation conditions. As no reference data (experimental or numerical) for this kind of simulation is available, a parameter study will be performed to investigate important parameters purely base on simulations results. The geometrical dimensions of the cooling flow path should be seen as an academic or prototypical example as no exact drawings of this configuration is available in the public literature.

6.1 Code to Code Comparison with Esmaili and Khatib (2004) and Zhang et al. (2010)

Esmaili and Khatib (2004) performed an extensive study of the integrity of the AP 1000 reactor pressure vessel under low pressure severe accident conditions. The main assumptions of the authors were two different melt pool configurations after a core melt down and partially relocation of the molten material to the lower head of the reactor pressure vessel. Configuration I is made up of a ceramic pool with a metallic layer on top. Configuration II on the other hand has another heavy metallic layer on the bottom underneath the ceramic pool. The authors conclude that configuration I has a higher probability to exceed the critical heat flux and is thus chosen for this study as the more relevant case. Zhang et al. (2010) used the same boundary conditions and applied a similar lumped parameter code to the case. These results will also be included in the comparison.

6.1.1 Material Properties and Boundary Conditions

Major uncertainties include the mass of molten and relocated uranium oxide UO_2, the decay heat and the fraction of oxidized zirconium. Another decisive factor, which is not known a priori, is the mass of steel in the top layer. Esmaili and Khatib (2004) developed uncertainty distributions on these parameters mainly based on MELCOR and RELAP5

Table 6.1: Material properties of pure materials

Property	Value	Property	Value
ρ_{Zr}	$6130 \ \frac{kg}{m^3}$	λ_{Zr}	$36 \ \frac{W}{mK}$
ρ_U	$17500 \ \frac{kg}{m^3}$	λ_U	$49 \ \frac{W}{mK}$
ρ_{ZrO_2}	$5990 \ \frac{kg}{m^3}$	λ_{ZrO_2}	$3.25 \ \frac{W}{mK}$
ρ_{UO_2}	$8740 \ \frac{kg}{m^3}$	λ_{UO_2}	$5.6 \ \frac{W}{mK}$
ρ_{SS}	$7020 \ \frac{kg}{m^3}$	λ_{SS}	$24.1 \frac{W}{mK}$
cp_{Zr}	$458 \ \frac{J}{KgK}$	β_U	$8.61 * 10^{-4} \ \frac{1}{K}$
cp_U	$157 \ \frac{J}{KgK}$	β_{Zr}	$0.54 * 10^{-4} \ \frac{1}{K}$
cp_{ZrO_2}	$815 \ \frac{J}{KgK}$	β_{SS}	$1.2 * 10^{-4} \ \frac{1}{K}$
cp_{UO_2}	$485 \ \frac{J}{KgK}$		
cp_{SS}	$835 \ \frac{J}{KgK}$		

calculations of severe accident progressions. For this study, the case with the highest probability has been selected for comparison referred to as the *base case*.

The decay heat density for this case is given as 2.1 $\frac{MW}{m^3}$, the uranium oxide mass as 66 266 kg, the zirconium oxide mass as 6 211 kg, the zirconium mass as 12 714 kg and the mass of the steel as 37 376 kg. Decay heat is assumed to be only present in the ceramic pool.

The evaluation of material properties is done in the same way as by Esmaili and Khatib (2004) to keep the simulations comparable. This method of obtaining the material properties was originally published by Rempe et al. (1997). The values for the pure materials needed for this method are given in table 6.1.

Density

The density for the metallic layer is calculated as

$$\rho_{metallicLayer} = f_{v-Zr} \cdot \rho_{Zr} + f_{v-SS} \cdot \rho_{SS} + f_{v-U} \cdot \rho_U. \tag{6.1}$$

And for the ceramic pool accordingly

$$\rho_{ceramicPool} = f_{v-Zr} \cdot \rho_{Zr} + f_{v-SS} \cdot \rho_{SS} + f_{v-U} \cdot \rho_U. \tag{6.2}$$

With f_v being the volume fraction of the specified pure material.

Thermal conductivity

The thermal conductivity for the metallic layer is calculated depending on the mass fraction f_M of the respective pure material according to

$$\lambda metallicLayer = f_{M-Zr} \cdot \lambda_{Zr} + f_{M-SS} \cdot \lambda_{SS} - 0.72 f_{M-Zr} \cdot f_{M-SS} |\lambda_{Zr} - \lambda_{SS}|. \tag{6.3}$$

For the ceramic pool the thermal conductivity is calculated based on the mole fraction f_N of the pure materials as

$$\lambda ceramicPool = f_{N-UO_2} \cdot \lambda_{UO_2} + f_{N-ZrO_2} \cdot \lambda_{ZrO_2} - 0.4 f_{N-UO_2} \cdot f_{N-ZrO_2}. \tag{6.4}$$

Table 6.2: Resulting averaged material properties for ceramic pool and metallic layer.

Property	Value
$\rho_{metallicLayer}$	$6756.67 \ \frac{kg}{m^3}$
$\rho_{ceramicPool}$	$8409.15 \ \frac{kg}{m^3}$
$cp_{metallicLayer}$	$733.8 \ \frac{K}{kgK}$
$cp_{ceramicPool}$	$513.29 \ \frac{K}{kgK}$
$\lambda_{metallicLayer}$	$25.61 \ \frac{W}{mK}$
$\lambda_{ceramicPool}$	$5.14 \ \frac{W}{mK}$
$\beta_{metallicLayer}$	$1.0 * 10^{-4} \ \frac{1}{K}$
$\beta_{ceramicPool}$	$1.05 * 10^{-4} \ \frac{1}{K}$
$Pr_{metallicLayer}$	0.1
$Pr_{ceramicPool}$	0.5

Specific Heat Capacity

The specific heat capacity of the the metallic layer and the ceramic pool are both calculated based on the mass fractions of the pure materials as

$$Cp_{metallicLayer} = f_{M-Zr} \cdot Cp_{Zr} + f_{M-SS} \cdot Cp_{SS} + f_{M-U} \cdot Cp_U \tag{6.5}$$

and

$$Cp_{ceramicPool} = f_{M-UO_2} \cdot Cp_{UO_2} + f_{M-ZrO_2} \cdot Cp_{ZrO_2}. \tag{6.6}$$

Thermal Expansion Coefficient

The volume fraction is used to calculate the thermal expansion coefficient of the metallic layer

$$\beta_{metallicLayer} = f_{v-Zr} \cdot \beta_{Zr} + f_{v-SS} \cdot \beta_{SS} + f_{v-U} \cdot \beta_U. \tag{6.7}$$

While for the ceramic pool, a constant value of $1.05 * 10^{-4} \ \frac{1}{K}$ is used for the thermal expansion coefficient.

Dynamic Viscosity

The dynamic densities for the metallic layer and the ceramic pool are calculated based on exponential functions as

$$\eta_{metallicLayer} = 1.1081 * 10^{-4} exp(\frac{5776}{T_{bulk}}) \tag{6.8}$$

and

$$\eta_{ceramicPool} = 1.5868 * 10^{-4} exp(\frac{10430}{T_{maxPool}}). \tag{6.9}$$

The averaged material properties, as they are used in the following simulations, are summarized in table 6.2. While most material properties of the metallic layer and the ceramic pool are similar, the most noticeable difference can be seen in the thermal conductivity ($25.61 \ \frac{W}{mK}$ for the metallic layer and $5.14 \ \frac{W}{mK}$ for the ceramic pool). This difference in thermal conductivity causes the focusing effect and represents the biggest threat to the integrity of the reactor pressure vessel under low pressure severe accident scenarios.

The resulting volume of the ceramic pool with internal heat source becomes $8.61 \ m^3$ and for the metallic layer $7.56 \ m^3$. The starting angle of the metallic layer is therefore 70.35 degrees with a total height of 0.627 m. The inner radius of the reactor pressure vessel is assumed to be 2 m with an initial wall thickness of 0.15 m.
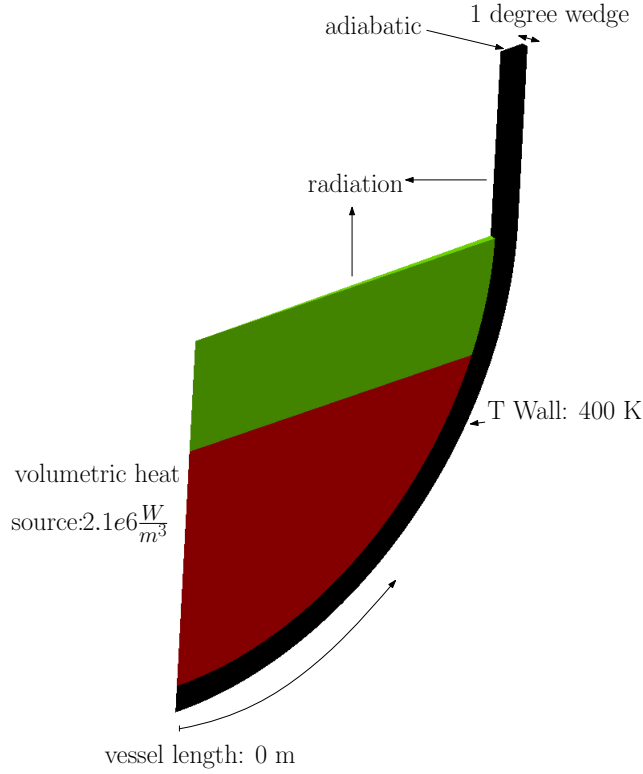
Figure 6.1: Schematic setup of 2D multiregion simulation domain used for code to code comparison. Red: ceramic pool, green: metallic layer, black: RPV wall.

6.1.2 Numerical Setup

For the code to code comparison, all volumes are closed with no inlets or outlet present. The complete geometry is approximated as a 1 degree wedge (see figure 6.1). The ceramic pool (red), the metallic layer (green) and the reactor pressure vessel wall (black) are discretized with separate meshes composed of hexahedral cells. The coupling between the separate meshes, from now on called *regions*, is realized by incorporating the newly developed solver into the OpenFOAM multRegion framework. Here, the different meshes are assigned to different solvers and become coupled through a shared energy boundary condition. The limitation of this approach is that the regions cannot inter-penetrate each other or change their shape. Phase change from liquid to solid and vise versa is only possible within each predefined region.

At the top of the metallic layer and on the free inside area of the reactor pressure vessel, a gray body radiation boundary condition has been applied. As no such boundary condition is available, it has been implemented as

$$\frac{\partial T}{\partial x} = -\frac{\epsilon_{rad}\sigma}{\lambda_{eff}}(T^4 - T_{inf}^4) \tag{6.10}$$

into the OpenFOAM library. σ is the Stefan-Boltzmann constant and T the temperature in the current boundary cell. The emissivity ϵ_{rad} is set to 0.4 in accordance to Esmaili and Khatib (2004) and the infinite temperature T_{inf} to 950 K.

The top cut-off part of the reactor pressure vessel wall was approximated with an adiabatic boundary condition, while the outside of the RPV wall has been set to a fixed temperature of 400 K, again to match the boundary conditions applied by Esmaili and Khatib (2004) in their lumped parameter code.
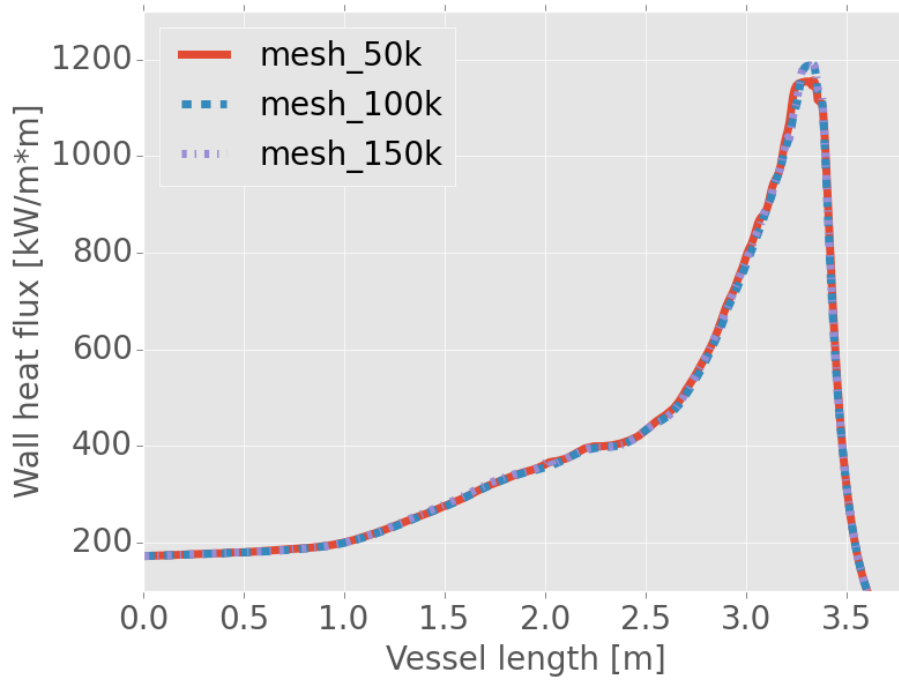
Figure 6.2: Mesh Study of core, metallic layer and vessel wall.

A mesh sensitivity study has been performed with meshes that consist of 50000 cells, 100000 cells and 150000 cells. As a result of the mesh study, the wall heat flux on the outer RPV wall is plotted in figure 6.2 as the main parameter of interest. It can be seen that a reasonable wall heat flux profile is predicted by the simulation, as the general shape is similar to the one used in the experiments by Park et al. (2013) that have been recalculated in the previous chapter. The difference in wall heat flux is small between the meshes, but the 50k mesh predicts a slightly smaller heat flux peak than the other two meshes. As the heat fluxes of these meshes are identical, the mesh with 100000 cells has been selected for all the upcoming simulations for the regions ceramic pool, metallic layer and RPV wall.

6.1.3 Numerical Results

The crust thickness in the ceramic pool, the remaining thickness of solid material in the RPV wall as well as the heat flux on the outer RPV wall are compared to the predictions by Esmaili and Khatib (2004) and Zhang et al. (2010). Both codes use a lumped parameter approach while a CFD approach has been applied in this study to the same problem. The problem size, internal heat source, outer wall temperature and material properties are the same for all codes.

Crust Thickness

A portion of molten core material is expected to solidify in the lower part of the ceramic pool and form a solid crust. The formation of this crust has a great influence on the heat transfer to the enclosing RPV wall, as the heat can only be removed through heat conduction in areas, where a crust has been formed, and not through convection as in the other areas, where liquid material is still present. The comparison of crust thickness to simulation results of the other two codes is presented in figure 6.4 (a). The counting of the vessel length is started at 0 m from the bottom of the outer RPV wall (see figure 6.1). At this point, the predicted crust thickness of 5 cm is in perfect agreement with
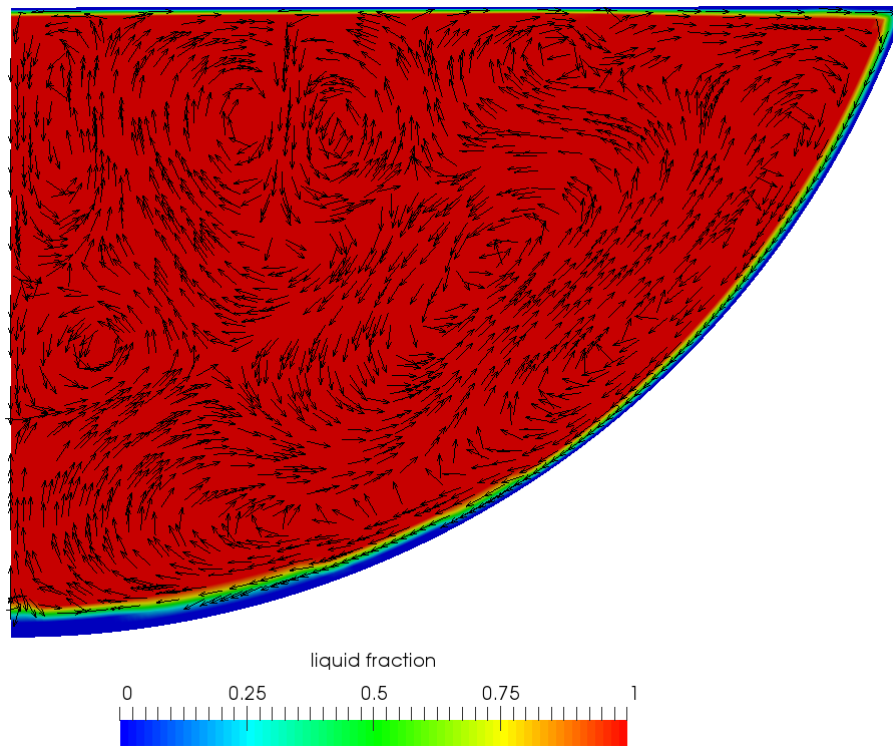
Figure 6.3: Flow pattern in the ceramic pool and crust formation. Blue: solid state, red: liquid state. Colors in between are a result of interpolation.

the simulation result by Esmaili and Khatib (2004). This is remarkable when recalling the total dimension of the ceramic pool with a radius of 2 m and the totally different approaches employed by the different codes to this simulation. The initial crust thickness predicted by Zhang et al. (2010) is slightly thinner at 3.9 cm. When moving along the vessel till about 1.5 m, the results of all simulations are very close. A decrease in crust thickness is predicted unanimously by all three codes.

After 1.5 m, the decrease in all codes slows down, but on a lower level in case of the two lumped parameter codes. In the CFD simulation, a minimum crust thickness of 1.4 cm is retained at all positions. Lumped parameter simulation results by Esmaili and Khatib (2004) show a stagnation between 0.5 and 0.75 cm crust thickness until the crust completely disappears after about 2.75 m. Zhang et al. (2010) predict an even lower stagnation thickness of about 0.25 cm. The difference can be explained by the different modeling approaches. In case of the lumped parameter codes, one-dimensional heat transfer correlations are applied to calculate the heat flux through the core and RPV wall. A correction of the area for the heat flux based on the formation of the crust and ablation of the vessel wall has not been applied in the lumped parameter codes. This effect is implicitly included in the CFD calculations, as a change from solid to liquid also alters the areas for the heat transfer between the phases.

The flow pattern in the pool is shown with the help of velocity vectors in the liquid region of the ceramic pool in figure 6.3. The red area means liquid state and blue area means solid state. Colors in between are a result of interpolation between the two. It is in good agreement with the observations by Theofanous et al. (1997). Three main patterns are visible. The first one is a well mixed upper region characterized by many big vortexes, a stratified high velocity region just above the crust transporting molten material downwards back to the center and a core region with very low velocities (absolute velocities in the core region are shown in figure 6.9).

Wall heat flux

A comparison of the simulated wall heat flux along the outer side of the RPV wall is shown in figure 6.4 (c). At position 0 m, all three simulations agree very well and predict a wall heat flux of about 200 $\frac{kW}{m^2}$. This value is almost constant until 1.1 m, where the results between the lumped parameter simulations and the CFD simulations start to differ. Both lumped parameter simulations predict a steeper increase of wall heat flux until a maximum of 1100 $\frac{kW}{m^2}$ is reached at 2.75 m. The CFD simulation predicts this increase at first at a slower and than later at 2.5 m at a faster pace. The peak values for the wall heat flux are comparable again with 1157 $\frac{kW}{m^2}$ for the CFD simulation and 1100 $\frac{kW}{m^2}$ for the lumped parameter codes. A heat balance has been done for the CFD simulation, to ensure that all the heat created in the core is equal to the heat transferred through the boundaries, because the total heat transferred through the outer wall is less in the CFD case than it is for the lumped parameter codes. One explanation could be that more heat is transferred through radiation in the CFD calculation, than it is the case for the lumped parameter codes. Unfortunately, this information is not given in the respective reports. The thinner predicted crust from 1.1 m to the rest of the wall by the lumped parameter codes could also lead to a higher heat flux in this region. This is consistent with the results shown in figure 6.4. But the question if the thinner crust leads to the higher heat flux or if the higher heat flux leads to the thinner crust remains unsolved.

(a) Thickness of crust in ceramic pool.

(b) Remaining thickness of the RPV wall.

(c) Heat flux distrubution along the outer RPV wall
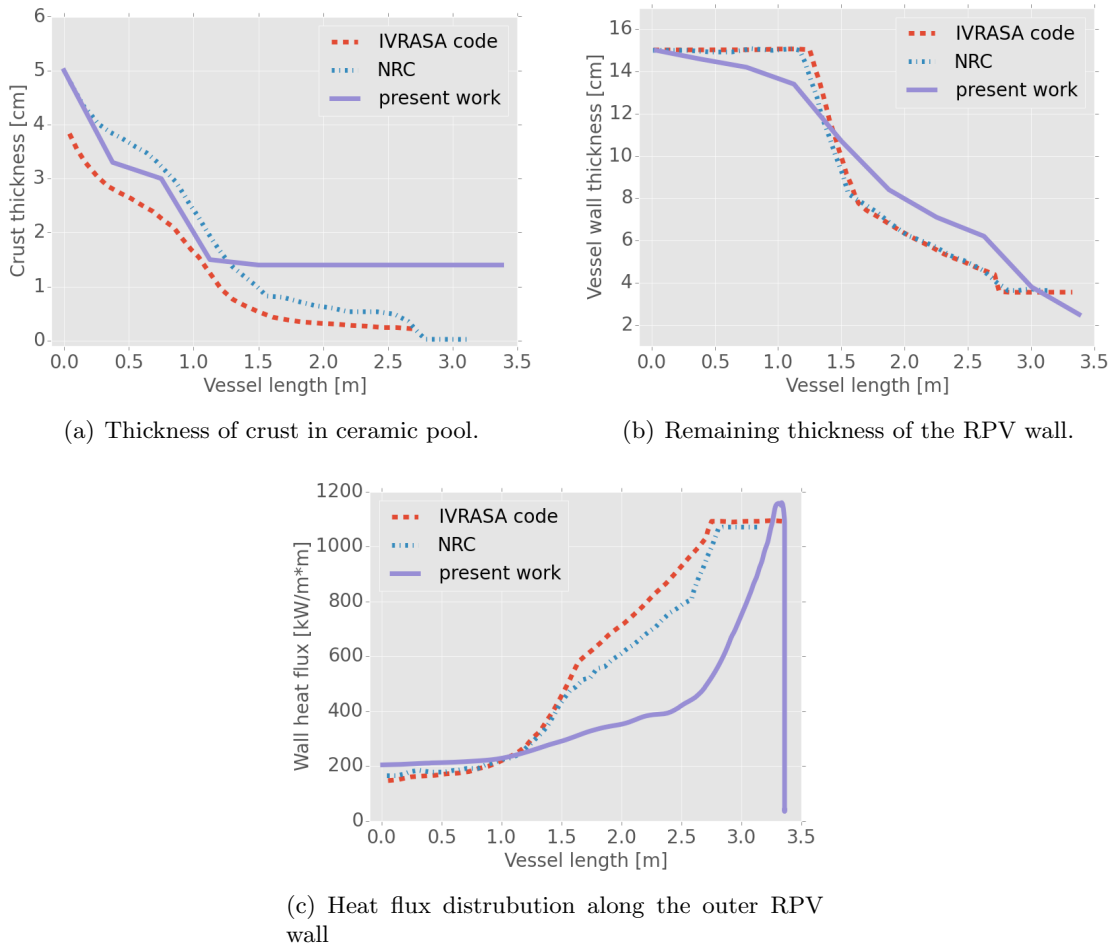
Figure 6.4: Comparison of crust thickness, remaining wall thickness and the wall heat flux distribution with publications by Esmaili and Khatib (2004) (denoted as *NRC*) and Zhang et al. (2010) (denoted as *IVRASA*).
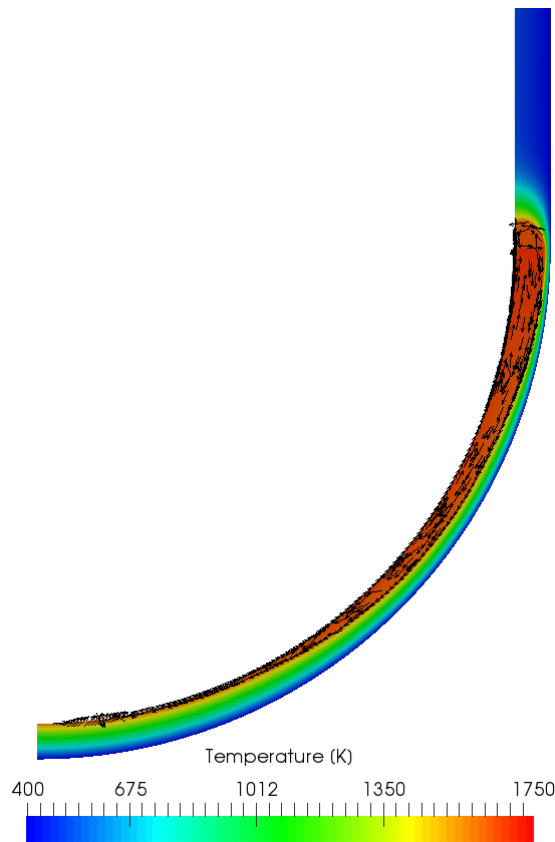
Figure 6.5: Temperature profile in RPV wall and velocity vectors in molten region.

RPV wall thickness

The remaining solid thickness of the reactor pressure vessel wall is presented in figure 6.4 b. The initial thickness of the RPV wall is 15 cm. At the bottom of the RPV, at position 0 m, all codes predict that no melting of the wall has been taken place. While the lumped parameter codes predict to keep the complete solid thickness of the wall till 1.5 m, the CFD simulation predicts a slow decrease of solid thickness which leaves 13.5 cm solid wall at 1 m. The lumped parameter codes predict a sharp decrease in thickness from 1.2 to 1.6 m which is in agreement to their prediction of sharp increase in wall heat flux as well as decrease in crust in this region. The CFD results show a more moderate decrease in remaining wall thickness. Exact agreement of all codes is reached at position 3 m with a wall thickness of 3.6 cm. While this marks the minimum wall thickness for the lumped parameter codes, the result of the CFD simulation show a minimum thickness of just 2.5 cm. The overall differences are remarkably small between the three codes. Slight differences could again be explained by the different modeling approaches; on the one hand a lumped parameter approach, which uses one-dimensional correlations, and on the other hand a CFD calculation, where conservation equations for mass, momentum and energy are solved (with previously described modeling assumptions).

The flow pattern of molten stainless steel in the RPV wall slice and its temperature profile is shown in figure 6.5. One large natural circulation cell is forming in the molten region of the RPV wall. Cao et al. (2015) used a lumped parameter approach in 2 dimensions to study the temperature distribution in the RPV wall under severe accident conditions and found a very similar temperature and melt profile as presented here.

6.1.4 Conclusion Code to Code Benchmark

The comparison with the results produced by lumped parameter codes by Esmaili and Khatib (2004) and Zhang et al. (2010) has shown that CFD results of the present study are very similar to them. Almost no difference in remaining wall thickness, small differences in crust thickness and partially different results for wall heat flux have been observed. This enhances the confidence in the results as two completely different approaches to the simulation of melt pool behavior in the lower head of a RPV lead to similar results. Comparison with experimental data would have been preferable over a code to code comparison, but are not available at the moment. As an advantage over the lumped codes, the CFD results give deeper insight into the flow structures. This helps in understanding the various flow paths and patterns. With this detailed understanding of the flow phenomena, it is possible to optimize the geometries with higher precision. It also helps to reason about the physical correctness of the simulation results in a much more refined way.

6.2 Extension to a passive cooling system

After the comparison with other codes, this last chapter is intended to showcase the capabilities of a coupled multiscale simulation including two-phase flow heat transfer. The previous model of the ceramic pool, metallic layer and reactor pressure vessel wall is extended by a water cooling flow path. A true passive safety design can be achieved, if the integrity of the RPV wall can be ensured under natural circulation cooling conditions. The design of such a system includes a large storage tank of water, which helps to flood a cavity under the RPV. The water will be heated up by the residual heat released in the molten core and transported through the RPV wall to the water. The change in density caused by the temperature difference in the water will be a first driving force for a natural circulation flow. But the heat released by the RPV wall will cause an exceedance of the saturation temperature of the cooling water. The presence of vapor bubbles in the cooling water further drives the natural circulation capabilities and also enhance the heat transfer coefficient from the RPV wall to the cooling water. The produced vapor will be separated from the water at the height of the hot leg of the RPV. The vapor rises further to the containment walls and to other structural material, where it condenses and flows back to the storage tank. The still liquid part of the cooling water will be fed directly to the storage tank. A semi-closed (steam vent to containment is open) natural circulation flow is expected to establish, which is capable to remove enough of the residual heat to keep the RPV wall from melting too far.

6.2.1 Description of the numerical Model

The same mesh (1 degree wedge), material properties and initial conditions that have been used for the code to code benchmark will be used for the following simulations. These regions are extended by a two-phase flow cooling path that is simulated by CFD and STH using the coupling approach as described in chapter 4. The outer wall of the CFD two-fluid region is assumed to be adiabatic. The dimensions and elevations are estimated from the drawings available in Westinghouse (2011). As they are only estimates and no exact geometrical data is available in the public literature, this system can be seen as a prototypical or academic example of an IVR system. A schematic overview of the simulation domain is given in figure 6.6. The red part is the ceramic pool, the green part the metallic layer, the black part the RPV wall, the dark blue part the CFD region of the cooling path and the light blue part the STH region of the cooling path.

As a first step, a mesh sensitivity study of the newly added CFD part of the two-phase flow region has been done. Radial profiles at 90 degrees vessel angle of steam and liquid velocity,
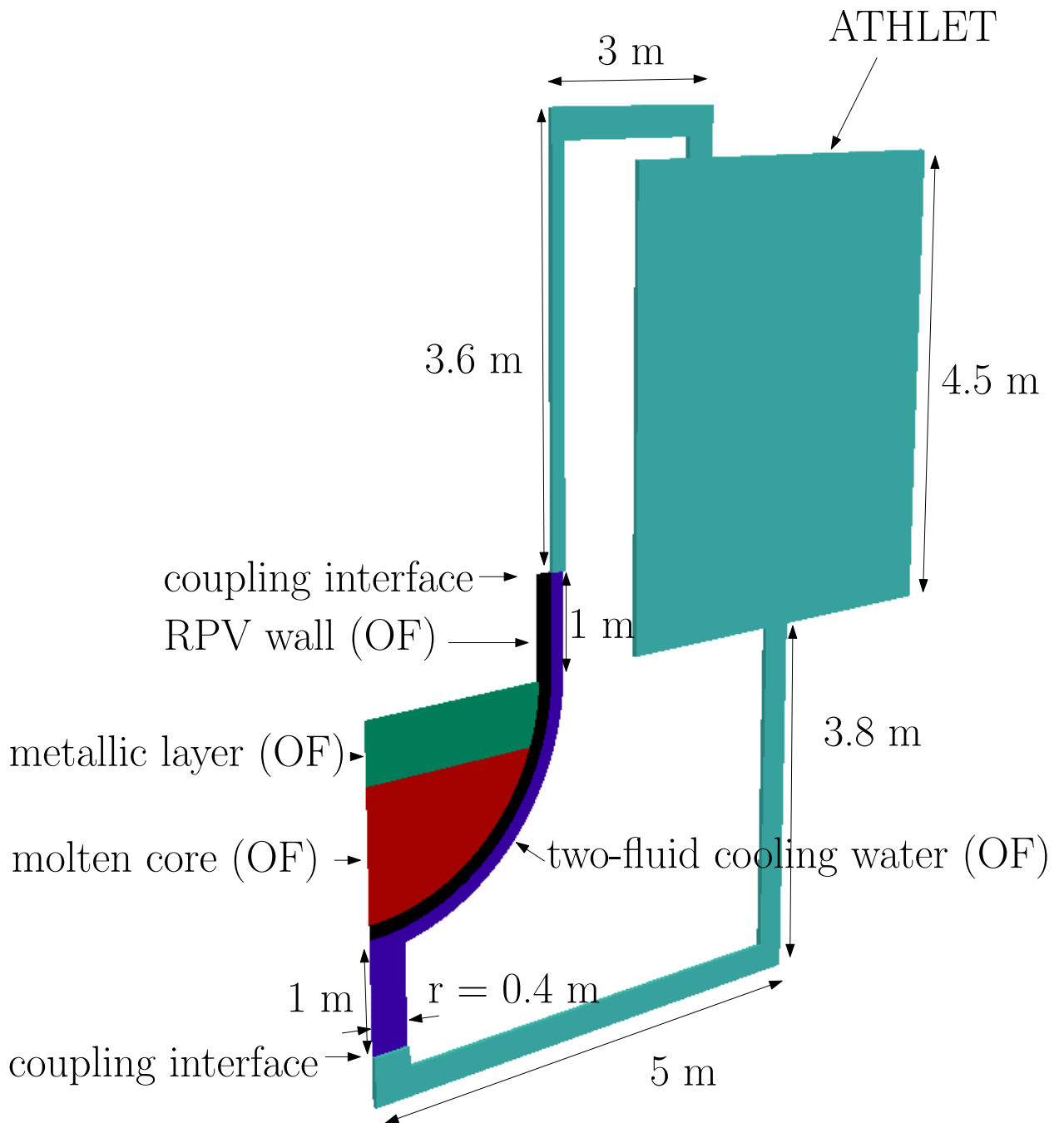
Figure 6.6: Schematic setup of CFD-STH coupled simulation of a passive IVR cooling flow path. Red: ceramic pool, green: metallic layer, black: RPV wall, dark blue: CFD region cooling water, light blue: STH region of cooling water. CFD mesh is a 1 degree wedge.

liquid temperature as well as void fraction are shown in figure 6.7. A mesh independent solution has been reached with 25 cells in radial direction and 143 cells in axial direction. This mesh will be used for the following simulations of the CFD region of the two-phase flow cooling path.

(a) Vapor velocity at 90 degree.

(b) Velocity of liquid water at 90 degree.

(c) Liquid temperature at 90 degree.

(d) Void fraction at 90 degree.
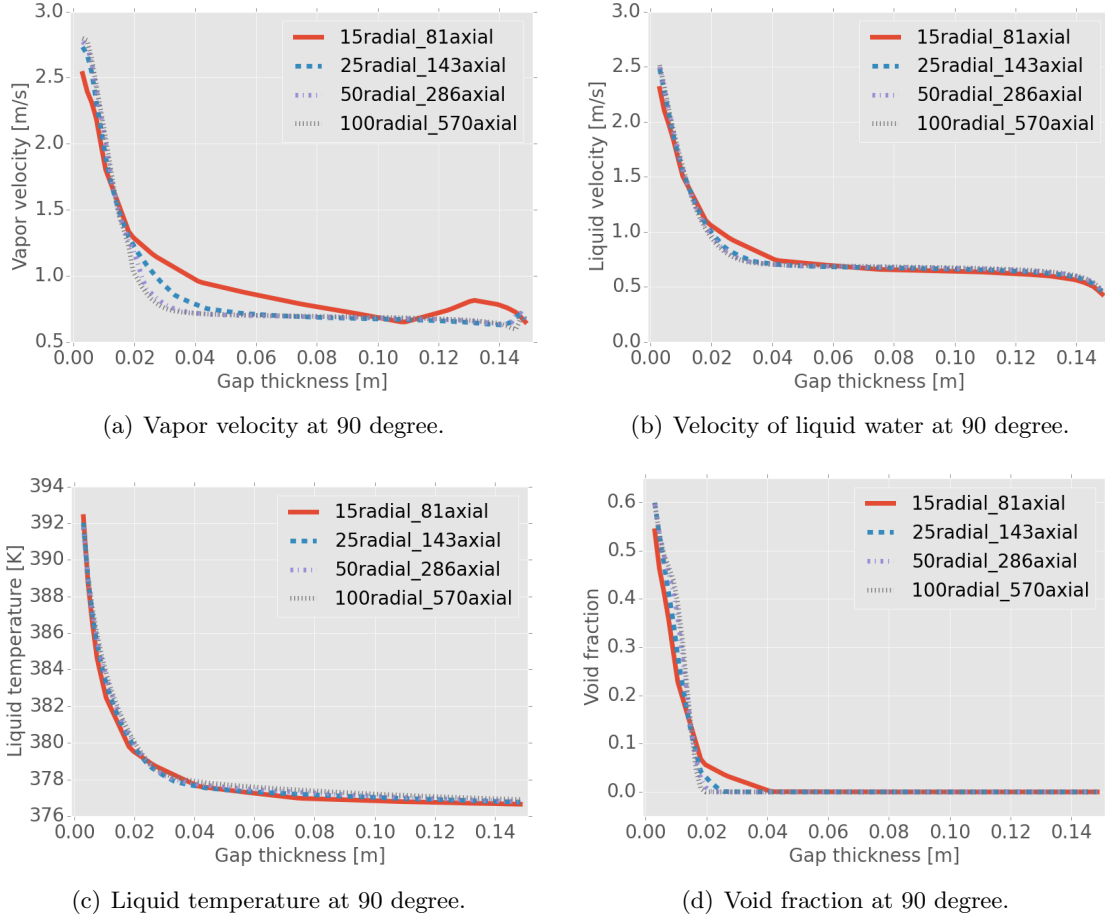
Figure 6.7: Mesh study of two-phase cooling flow path.

The 1D STH model, including its nodilization, is shown in figure 6.8 in detail. It consists of one closed and one open loop. The open loop is the steam vent to the containment, which also serves as the back flow channel of possibly condensed water back to the main loop. Here a constant containment pressure of 2 bar is applied. It is connected to the closed loop at the end of the thermo fluid object (TFO) *riser*. The closed main cooling loop is made up of 4 TFOs (*riser*, *toTank*, *tank*, *toCavity*). The coupling to CFD is realized at the endings of the TFO *toCavity* and *riser*. The number of control volumes in the STH region is 186 and the distribution of the nodalization is shown by the thin lines in figure 6.8. All TFOs have a cylindrical cross section, except for the TFO *riser*. An annular geometry is assumed here, with a flow cross section area of 2.1 m^2. Total height of the tank is 4.5 m with a diameter of 7.5 m, diameter of the pipe connecting the tank to the CFD region is 0.8 m with a length of 9.3 m. Hydraulic diameter for the riser TFO is 0.3 m and its length is 3.6 m. The TFO connecting the riser to the tank is 3.5 m long and has a diameter of 0.8 m. A complete overview of the dimensions of the separate TFOs and their elevations is given in table 6.3. The pressure drop due to friction is calculated with the Colebrook model in all TFOs (see equation 2.83). Additional local pressure losses are not set, as they are not known for this system.
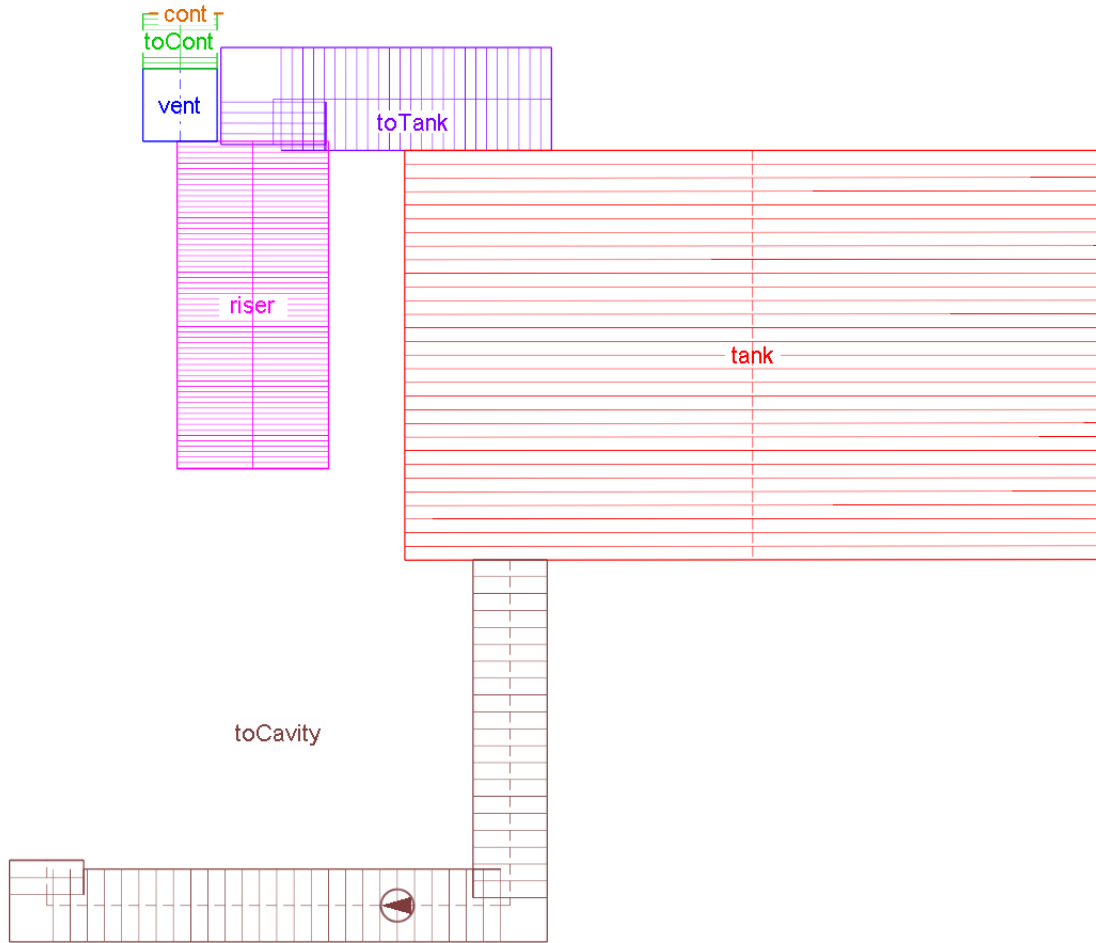
Figure 6.8: STH (ATHLET) model for the coupled simulation of the passive IVR system.

Table 6.3: Properties of the STH (ATHLET) model for IVR coupled simulations.

TFO	Length $[m]$	Hydraulic diameter [m]	Flow cross section $[m^2]$	Start elevation $[m]$	End elevation$[m]$
toCavity	9.3	0.8	0.5	0.0	-3.3
riser	3.6	0.3	2.1	1.0	4.6
toCont	0.6	0.8	0.5	5.4	6.0
toTank	3.5	0.8	0.5	5.0	4.5
tank	4.5	7.5	44.17	4.5	0.0

6.2.2 Influence of Coupling Time Step

The first parameter to investigate is the time step of the coupling information exchange. To save computational time, the wall heat flux from the code to code benchmark is used as a boundary condition on the two-phase cooling flow path, and the ceramic pool, RPV wall and metallic layer are not included in the simulation. Two different coupling time steps, 0.1 s and 0.05 s have been chosen for the investigation. A guaranteed subcooling of 20 K at the inlet of the CFD section was specified by adjusting the wall temperature of the tank accordingly. The resulting steady state mass flow rate due to two-phase natural circulation was 217.5 $\frac{kg}{s}$ for the simulation with a coupling time step of 0.1 s and 218.52 $\frac{kg}{s}$ for the simulation with half the time step size. The maximum void fraction for both cases is 0.65. It can be concluded that the coupling time step size of 0.1 s is small enough, as almost no dependence on the simulation results can be observed. The following simulations will be done with a coupling time step size of 0.1 s.

6.2.3 Influence of Feedback between Ceramic Pool and Cooling Path

The necessity to simulate the ceramic pool, metallic layer and RPV wall together with the cooling flow path is investigated in this section. A lot of computational time can be saved if the cooling path can be simulated separately with a prescribed wall heat flux. The question is whether there is a feedback between the molten pools and the wall and the two-phase flow region. To investigate this, two simulations will be compared. In case 1, all regions are simulated and in case 2, a fixed wall heat flux is applied to the two-phase region of the coupled CFD-STH model. A visualization of the simulation result of case 1 is shown in figure 6.9.

In the metallic top layer, one large circulation cell is formed. This flow pattern is in accordance with the publication by Wang and Cheng (2015), who investigated flow patterns in the metallic layer with a CFD method based on different ratios of layer thickness to vessel radius.

The void fraction distribution is similar to the profiles obtained in chapter 5.2.2. With a high void fraction region near the RPV wall and a subcooled low void fraction region opposite to it.

The steady state mass flow reached in case 1 is 218.07 $\frac{kg}{s}$ and for case 2 217.5 $\frac{kg}{s}$. The maximum void fraction for case 1 is 0.67 and for case 2 a maximum void fraction of 0.65 is obtained. So again, the differences between the two compared simulations are small. An explanation could be given with the rather flat wall temperature profile obtained from subcooled nucleate boiling flow. The heat flux in case no 2 was the result of a fixed temperature boundary condition of 400 K on the outer RPV wall (see figure 6.1). Despite the very non-uniform wall heat flux (see figure 6.4 (c)) the temperature profile obtained from case 1 ranges only from 383 K to 425 K (see figure 6.10). This is caused by the much enhanced heat transfer coefficient at higher void fractions/wall heat fluxes in case of subcooled nucleate flow boiling.

6.2.4 Influence of bubble diameter Modeling Approach

The influence of modeling approach for the bubble diameter on the natural circulation mass flow rate and the maximum void fraction has been studied. One approach was to use a constant bubble diameter of 7 mm and the other was to use a transport equation for the interfacial area concentration as described in chapter 2.3.2. The influence of this parameter is slightly bigger than the parameters studied before, resulting in a difference of natural circulation flow rate of 6 $\frac{kg}{s}$. But the maximum void fraction was the same for both simulations.
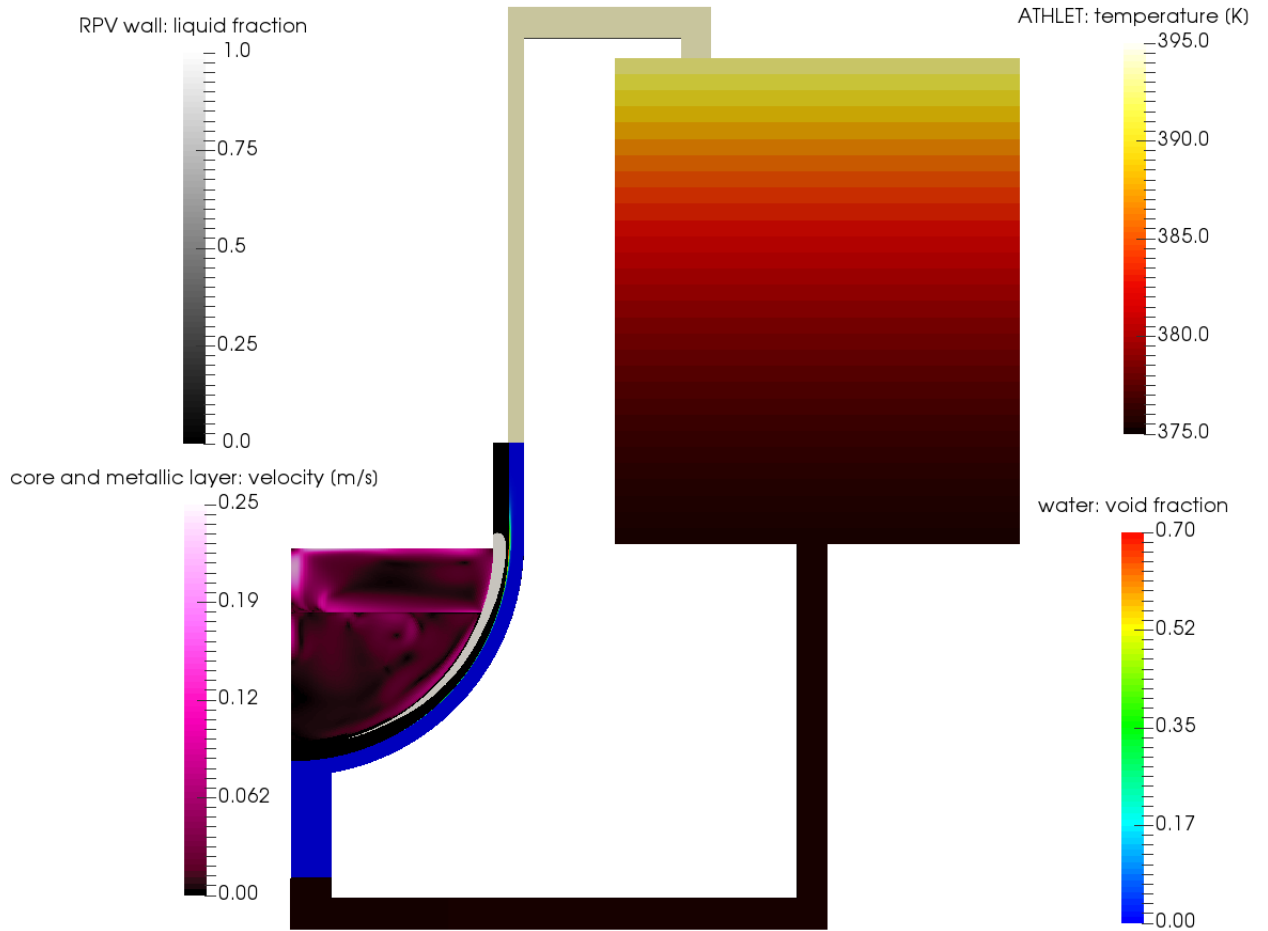
Figure 6.9: Coupled CFD and STH simulation with ceramic pool, metallic layer and RPV wall. Case 1.
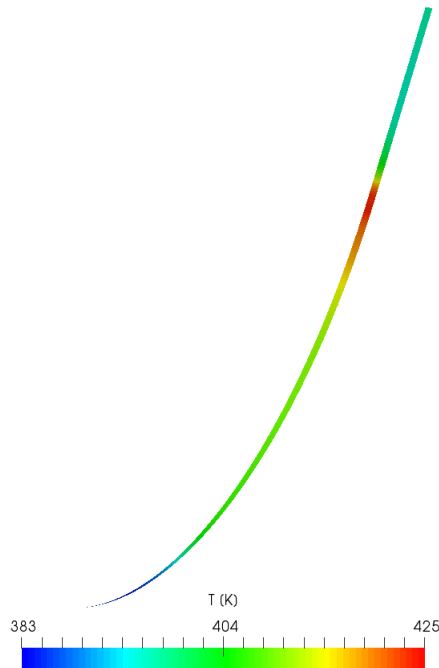
Figure 6.10: Outer wall temperature of RPV wall for coupled CFD - STH simulation with ceramic pool, metallic layer and RPV wall. Case 1.

6.2.5 Influence of Subcooling

The last parameter that is to be studied is the subcooling of the water, as it enters the cavity under the RPV. This parameter is controlled by the wall temperature of the water storage tank. Subcoolings in the range of 5 K to 40 K, with respect to the 2 bar containment pressure, have been investigated. Figure 6.11 shows the mass flow rate sampled before the CFD section (in the last control volume of TFO *toCavity*) and after the CFD section (in the first control volume of TFO *riser*) for subcoolings of 10 K and 15 K for a simulation time of 1000 s. Heavy oscillations are visible for both subcoolings. The two sample points (before and after the CFD region) are plotted together to verify that no mass is added or lost through the coupling under such heavy oscillations. It can be seen that for 10 K subcooling the oscillations start right after reaching an average value of about 300 $\frac{kg}{s}$ and never recover again to a steady state. For 15 K, the simulation looks stable after one small oscillation at the beginning, but starts to enter an unstable state after 360 s. Here the oscillations start with a mass flow excursion to almost 400 $\frac{kg}{s}$, which is recovered after about 100 seconds. The frequency of the oscillations is the same as for the 10 K case, but the amplitude is much lower at the beginning and growing to similar values at the end of the simulation. Simulations with less than 10 K subcooling showed such strong oscillations that a complete simulation was not possible anymore. One explanation could be that the liquid is accelerated so fast in case of the high heat flux, that the suppression of boiling due to the higher mass flux leads to a decrease of evaporation which leads to a decrease in driving force for natural circulation and a lower mass flux. This lower mass flux reduces again the suppression of boiling and enables higher void production which leads to an acceleration of the fluid. Another possibility is evaporation in the bulk flow. If the subcooling below the cavity is small, the bulk flow is almost already saturated when leaving the CFD region. As the hydrostatic pressure decreases with the height of the cooling path, the saturation temperature also decreases, which could lead to the case that the bulk temperature is above the saturation temperature and evaporation in the bulk can occur, which adds more driving force to the natural circulation. This could lead again to a suppression of evaporation and a reduction in mass flow. This would be a typical case

of the so called geysering effect.

To further investigate this phenomena, void fractions for three different elevations are plotted in figure 6.12 (a). The TFO *riser*, which follows the CFD section, is divided into 60 control volumes. Its control volume with the lowest elevation is 1 and the control volume with the highest elevation is 60. In figure 6.12 (a), it can be seen that, at the two lower sampling positions, almost no void is present, although a clear void peak at about 100 s is visible in the highest control volume. With a positive mass flow rate (see figure 6.11 (b)), this void must have been created between control volume 30 and 59. As there is no external heat added to the TFO, this evaporation must be happening due to the lower hydrostatic pressure at elevated positions. The link between the evaporation and the oscillating mass flow can be established with the help of figure 6.12 (b). Here, the mass flow and the void fraction are plotted together over the time. Every peak in void fraction coincides with every peak in mass flow rate. This leads to the conclusion that the void generated due to bulk evaporation accelerates the fluid. With an increased mass flow rate, the bulk temperature is reduced again below its saturation temperature at all elevations in the system and no bulk evaporation can take place. With the lower mass flow rate, higher bulk temperatures can be obtained and the process of bulk evaporation and fluid acceleration starts again.

Subcoolings larger than 15 K on the other hand lead to very stable conditions. Figure 6.13 shows the influence of subcoolings of 20 K, 30 K and 40 K on the mass flow rate and on the maximum void fraction. The maximum mass flow rate of 217.5 $\frac{kg}{s}$ and also the maximum void fraction peak (0.65) is achieved with the lowest subcooling. The higher the subcooling, the lower the mass flow rate and also the maximum void fraction. The main driving force for the flow is the buoyancy force caused by the density difference, because of the presence of vapor bubbles in the liquid. The higher the subcooling, the less cooling water is evaporated and so the driving force for the natural circulation flow is lower. This finding is in accordance with very recent RELAP calculations published by Park et al. (2016).

(a) Unstable mass flow at 10 K subcooling. (b) Unstable mass flow at 15 K subcooling.
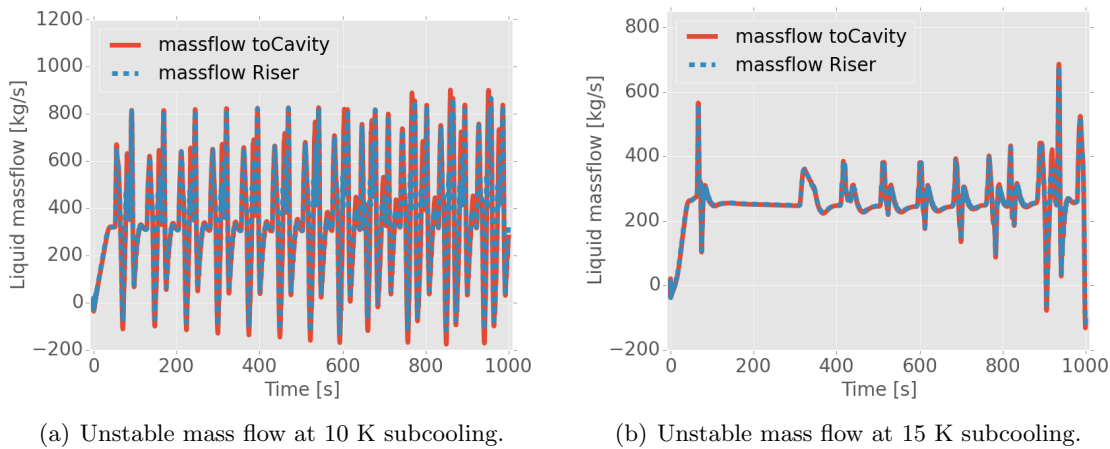
Figure 6.11: Unstable natural circulation behavior at subcoolings below 20 K. Sampling locations are at the last control volume of TFO *toCavity* and the first control volume of TFO *riser*.
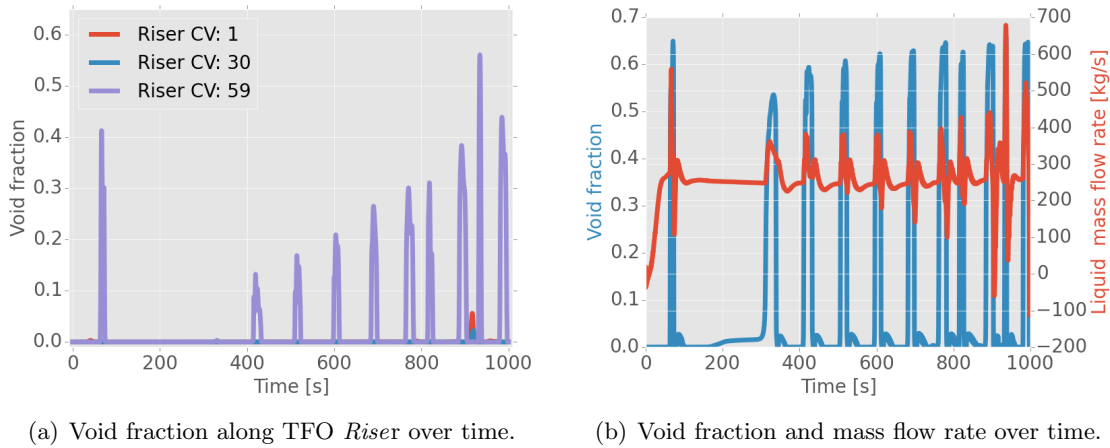
(a) Void fraction along TFO *Riser* over time.

(b) Void fraction and mass flow rate over time.

Figure 6.12: Bulk evaporation and effect on mass flow rate for a subcooling of 15 K.
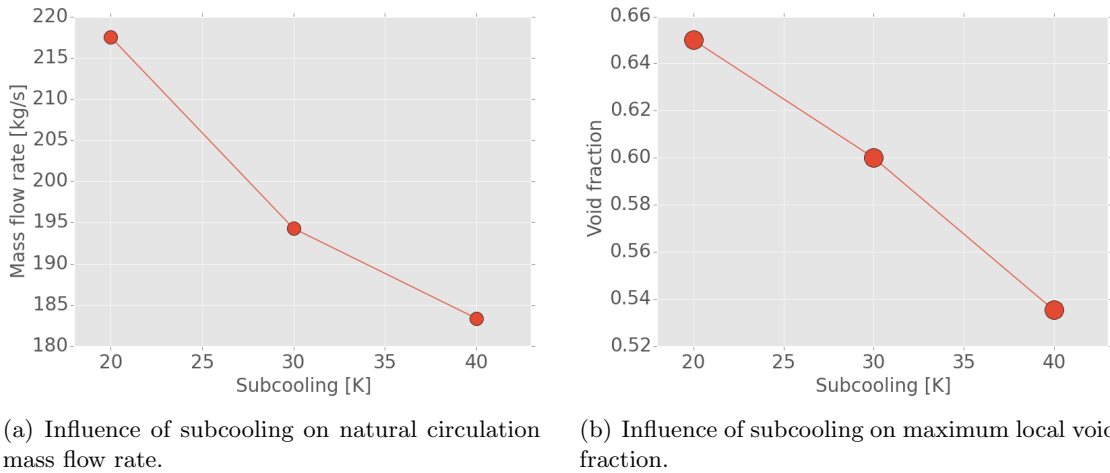
(a) Influence of subcooling on natural circulation mass flow rate.

(b) Influence of subcooling on maximum local void fraction.

Figure 6.13: Influence of subcooling on natural circulation mass flow rate and on the maximum local void fraction.

6.2.6 Conclusion - Simulation of a passive IVR cooling System

Table 6.4 summarizes the main findings of the simulations of a prototypic/academic IVR cooling system. A parameter study showed that the modeling approach of the bubble diameter has little influence on integral parameters of the complete cooling system. Also the detail of simulation, in regards of including the ceramic pool, the metallic layer and the RPV wall in the simulation by coupling their energy boundary conditions, had little influence on the steady-state mass flow rate and the maximum local void fraction. The most important parameter according to this study is the subcooling of the cooling water. This parameter is hard to determine in a real world case, as it depends on the temperature of the structural material of the water pool. Subcoolings lower than 20 K showed a very unstable circulation rate which makes it impossible to determine if accurate cooling of the RPV wall can be ensured. Subcoolings bigger than 20 K resulted in very stable circulation mass flows. The maximum local void fraction was, in all simulations with stable conditions, below 0.65. For the recalculations of the IVR like experiments by Park et al. (2013) in chapter 5.2.2 the maximum void fraction was 0.81, if the heat flux in the metallic layer was equal to the critical heat flux.

Table 6.4: Parameter study of passive IVR system.

Variable	Values	Outcome
coupling time step	$[0.1, 0.05]$ s	$\Delta m = 1.0 \ \frac{kg}{s}; \ \Delta \alpha = 0$
bubble diameter	[IATE, const 7 mm]	$\Delta m = 6.0 \ \frac{kg}{s}; \ \Delta \alpha = 0$
systems in simulation	[multiregion, only cooling water]	$\Delta m = 0.5 \ \frac{kg}{s}; \ \Delta \alpha = 0.02$
subcooling	$[5, 10, 15, 20, 30, 40]$ K	stable for $T_{sub} > 20K$

6.2.7 Suggestions for Design Optimizations

To ensure a stable natural circulation flow, in the cooling path of an IVR system, subcoolings of less than 20 K for this specific system have to be avoided. Or more general, the part of the residual heat that is supplied to the cooling water has to be less than the heat needed to achieve saturated conditions, when leaving the heated section of the cooling path

$$Q_{toCoolingWater} < G * c_{p,l} * \Delta T_{sub}. \tag{6.11}$$

The subcooling of the water around the RPV wall will be determined by the temperature of the structural material in the containment. To keep these structures below a certain temperature, it would be necessary to cool the whole containment from the outside. In current designs, a containment cooling with an outside water storage tank is already foreseen, but if this is sufficient to keep the temperature below the required limit cannot be answered in this study.

7. Conclusion and Outlook

The focus of this study has been on the development of the simulation tools and models for two-phase flow wall heat transfer in large multiscale systems under subcooled conditions. This was accompanied with extensive verification and validation of the newly developed models and tools. Main contributions are the development of a robust wall heat transfer model for two-phase flows under subcooled nucleate flow boiling conditions in an Eulerian modeling framework and the coupling of a legacy STH code with a CFD library for two-phase flows.

This last chapter is intended to draw conclusions of the presented work and also give an outlook to propose future work in this field.

7.1 Conclusion

The following summarizes the main contributions by this study and conclusions are drawn from the findings:

- It has been shown that is possible to predict void fraction profiles and wall temperatures within an Eulerian modeling framework under subcooled nucleate boiling flow conditions. The accuracy of the prediction of void fraction profiles was not satisfactory under all conditions. Especially the recalculation of experiments in an annular geometry, showed deviations between simulation results and experimental data that were greater than the measurement error of the experiment. To obtain these void fraction profiles, a robust model for the wall heat transfer has been developed. Robust means that it is not subject to user input tuning parameters found in many industry standard models. It is build on top of the ideas by Chen (1966), who proposed a integral 1D correlation to predict the wall heat transfer under saturated flow boiling conditions and by Steiner et al. (2005), who extended this model to reduce its dependency on integral flow parameters. The contributions made in this study are the modeling of the convective part of the heat transfer just from local, near wall fluid parameters and to implement it in a two-fluid approach, where the evaporation rate is obtained from the model in addition to the wall temperature.

- Validation of the wall heat transfer model and its implementation has been carried out in three steps. The first step was the recalculation of isothermal experiments to study the influence of the modeling approaches to interfacial forces and interfacial

area concentration. This was done with isothermal experiments to isolate the in itself already complex phenomena of interfacial momentum transfer from phase change phenomena between the phases. The influence of interfacial area concentration on the liquid and gas velocities was found to be small in these isothermal experiments. Different models of the drag force showed to have a bigger influence while the simulations with the model by Ishii and Zuber (1979) had the best agreement with experimental data. The overall agreement with experimental data was excellent for the isothermal recalculations in case of liquid and gas velocities. The void fraction profiles showed larger differences with the experimental data. A reason for these differences could be found in the uncertainties associated with the inlet conditions of the gas bubbles.

- The second and most important step for the validation of the wall heat transfer model was the recalculation of experiments in the subcooled flow boiling regime. Three experimental series have been chosen for recalculation. The first experiments by Bibeau and Salcudean (1994) provided data for the comparison of wall temperatures for laminar flow in an annular geometry. The wall temperatures were slightly underpredicted in the simulations, but the trend was captured very well. The second experiment by Bartolomei et al. (1980) provided cross section averaged void fractions at different axial position in heated pipes. The important aspect of these experiments was that the heated section was followed by an adiabatic section. As the heated section is dominated by evaporation and the adiabatic section by condensation the recalculation of this experiment gives insightful information on the validity of these two separate effects. It was shown that both effects can be reproduced by the solver. The third experiments (Lee et al. (2002)) focused on the detailed void fraction profile in one axial position of an internally heated annular geometry. Three different runs of this experimental series were recalculated. The case with the smallest mass flow rate was in almost perfect agreement with the experimental data (void fraction, liquid and vapor velocity profiles have been compared), while the case with the highest mass flow rates showed the limitations of this modeling approach. Here it was only possible to qualitatively reproduce the void fraction profile, but the peak values were much lower than in the experiment.

- Recalculation of experiments with wall heat fluxes in the vicinity of the critical heat flux are the third step of the validation process for the wall heat flux model. The goal of these recalculations was the investigation of the influence of wall heat flux on the near-wall void fraction at high heat fluxes. A secondary goal was to test the numerical stability of the solver for the expected high local void fractions. Recalculation of one experiment in a pipe and one experiment with a hemispherical geometry has shown that a maximum near-wall void fraction of about 0.8 was found at heat fluxes that were reported in the experiment as critical heat fluxes. This is by no means a measure for critical heat flux, but rather an observation for these two distinct cases. Further studies on a wider range of parameters should be considered here.

- To obtain the wall heat flux distribution on the outer side of the RPV wall in case of a severe accident, it is necessary to simulate the natural convection in combination with solidification phenomena inside the RPV. According to Esmaili and Khatib (2004), the formation of an internally heated ceramic pool, with one metallic layer on top is the most likely core melt configuration in the late phase of a severe accident. Partial melting of the RPV wall also has an influence of the outside wall heat flux (Cao et al. (2015)). To simulate the combined convection and solidification/melting phenomena, one experiment by Gau and Viskanta (1986) has been recalculated to validate the already implemented model. Good agreement of experimental data and

simulation results have been found for this case.

- The coupling of CFD codes and STH codes brings great savings in computational time for the simulation of large multiscale systems. Areas which require high resolution simulations are resolved by the CFD code and parts of the system, where empirical correlation are valid or detailed information is not necessary, are simulated with a STH code. Such a coupled simulation tool has been realized in this study by combining the STH code ATHLET and the OpenFOAM CFD library in an efficient way. Efficient means that no write and read operations are involved in the coupling process and that the full parallel calculation capabilities of the CFD code are retained. The coupled code has been verified by comparing single and two-phase simulations of the coupled system against STH standalone simulation results.

- To demonstrate the capabilities of the developed simulation tool a prototypical/academic IVR cooling system has been modeled. In a first step, results of lumped parameter code simulation results by Esmaili and Khatib (2004) and Zhang et al. (2010) have been compared to present CFD results. The remaining RPV vessel wall thickness as well as the crust thickness in the ceramic pool were in good agreement. The absolute values for the wall heat flux were also similar, but the distribution was different between the two modeling approaches. In a next step, the simulation was extended with a natural circulation cooling path to simulate the cooling of the RPV wall under passive conditions. This cooling path was realized with the coupled CFD-STH approach. The region of the cooling path, which is in direct contact to the RPV wall, where the subcooled nucleate boiling heat transfer is occurring, is simulated with a CFD approach and the rest of the loop is simulated by the STH code. Main findings are that a minimum subcooling of 20 K of the cooling water is necessary to ensure a stable natural circulation flow for a given containment pressure of 2 bar. With higher subcoolings, a lower natural circulation mass flow rate is achieved. The maximum local void fraction for 20 K subcooling was 0.65.

7.2 Outlook

The modeling of two-phase flow wall heat transfer would benefit from a better understanding of the dynamics of bubble departure and liftoff, especially in the presence of many bubbles close to each other. The interactions between bubbles at departure are still not understood completely.

A next step for the integral simulation of the passive IVR system would be to replace the STH region with a CFD modeling approach. Especially the detailed simulation of the steam vent or the water storage tank would be beneficial to the further understanding of the subject. As the inlet subcooling was found to be the main influence on the flow stability, a better understanding of the thermal-hydraulic phenomena in the water storage pool are a necessity.

The relocation process of the core and the structural material supporting it is not taken into consideration in this study at all. Mass fractions of UO_2 or the mass of molten stainless steel introduce big uncertainties. A deeper understanding of the relocation process would be necessary to accurately predict the position and the thickness of the metallic layer. The thickness of the metallic layer determines the focusing effect, which remains the biggest threat to the integrity of the RPV wall.

The interaction of the cooling path with the containment is implemented very rudimentary in the current model by assuming a constant filling level of the water in the storage tank. Also the pressure in the containment is assumed to be constant. To resolve these issues, the further coupling with a containment code like COCOSYS can help.

Bibliography

S P Antal, R T Lahey, and J E Flaherty. Analysis of phase distribution in fully developed laminar bubbly two-phase flow. *International Journal of Multiphase Flow*, 17(5):635–652, 1991.

G Bandini, M Polidori, A Gerschenfeld, D Pialla, W Ma, Pavel Kudinov, M Jeltsov, K Kööp, K Huber, X Cheng, C Bruzzese, A Class, D Prill, A Papukchiev, C Geffray, R Macian-Juan, and L Maas. Assessment of systems codes and their coupling with CFD codes in thermal–hydraulic applications to innovative reactors. *Nuclear Engineering and Design*, 281:22–38, 2015.

G G Bartolomei, G N Batashova, and V G Brantov. *Teplomassoobmen-IV*, volume 5. ITMO AN BSSR Press, 1980.

A Behzadi, R Issa, and H Rusche. Modelling of dispersed bubble and droplet flow at high phase fractions. *Chemical Engineering Science*, 59:759–770, 2004.

I H Bell, J Wronski, S Quoilin, and V Lemort. Pure and Pseudo-pure Fluid Thermophysical Property Evaluation and the Open-Source Thermophysical Property Library CoolProp. *Industrial & Engineering Chemistry Research*, 53(6):2498–2508, 2014.

D Bestion. The difficult challenge of a two-phase CFD modelling for all flow regimes. *Nuclear Engineering and Design*, 279:116–125, 2014.

D Bestion, H Anglart, D Caraghiaur, P Péturaud, B Smith, M Andreani, B Niceno, E Krepper, D Lucas, F Moretti, M C Galassi, J Macek, L Vyskocil, B Koncar, and G Hazi. Review of Available Data for Validation of Nuresim Two-Phase CFD Software Applied to CHF Investigations. *Science and Technology of Nuclear Installations*, 2009, 2009.

E.L. Bibeau and M. Salcudean. Subcooled void growth mechanisms and prediction at low pressure and low velocity. *International Journal of Multiphase Flow*, 20(5):837 – 863, 1994. ISSN 0301-9322.

A Bui, N Dinh, and B Williams. Validation and Calibration of Nuclear Thermal Hydraulics Multiscale Multiphysics Models–Subcooled Flow Boiling Study. Technical report, Idaho National Laboratory (INL), 2013.

A D Burns, T Frank, I Hamill, and J M Shi. The Favre averaged drag model for turbulent dispersion in Eulerian multi-phase flows. *5th International Conference on Multiphase Flow*, 2004.

Z Cao, X Liu, and X Cheng. A two dimensional approach for temperature distribution in reactor lower head during severe accident. *Annals of Nuclear Energy*, 85:467–480, 2015.

J C Chen. Correlation for boiling heat transfer to saturated fluids in convective flow. *Industrial & engineering chemistry process design and development*, 5(3):322–329, 1966.

X Cheng. R&D on Nuclear Safety and Severe Accident Mitigation in China. *Asian Research Policy*, 4:30–43, 2013.

X Cheng and U Müller. Review on Critical Heat Flux in Water Cooled Reactors. Technical report, Forschungszentrum Karlsruhe, 2003.

J G Collier and J R Thome. *Convective boiling and condensation*. Clarendon Press, 1996.

E De Villiers. *The potential of large eddy simulation for the modelling of wall bounded flows*. PhD thesis, University of London, 2007.

V K Dhir. Nucleate and transition boiling heat transfer under pool and external flow conditions. *International journal of heat and fluid flow*, 12(4):290–314, 1991.

T N Dinh, J P Tu, T Salmassi, and T G Theofanous. Limits of coolability in the AP1000-related ULPU-2400 Configuration V facility. Technical report, Center for Risk Studies and Safety University of California, 2003.

H Esmaili and M Khatib. Analysis of in-vessel retention and ex-vessel fuel coolant interaction for AP1000. Technical report, U.S. Nuclear Regulatory Commission, 2004.

J H Ferziger and M Peric. *Computational methods for fluid dynamics*. Springer Science & Business Media, 2012.

H K Forster and N Zuber. Dynamics of vapor bubbles and boiling heat transfer. *AIChE Journal*, 1(4):531–535, 1955.

Message P Forum. MPI: A Message-Passing Interface Standard. Technical report, University of Tennessee Knoxville, 1994.

T Frank, P J Zwart, E Krepper, and H M Prasser. Validation of CFD models for mono-and polydisperse air–water two-phase flows in pipes. *Nuclear Engineering and Design*, 238: 647–659, 2008.

C Gau and R Viskanta. Melting and solidification of a pure metal on a vertical wall. *Journal of Heat Transfer*, 108(1):174–181, 1986.

D C Groeneveld, S C Cheng, and T Doan. 1986 AECL-UO critical heat flux lookup table. *Heat Transfer Engineering*, 7:46–62, 1986.

C Grossetete. Caracterisation experimentale et simulations de l evolution d un ecoulement diphasique a bulles ascendant dans une conduite verticale. Technical report, EDF, 1995.

A Gubaidullin. *Natural convection heat transfer in two-fluid stratified pools with internal heat sources*. PhD thesis, Royal Institute of Technology, 2001.

Z Guozhi, C Xinrong, and S Xingwei. A study using RELAP5 on capability and instability of two-phase natural circulation flow under passive external reactor vessel cooling. *Annals of Nuclear Energy*, 60:115–126, 2013.

M Ishii and T Hibiki. *Thermo-Fluid Dynamics of Two-Phase Flow*. Springer, 2011.

M Ishii and N Zuber. Drag coefficient and relative velocity in bubbly, droplet or particulate flows. *AIChE Journal*, 25(5):843–855, 1979.

M Jamet, J Lavieville, K Atkhen, and N Mechitoua. Validation of NEPTUNE CFD on ULPU-V experiments. *Nuclear Engineering and Design*, 293:468–475, 2015.

G Janssens-Maenhout. *Beiträge zur Modellierung und numerischen Simulation von Zweiphasenströmungen mit Wärmeübertragung.* PhD thesis, 1999.

M Jeltsov, K Kööp, P Kudinov, and W Villanueva. Development of a Domain Overlapping Coupling Methodology for STH/CFD Analysis of Heavy Liquid Metal Thermalhydraulics. In *NURETH-15*, 2013.

D Jin, L Fei, X Liu, and X Cheng. Thermal-hydraulic analysis of external reactor vessel cooling for an advanced large size PWR. In *ICAPP 2013*, 2013.

GKW Kenway. *A Scalable, Parallel Approach for Multi-Point, High-Fidelity Aerostructural Optimization of Aircraft Configurations.* PhD thesis, University of Toronto, 2013.

J F Klausner, R Mei, D M Bernhard, and L Z Zeng. Vapor bubble departure in forced convection boiling. *International Journal of Heat and Mass Transfer*, 36:651–662, 1993.

S Knight. Building Software with SCons. *Computing in Science and Engg.*, 7(1), January 2005.

N I Kolev. How accurately can we predict nucleate boiling? *Experimental Thermal and Fluid Science*, 10:370–378, 1995.

E Krepper and R Rzehak. CFD for subcooled flow boiling: Simulation of DEBORA experiments. *Nuclear Engineering and Design*, 241:3851–3866, 2011.

N Kurul and M Z Podowski. On the modeling of multidimensional effects in boiling channels. In *27th National Heat Transfer Conference, Minneapolis*, 1991.

R T Lahey. The simulation of multidimensional multiphase flows. *Nuclear Engineering and Design*, 235:1043–1060, 2005.

B E Launder and D B Spalding. The numerical computation of turbulent flows. *Computer Methods in applied Mechanics and Engineering*, 3:269–289, 1974.

S S Lee, S H Kim, and K Y Suh. The design features of the advanced power reactor 1400. *Nuclear Engineering and Technology*, 41(8):995–1004, 2009.

T H Lee, G C Park, and D J Lee. Local flow characteristics of subcooled boiling flow of water in a vertical concentric annulus. *International Journal of Multiphase Flow*, 28:1351–1368, 2002.

M Lemmert and J M Chawla. Influence of flow velocity on surface boiling heat transfer coefficient. *Heat Transfer and Boiling*, pages 237 –247, 1977.

G Lerchl. Kopplung von ATHLET mit dem CFD-Programm CFX. Technical report, Gesellschaft fuer Anlagen- und Reaktorsicherheit (GRS) gGmbH, 2007.

G Lerchl. *ATHLET Mod 3 Cycle A Models and Methods*, 2012.

C Lifante, T Frank, and A Burns. Wall boiling modeling extension towards critical heat flux. *The 15th International Topical Meeting in Nuclear Reactor Thermalhydraulics, NURETH-15*, 2013.

W Ma, E Bubelis, A Karbojian, and B R Sehgal. Transient experiments from the thermalhydraulic ADS lead bismuth loop (TALL) and comparative TRAC/AAA analysis. *Nuclear Engineering and Design*, 236:1422–1444, 2006.

J Macek and L Vyskocil. Simulation of critical heat flux experiments in NEPTUNE CFD code. In *Experiments and CFD Code Application to Nuclear Reactor Safety (XCFD4NRS)*, 2008.

J Mahaffy, B Chung, C Song, F Dubois, and E Graffard. Best practice guidelines for the use of CFD in nuclear reactor safety applications. Technical report, NEA, CSNI, 2007.

M R Malin. On the calculation of heat transfer rates in fully turbulent wall flows. *Applied mathematical modelling*, 11:281–284, 1987.

R C Martinelli and D B Nelson. Prediction of Pressure Drop During Forced Circulation Boiling of Water. *Trans. ASME*, 70:695, 1948.

W H McAdams, W E Kennel, and C S Minden. Heat transfer at high rates to water with surface boiling. *Industrial & Engineering Chemistry*, 41(9):1945–1953, 1949.

F R Menter, M Kuntz, and R Langtry. Ten years of industrial experience with the SST turbulence model. *Turbulence, Heat and Mass Transfer*, 4(1):625–632, 2003.

B Niceno, M T Dhotre, and N G Deen. One-equation sub-grid scale (SGS) modelling for Euler–Euler large eddy simulation (EELES) of dispersed bubbly flow. *Chemical Engineering Science*, 63:3923–3931, 2008.

H Oertel Jr, M Böhle, and T Reviol. *Stroemungsmechanik*. Vieweg+Teubner Verlag, 2011.

H M Park, Y H Jeong, and S Heo. The effect of the geometric scale on the critical heat flux for the top of the reactor vessel lower head. *Nuclear Engineering and Design*, 258: 176–183, 2013.

R J Park, K S Ha, and H Y Kim. Detailed evaluation of natural circulation mass flow rate in the annular gap between the outer reactor vessel wall and insulation under IVR-ERVC. *Annals of Nuclear Energy*, 89:50–55, 2016.

J L Rempe, D L Knudson, M Cebull, C L Atwood, and C M Allison. Potential for AP600 InVessel Retention through Ex-Vessel Flooding. Technical report, INEEL, EXT, 1997.

F Rösler and D Brüggemann. Shell-and-tube type latent heat thermal energy storage: numerical analysis and comparison with experiments. *Heat and Mass Transfer*, 47(8): 1027–1033, 2011.

S Rouge. SULTAN test facility for large-scale vessel coolability in natural convection at low pressure. *Nuclear Engineering and Design*, 169:185–195, 1997.

H Rusche. *Computational fluid dynamics of dispersed two-phase flows at high phase fractions*. PhD thesis, University of London, 2003.

R Rzehak and E Krepper. Bubbly flows with fixed polydispersity: validation of a baseline closure model. *Nuclear Engineering and Design*, 287:108–118, 2015.

P Sadasivan, C Unal, and R Nelson. Perspective: issues in CHF modeling—the need for new experiments. *Journal of Heat Transfer*, 117(3):558–567, 1995.

L Schiller and A Naumann. Fundamental calculations in gravitational processing. *Zeitschrift Des Vereines Deutscher Ingenieure*, 77:318–320, 1933.

W Schroeder, K W Martin, and B Lorensen. *The Visualization Toolkit: An Object-oriented Approach to 3D Graphics*. Prentice Hall PTR, 1996.

R Situ, T Hibiki, M Ishii, and M Mori. Bubble lift-off size in forced convective subcooled boiling flow. *International Journal of Heat and Mass Transfer*, 48:5536–5548, 2005.

M Sonntag and X Cheng. CFD model for simulation of subcooled nucleate flow boiling - implementation and validation. In *Proc. CFD4NRS-6, Boston, Massachusetts, USA, 13 Sep 2016 - 15 Sep 2016*, 2016.

H Steiner. *Modeling and Numerical Simulation of complex technical flows*. Graz University of Technology, 2006.

H Steiner, A Kobor, and L Gebhard. A wall heat transfer model for subcooled boiling flow. *International Journal of Heat and Mass Transfer*, 48:4161–4173, 2005.

C R Swaminathan and V R Voller. A general enthalpy method for modeling solidification processes. *Metallurgical Transactions B*, 23(5):651–664, 1992.

D Tenchine, D Pialla, T H Fanning, and J W Thomas. International benchmark on the natural convection test in Phenix reactor. *Nuclear Engineering and Design*, 258:189–198, 2013.

T G Theofanous, S Syri, and T Salmassi. Critical heat flux through curved, downward facing, thick walls. *Nuclear Engineering and Design*, 151:247–258, 1994.

T G Theofanous, C Liu, S Additon, and S Angelini. In-vessel coolability and retention of a core melt. *Nuclear Engineering and Design*, 169:1–48, 1997.

V Ustinenko, M Samigulin, A Ioilev, and S Lo. Validation of CFD-BWR, a new two-phase computational fluid dynamics model for boiling water reactor analysis. *Nuclear Engineering and Design*, 238:660–670, 2008.

V R Voller and C Prakash. A fixed grid numerical modelling methodology for convection-diffusion mushy region phase-change problems. *International Journal of Heat and Mass Transfer*, 30(8):1709–1719, 1987.

L Vyskocil and J Macek. Cfd simulation of critical heat flux in a tube. *Computational Fluid Dynamics (CFD) for Nuclear Reactor Safety Applications - Workshop Proceedings, CFD4NRS-3 - Experimental Validation and Application of CFD and CMFD Codes to Nuclear Reactor Safety Issues*, page 1231, 2012.

X Wang and X Cheng. Analysis of Focusing Effect of Light Metallic Layer in Stratified Molten Pool Under IVR-ERVC Condition. *Journal of Nuclear Engineering and Radiation Science*, 1(2), 2015.

J Weisman and B S Pei. Prediction of critical heat flux in flow boiling at low qualities. *International Journal of Heat and Mass Transfer*, 26(0):1463–1477, 1983.

Westinghouse. AP1000 Design Control Document Rev. 19, Tier 2, Chapter 5. Reactor Coolant System and Connected Systems. Section 5.3, Reactor Vessel. Technical report, Westinghouse, 2011.

D C Wilcox. Reassessment of the scale-determining equation for advanced turbulence models. *AIAA Journal*, 26(11):1299–1310, 1988.

Q Wu, S Kim, M Ishii, and S G Beus. One-group interfacial area transport in vertical air-water bubbly flow. Technical report, U.S. Department of Energy, 1997.

S Yamoah and R Martínez. Numerical investigation of models for drag, lift, wall lubrication and turbulent dispersion forces for the simulation of gas–liquid two-phase flow. *Chemical Engineering Research and Design*, 98:17–35, 2015.

W Yao and C Morel. Volumetric interfacial area prediction in upward bubbly two-phase flow. *International Journal of Heat and Mass Transfer*, 47:307–328, 2004.

GH Yeoh and JY Tu. Two-fluid and population balance models for subcooled boiling flow. *Applied mathematical modelling*, 30(11):1370–1391, 2006.

J Yue, W Xu, X Liu, and X Cheng. In- and ex-vessel coupled analysis of ivr-ervc phenomenon for large scale pwr. *Annals of Nuclear Energy*, 80:322 – 337, 2015.

L Z Zeng, J F Klausner, and R Mei. A unified model for the prediction of bubble detachment diameters in boiling systems—I. Pool boiling. *International Journal of Heat and Mass Transfer*, 36(9):2261–2270, 1993.

Y P Zhang, S Z Qiu, G H Su, and W X Tian. Analysis of safety margin of in-vessel retention for AP1000. *Nuclear Engineering and Design*, 240:2023–2033, 2010.

M Zheng, J Yan, S Jun, L Tian, X Wang, and Z Qiu. The General Design and Technology Innovations of CAP1400. *Engineering*, 2:97–102, 2016.

N Zuber. The dynamics of vapor bubbles in nonuniform temperature fields. *International Journal of Heat and Mass Transfer*, 2:83–98, 1961.